

國 立 交 通 大 學

電控工程研究所

碩士論文

利用垂直梳狀致動器驅動之抬起式微掃描鏡之設計、
製作及組裝

**Design, Fabrication and Assembly of a Flip-Up Micro
Scanning Mirror with Vertical Comb Drive**

研究生：陳政安

指導教授：邱一 博士

中華民國九十九年十月

利用垂直梳狀致動器驅動之抬起式微掃描鏡之設計、
製作及組裝

**Design, Fabrication and Assembly of a Flip-Up Micro
Scanning Mirror with Vertical Comb Drive**

研 究 生:陳政安

Student: Cheng-An Chen

指 導 教 授:邱一

Advisor : Yi Chiu

國立交通大學 電機學院

電控工程研究所

碩士論文

A Thesis

Submitted to Institute of Electrical Control Engineering

College of Electrical Engineering

National Chiao Tung University

In Partial Fulfillment of the Requirement

For the Degree of

Master

In

Electrical Control Engineering

October 2010

Hsinchu, Taiwan, R.O. C

中華民國九十九年十月

中文摘要

近年來隨著半導體產業的發展，微機電製程技術有許多重大的發展。微光機電技術(Micro-Opto-Electro-Mechanical System)提供了一個實現微型光學系統的好方法。在自由空間的光學平台應用上，三維抬起式微結構的角色也更加重要。

我們的最終目標為設計一微光學資訊儲存平台，採用 SOI (Silicon on Insulator)基板上的單晶矽作為鏡面結構，因為它的低應力可以避免其他材料製作時可能發生的翹曲現象。SU-8 光阻可用簡單微影製程製作高深寬比結構，所以使用它來製作結構層。

本實驗室之前已提出利用簡單下壓動作進行任意角度斜面鏡的組裝，成功驗證了不同角度的組裝，並將 135°斜面鏡應用在微光學讀取頭的架構。本論文提出一構想，在以下壓方法的組裝基礎上，在斜面鏡上製作垂直梳狀致動的微掃描鏡，並將之應用在微光學讀取頭的架構當中實現循軌伺服的功能。

本論文已成功量測到組裝前靜態與動態掃描特性。具有直線形扭力彈簧的微掃描鏡在 110V 的直流電壓驅動下有 0.57°的機械掃描角。具有彎曲式彈簧的微掃描鏡在 5V 直流電壓±5V 交流電壓的驅動下，在共振頻率下具有 0.8°的光學掃描角。由於梳指間隙受限於曝光機的誤差約±2μm，所以限制了微掃描鏡的效能，本論文也提出了一新式的製程，可將梳指間隙縮小至 3μm，提升效能。

Abstract

Recently, Micro Electro Mechanical System (MEMS) technology has many important developments with the rapid progress in the semiconductor industry. Micro-Opto-Electro-Mechanical System (MOEMS) technology provides a method to realize miniaturized optical systems. Three-dimensional (3-D) flip-up MEMS structures are important components in applications such as free-space optical bench.

In this thesis, low-stress silicon on insulator (SOI) wafers are used to avoid stress-induced curvature for optical applications. SU-8 can be processed by simple lithography with high aspect ratio, making it suitable for another structural layer.

In our previous study, flip-up structures with arbitrary angles were assembled using a simple push operation. The design and assembly of 135° mirrors were verified and used in the proposed optical pickup head. A flip-up micro scanning mirrors assembled by the simple push operation were proposed in this thesis. It can be integrated on the proposed optical pickup head as the tracking servo actuator. The characteristics of the micro scanning mirror before assembly were measured. The maximum static scanning angle of the beam type mirror was 0.57° with 110 V applied voltage. The maximum dynamic scanning angle of the meander type mirror was 0.80° with ± 5 V sinusoidal and 5 V DC applied voltage at 413.6 Hz. The performance was strongly related to the finger gaps. The large finger gaps were limited by the accuracy of the aligner. The vertical comb fingers fabricated by the new fabrication process are proposed to improve the performance.

致謝

歷經了無數個充滿淚水與歡笑的日子後，兩年多的碩班生涯集結踏上句點，遙想當年懵懂的加入實驗室依舊像是昨天一樣。最欣慰的是這段時間以來能有所成長，讓自己更加茁壯。

在交大求學的日子裡，最感謝的是我的指導老師邱一老師，不論是大學時期修電磁學或是研究所的指導，都讓我學到了寶貴的知識與實驗上的經驗，最重要的是老師不斷灌輸追求學問所需的嚴謹態度，更讓我獲益良多。而在撰寫論文時老師也不厭其煩的修改，讓這本論文更加完美，謝謝！

感謝我的口試委員方維倫老師以及洪國永老師，在忙碌之餘還能給予我研究上的建議。方老師點出的問題讓我找出量測數據盲點所在，而洪老師也提供了許多我製程上所不能解決的寶貴意見，非常的感謝！

感謝 PSOC 實驗室的夥伴，健安學長以及經富學長，尤其是健安學長在製程上的經驗傳承使我在做實驗碰到問題也能迎刃而解。同時也感謝鴻智、姿穎、哲明、俊宏，在心情煩悶時可以互相打氣。感謝學弟彥霆以及彥杰，總是叫你們幫忙許多雜事，祝你們研究順利。

感謝奈米中心的技術員們，幫助我實驗所遇到的問題。邱俊誠老師實驗室詠鋒、宗穎及彥期，還有一同接 PSOC 計畫的岳正以及冠州學長，在製程上能互相幫忙。感謝方老師實驗室的信瑀學長，在最後的量測上幫助我許多技巧以及研究的心態。還有許許多多幫助過我的人，我會銘記在心，謝謝！

還有交大棒球隊的黃教練還有各位隊友，六年來帶給我太多美好的回憶，謝謝！

最後要感謝的是家人的支持，能讓我在異鄉能毫無牽掛的求學，不用擔心經濟上的問題，養育之恩無從報答！謝謝大家，謝謝培育我的交通大學。珍重再見！

Table of Content

中文摘要.....	i
Abstract.....	ii
致謝.....	iii
Table of Content.....	iv
List of Figures.....	vi
List of Table.....	xii
Chapter 1 Introduction.....	1
1-1 Motivation.....	1
1-2 Literature survey.....	5
1-2-1 Micro scanning mirrors.....	5
1-2-1-1 Electrostatic actuation.....	5
1-2-1-2 Thermal actuation.....	7
1-2-1-3 Magnetic actuation.....	9
1-2-1-4 Summary.....	13
1-2-2 Micro scanning mirror with vertical comb actuator.....	14
1-2-2-1 Wafer bonding.....	14
1-2-2-2 Multi-mask etching.....	20
1-2-2-3 Offset by self assembly.....	23
1-2-2-4 Multiple structure layers.....	25
1-2-2-5 Summary.....	29
1-2-3 Micro assembly.....	30
1-3 Objective and organization of the thesis.....	33
Chapter 2 Principle and Design.....	34
2-1 Introduction.....	34
2-2 Push assembly process.....	37

2-3	Static analysis.....	40
2-4	Dynamic analysis.....	43
2-5	Torsional spring analysis.....	49
2-5-1	Lateral spring constant k	50
2-5-2	Torsional spring constant k_s	51
2-6	Summary.....	54
Chapter 3	Fabrication Process.....	55
3-1	Introduction.....	55
3-2	Fabrication flow.....	55
3-3	Fabrication issues.....	66
3-3-1	SU-8 patterning.....	66
3-3-2	RIE lag phenomenon.....	69
3-3-3	Thermal release tape problem.....	70
3-3-4	Release problem.....	71
3-4	Summary.....	74
Chapter 4	Measurement and Results.....	76
4-1	Surface profile measurement.....	76
4-2	Static scanning measurement.....	85
4-3	Dynamic scanning measurement.....	89
4-3-1	Optical scanning measurement.....	94
4-4	Gold deposition measurement.....	96
4-5	Summary.....	100
Chapter 5	Conclusions and Future Work.....	101
5-1	Future work.....	101
Reference	107

List of Figures

Figure 1-1. Schematic of an optical switch [1].....	2
Figure 1-2. Schematic of a barcode reader [2].....	2
Figure 1-3. Schematic of the digital light processor (DLP) by Texas Instruments [3]...3	
Figure 1-4. Pickup head system on a 3-D optical bench [4].....	3
Figure 1-5. Schematic of the optical pickup with incorporated flip-up micro scanning mirror for tracking.....	4
Figure 1-6. Schematic of micro mirror actuated by parallel plate electrostatic force [6].....	6
Figure 1-7. SEM micrographs of the mirror array actuated by parallel plate electrostatic force [6].....	6
Figure 1-8. SEM micrographs of vertical and horizontal micro scanning mirrors [2]...7	
Figure 1-9. Schematic of the thermal actuator, (a) device top view, (b) cross-section of the device before release, (c) cross-section of the device after releasing the long beam, (c') cross-section of the device after releasing the short beam [7].....	8
Figure 1-10. SEM micrographs of thermally actuated micro scanning mirror [7].....	8
Figure 1-11. SEM micrographs of the thermally actuated micro scanning mirror [8]...9	
Figure 1-12. Schematic and side views of two types of magnetic scanning mirrors: (a) mirror with permalloy only and (b) mirror with permalloy and copper coils [9].....	10
Figure 1-13. Micrographs of two types of magnetic scanning mirrors: (a) mirror with permalloy and (b) mirror with permalloy and copper coils [9].....	10
Figure 1-14. SEM micrographs of the fabricated mirror, (a) overall view, (b) enlarged view of the mirror plate, (c) electrical connection between two points and (d) torsion bar [10].....	11

Figure 1-15. Operation principle of the magnetic scanning micro scanning mirror: (a) y-axis rotational actuation, (b) x-axis rotational actuation and (c) z-axis linear actuation [10].	12
Figure 1-16. Actuation concepts of the magnetostatic mirror, (a) schematic and (b) cross-section view [11].	13
Figure 1-17. SEM micrographs of the magnetostatic mirror: (a) front side and (b) back side [11].	13
Figure 1-18. SEM micrograph of the STEC micro scanning mirror [12].	15
Figure 1-19. Fabrication flow of the STEC micro scanning mirror [12].	15
Figure 1-20. Fabrication flow of the self-aligned micro scanning mirror [13].	16
Figure 1-21. SEM micrographs of the dual-mode and double-stacked device: (a) self-aligned combteeth and (b) top view of the mirror [13].	17
Figure 1-22. Schematic and SEM of the two dimensional self-aligned scanning mirror, (a) cross-section schematic and (b) SEM micrograph [14].	17
Figure 1-23. Basic structure of the two-structure bonded scanning mirror [15].	18
Figure 1-24. Assemble processes of the two-structure scanning mirror: (a) alignment and (b) eutectic bonding [15].	19
Figure 1-25. SEM micrograph of the upper structure with a bonded glass plate[15].	19
Figure 1-26. SEM micrographs of the eye-type micro scanning mirror, (a) upper view and (b) enlarged view of the combteeth [16].	20
Figure 1-27. Concept of the delay-mask process [17].	21
Figure 1-28. SEM micrographs of a micro scanning mirror fabricated by DMP	21
Figure 1-29. Schematic view of the micro scanning mirror with high fill-factor.	22
Figure 1-30. SEM micrographs of the scanning mirror with high fill-factor, (a) mirror array, (b) vertical comb actuator [18].	22
Figure 1-31. Fabrication processes of the self assembly vertical comb actuator [19].	23
Figure 1-32. SEM micrograph of a scanning mirror with self assembly vertical comb	

drive [19].....	24
Figure 1-33. SEM micrograph and schematic of the vertical comb actuator achieved by the bimorph cantilever [20].....	25
Figure 1-34. Schematic view of two types of mirrors, (a) type I device has one level of comb-drives and (b) type II device has two levels [21].....	26
Figure 1.35. SEM micrographs of the mirror, (a) type I device has one level of comb-drives (b) type II device has two levels [21].....	27
Figure 1-36. Schematic diagram of the dual mode micro scanning mirror [22].....	28
Figure 1-37. Principle of the vertical combdrive actuator, (a) upward actuation and (b) downward actuation [22].....	28
Figure 1-38. SEM micrograph of the dual mode micro scanning mirror [22].....	29
Figure 1-39. Schematic of the simple push assembly flow [5].....	31
Figure 1-40. An assembled 45° device, (a) top view, (b) side view, (c) interlock, (d) torsional beam of the mirror plate with mechanical stop.....	31
Figure 2-1 (a) 3D model of the proposed scanning mirror, (b) vertical comb fingers.....	35
Figure 2-2. Illustrations of electrical isolation and mechanical connection, (a) front side view, (b) back side view and (c) cross-section view along A-B.....	36
Figure 2-3. Assembly processes of the flip-up micro scanning mirror.....	38
Figure 2-4. Dimensions of the torsional beam.....	39
Figure 2-5. Cross section profile of the finger.....	40
Figure 2-6. Simulated rotation angle versus applied voltage.....	41
Figure 2-7. Illustration of the mirror dimensions.....	43
Figure 2-8. Model for modal analysis.....	44
Figure 2-9. Mode 1 of the beam type mirror: rotation around the spring.....	45
Figure 2-10. Mode 2 of the beam type mirror: piston motion along z-axis.....	45
Figure 2-11. Mode 3 of the beam type mirror: rotation around x-axis.....	45

Figure 2-12. Mode 4 of the beam type mirror: rotation around y-axis.....	46
Figure 2-13. Mode 1 of the meander type mirror: rotation around the spring.....	47
Figure 2-14. Mode 2 of the meander type mirror: piston motion along z-axis.....	47
Figure 2-15. Mode 3 of the meander type mirror: rotation around x-axis.....	47
Figure 2-16. Mode 4 of the meander type mirror: rotation around x-axis.....	48
Figure 2-17. Three types of the springs, (a) beam type, (b) meander type and (c) box type.....	49
Figure 2-18. Dimensions of the springs.....	50
Figure 2-19. Displacement versus applied pressure of three types of springs.....	50
Figure 2-20. Rotation angle versus applied pressure of three types of springs.....	52
Figure 2-21. Layout of the flip-up micro scanning mirror.....	54
Figure 3-1. Fabrication flow.....	56
Figure 3-2. Schematic of the HF vapor release setup [39].....	65
Figure 3-3. Schematic of the gold deposition.....	66
Figure 3-4. Optical micrograph of SU-8 patterned on the silicon substrate.....	67
Figure 3-5. Optical micrographs of SU-8 patterns on nitride, (a) without HMDS and (b) with HMDS.....	67
Figure 3-6. SU-8 patterns with different exposure dose, (a) 1 X, (b) 1.25 X, (c) 1.5 X, (d) 1.75 X and (e) 2 X.....	68
Figure 3-7. Back side patterns, (a) pattern without RIE lag prevention, (b) pattern with constant feature width.....	69
Figure 3-8. Optical micrographs of the device, (a) with RIE lag phenomenon, (b) without RIE lag phenomenon.....	70
Figure 3-9. Optical micrographs of the devices, (a) with good thermal conductivity and (b) with poor thermal conductivity.....	70
Figure 3-10. Devices stuck on the thermal release tape.....	71

Figure 3-11. Optical micrograph of the peeled-off SU-8.....	72
Figure 3-12. Optical micrographs of the mirror plate, (a) unreleased, (b) released for 2 hours, (c) gold coating on the 2 hours released mirror and (d) released for 6 hours.....	73
Figure 3-13. SEM micrograph of the devices, (a) top view of the mirror before back side ICP, (b) fabricated mirror and frame with broken torsional beam, (c) vertical comb actuator and (d) electrical isolation.....	74
Figure 3-14. SEM micrographs of the assembled mirror, (a) mirror with peeled-off SU-8, (b) side view of the mirror, (c) mislocked interlock and (d) torsional beam of the flip-up frame.....	75
Figure 4-1. Surface profile of the mirror plate of sample A, (a) 3-D profile, (b) cross section schematic of the mirror plate, (c) 2-D profile, (d) 2D profile of the flat area along A-B and (e) 2D profile of the flat area along C-D.....	77
Figure 4-2. Roughness measurement of sample A.....	79
Figure 4-3. Surface profile of the torsional spring of sample A.....	79
Figure 4-4. Optical micrograph of the micro scanning mirror after 2 hour releasing..	80
Figure 4-5. Surface profile of the mirror plate of sample B, (a) 3-D profile and (b) 2-D analysis.....	80
Figure 4-6. Surface profile of the torsional spring of sample B.....	81
Figure 4-7. Optical micrograph of the micro scanning mirror with gold coating.....	82
Figure 4-8. Surface profile of the mirror plate of sample C, (a) 3-D profile, (b) 2-D profile.....	82
Figure 4-9. Surface profile of the torsional spring of sample C.....	83
Figure 4-10. Setup of the static scanning measurement.....	86
Figure 4-11. Static scanning measurements by WYKO optical profiler, (a) unactuated, (b) 110V actuation and (c) difference between unactuated and 110V	

actuation profiles.....	86
Figure 4-12. Measured and simulated static scanning angle versus applied voltage...	87
Figure 4-13. Surface profile of the spring.....	88
Figure 4-14. Static scanning angle of the beam type and the meander type scanning mirror.....	88
Figure 4-15. Setup of the dynamic scanning measurement.....	90
Figure 4-16. Frequency response of a meander type scanning mirror.....	90
Figure 4-17. Illustration of the resonant modes, (a) schematic of four modes ,(b) mode 1, (c) mode 2, (d) mode 3 and (e) mode 4.....	91
Figure 4-18. Setup of the optical measurement.....	94
Figure 4-19. Images of the reflected laser on the screen: (a) without actuating and (b) with actuating.....	95
Figure 4-20. Measurement of sidewall of SU-8, (a) SEM micrograph and (b) EDS result.....	97
Figure 4-21. Measurement of the joint between SU-8 and the substrate, (a) SEM micrograph and (b) EDS result.....	98
Figure 4-22. Gold connection of the electrical isolation, (a) SEM micrograph and (b) EDS result.....	99
Figure 5-1. New fabrication flow.....	103

List of Tables

Table 2-1. Dimensions of the micro scanning mirror.....	42
Table 2-2. Result of the modal analysis.....	44
Table 2-3. Result of the modal analysis of the meander type micromirror.....	46
Table 2-4. Summary of spring simulation.....	53
Table 3-1. Roughness comparison.....	73
Table 4-1. Comparison of three samples.....	84
Table 4-2. Comparison between the simulation and measurement results of a meander type scanning mirror.....	90
Table 4-3. Optical scanning measurement.....	95



Chapter 1

Introduction

1-1 Motivation

Micro-electro-mechanical systems, also written as MEMS, are very small electro-mechanical systems fabricated by semiconductor fabrication technologies. It integrates many microcomponent into a microsystem. MEMS devices generally range in size from ten micrometers to millimeters. At these size scales, the behaviors may not be the same as macro devices, because of the large surface area to volume ratio of MEMS. Surface effects such as electrostatics and wetting dominate volume effect such as inertia. By decreasing area, MEMS can lower power consumption, save materials, improve performance, and lower cost. Due to these advantages, MEMS have been widely studied and become one of the most potential industries.

MEMS devices can be classified as microstructures, microsensors and microactuators according to the fields of application. Microstructures include microlens, microgear, inkjet printer head, etc.. Microsensors measure physical and chemical quantities such as pressure and acceleration. Many microsensors have been commercialized. Microactuators have various driving mechanisms, such as electrostatic, electromagnetic, and electrothermal actuators. These forms of energy can be changed to movement by the actuators. We can integrate numerous MEMS devices together with circuits to realize a micro system.

Microactuators fabricated by MEMS technologies have been widely used for optical applications and telecommunications networks such as optical switches (Figure 1-1) [1], variable optical attenuators, tunable filters and micro scanning

mirrors. Micro scanning mirrors are particularly used in barcode readers (Figure1-2) [2], micro displays (Figure 1-3) [3], and so on. Recently, much research has been carried out to make micro scanning mirrors using MEMS technology for a compact size, low cost, low power consumption, and light weight.

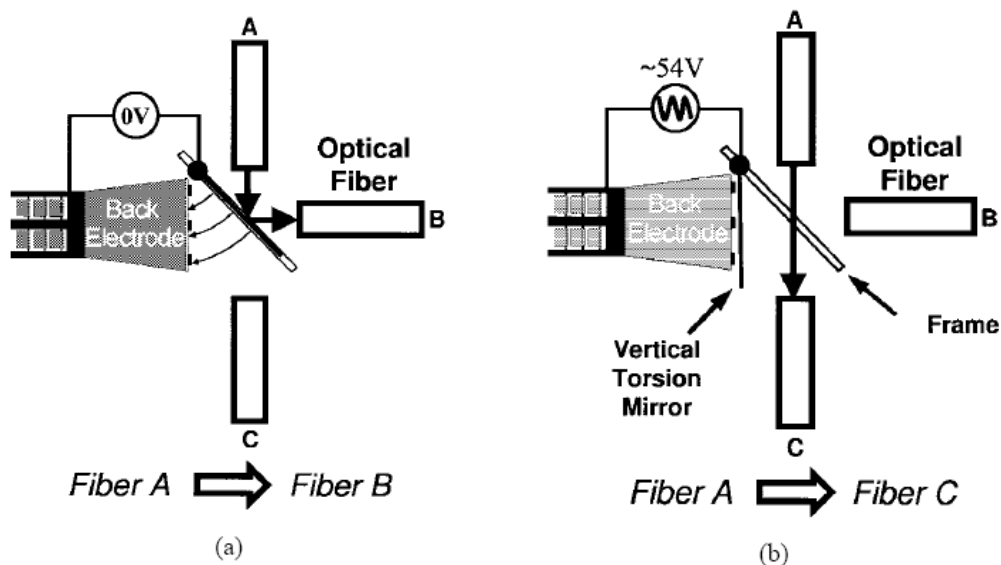


Figure 1-1. Schematic of an optical switch [1].

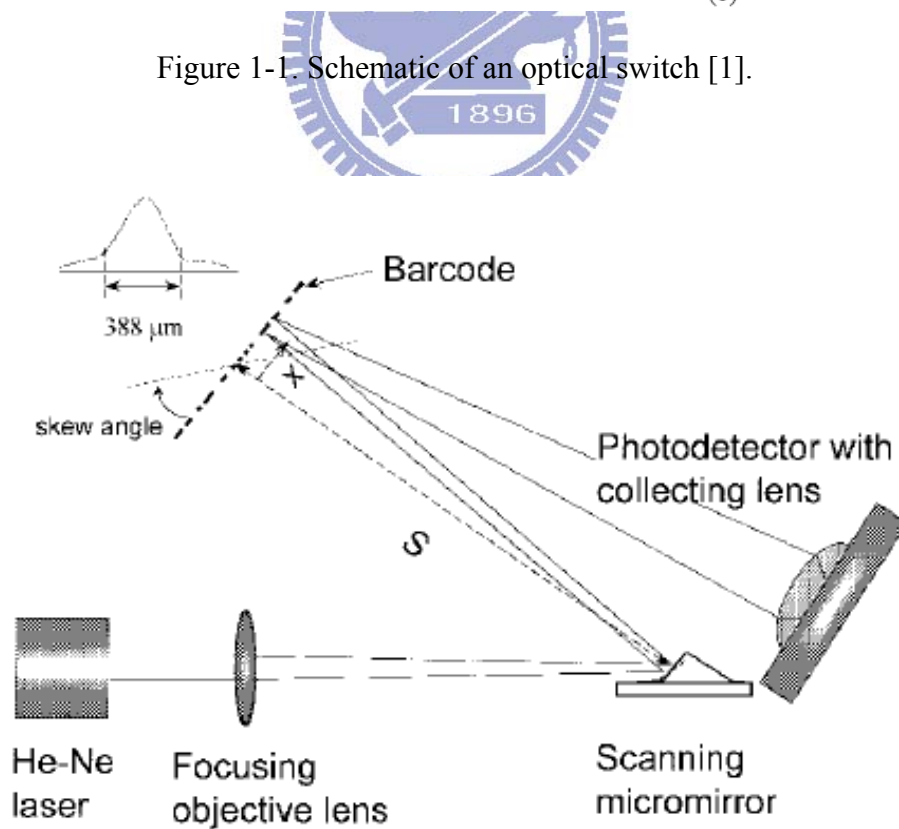


Figure 1-2. Schematic of a barcode reader [2].

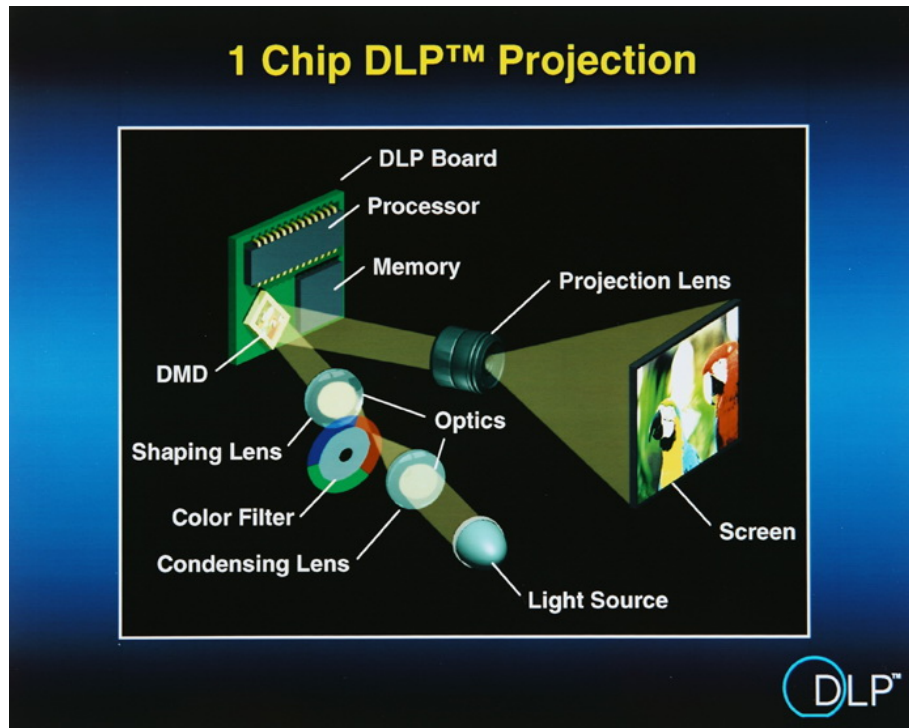


Figure 1-3. Schematic of the digital light processor (DLP) by Texas Instruments [3].

Three-dimensional (3-D) flip-up MEMS structures are important components in applications such as free-space optical benches (Figure 1-4) [4]. MEMS-based optical bench can be batch fabrication. Furthermore, flip-up microstructures assembled by simple operation can reduce production time and cost.

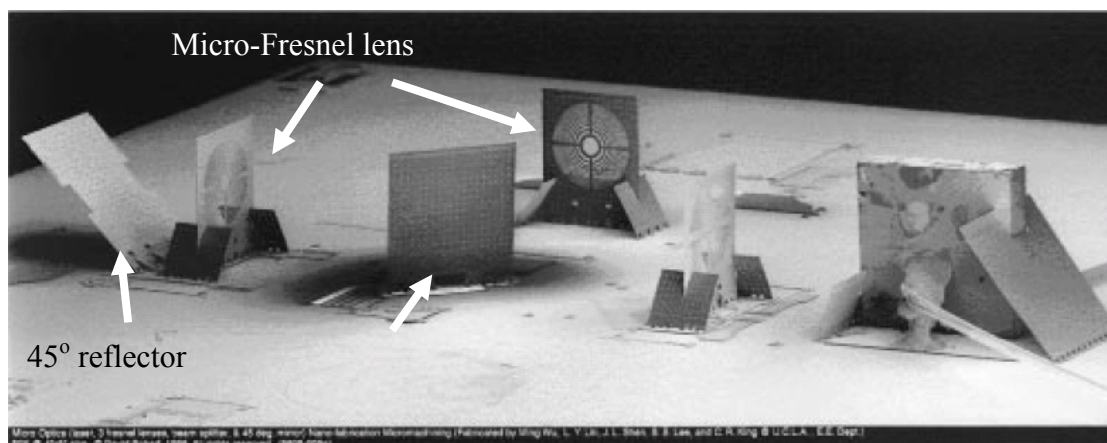


Figure 1-4. Pickup head system on a 3-D optical bench [4].

In our previous research [5], a MEMS-based optical pickup unit (OPU) assembled by simple push operation on SOI wafers was proposed. The optical pickup is composed of two 135° MEMS mirrors. In this optical pickup unit, a micro scanner can be integrated on the mirrors for tracking as Figure1-5 shows. In order to realize the tracking function, a micro scanning mirror actuated by a vertical comb actuator is proposed based on the flip-up plate of our previous research. Therefore, the main objective of this thesis is to fabricate flip-up micro scanning mirrors assembled by the novel simple push method. The DC optical scan angle must be larger than 0.03° and the torsional resonant frequency must be much higher than the disc rotation frequency 150 Hz.

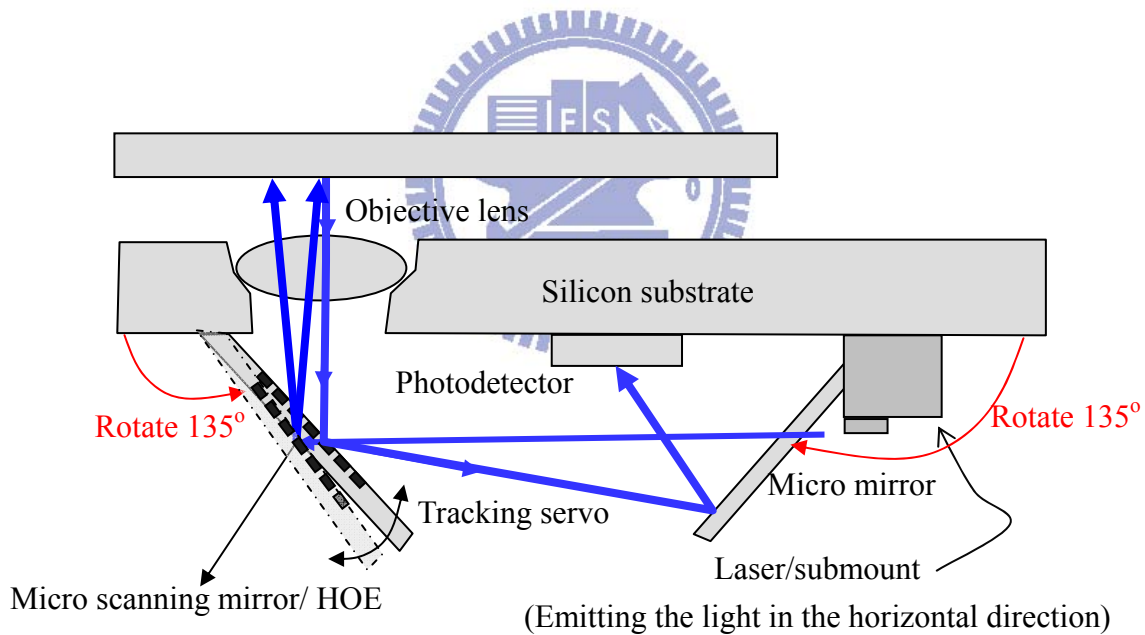


Figure 1-5. Schematic of the optical pickup with incorporated flip-up micro scanning mirror for tracking.

1-2 Literature survey

Micro scanning mirrors based on various actuation principles had been demonstrated in the literature. In the past years, many assembly methods for 3-D structures were demonstrated. In this section, micro scanning mirrors with different actuation methods are reviewed first. Then different kinds of assembly methods are reviewed .

1-2-1 Micro scanning mirrors

Various actuation methods had been applied to actuate micro scanning mirrors. In this section, micro scanning mirrors actuated by electrostatic actuators, thermal actuators and magnetic actuators are reviewed.

1-2-1-1 Electrostatic actuation

Electrostatic force can be used to actuate micro scanning mirrors by applying a voltage difference between fixed and movable electrodes. Many micro scanning mirrors reported to date employ electrostatic actuators. It offers fast speed with low power consumption and is relatively simple to design and fabricate. However, this method may suffer from the pull-in phenomenon, which limits its useful scan range. The digital light processing (DLP) technology (Figure 1-3) developed by Texas Instruments (TI) is an example that employs this actuation method [3].

Ford et al. presented a micro scanning mirror actuated by electrostatic force generated by a parallel plate actuator [6]. The operation principle is shown in Figure 1-6. When the voltage is applied to the bottom electrode, the electrostatic attraction force between the electrode and grounded mirror plate actuates the mirror. Figure 1-7 shows the SEM micrograph of the mirror array actuated by the parallel plate electrostatic force. The mirrors use an 80 V peak-to-peak 300 KHz sinusoidal signal

to switch between $\pm 10^\circ$ with a $20 \mu\text{s}$ response.

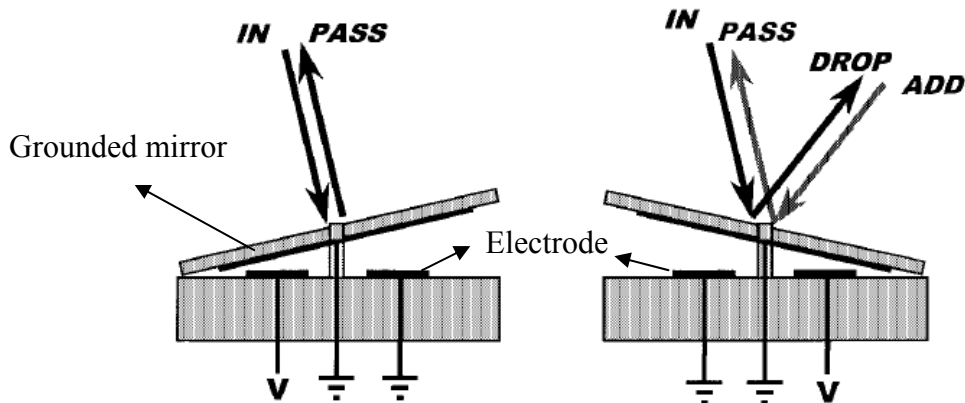


Figure 1-6. Schematic of micro mirror actuated by parallel plate electrostatic force [6].

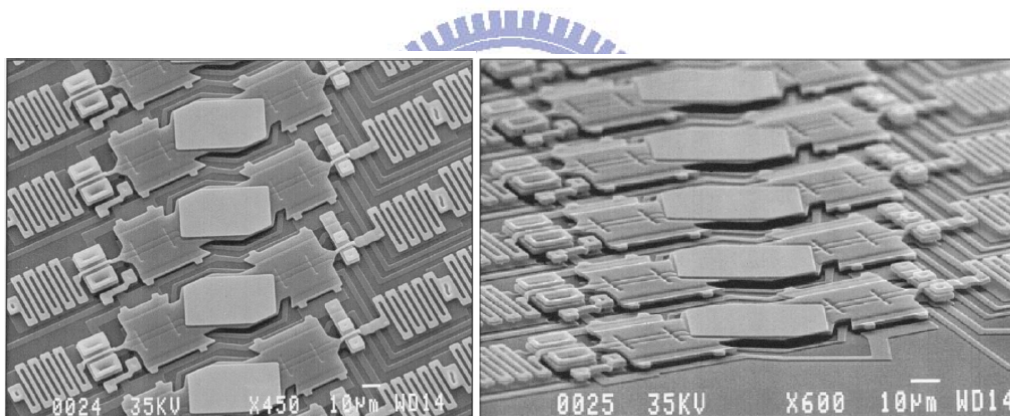


Figure 1-7. SEM micrographs of the mirror array actuated by parallel plate electrostatic force [6].

Kiang et al. presented an out-of-plane, lateral electrostatic combdrive-actuated micro scanning mirror [2]. Two types of scanning mirrors with horizontal and vertical scan were fabricated with two or three structural layers of polysilicon. As shown in Figure 1-8, the out-of-plane micro scanning mirror is suspended by the frame connected to a hinged slider in the back. Scanning is achieved by the linkage of the lateral combdrive to the mirror structure through a hinge that allows the linear motion

of the comb to be translated into the angular motion of the micro mirror. Maximum optical scan angles were up to $\pm 14^\circ$ for the vertical scanning mirror and $\pm 9^\circ$ for the horizontal scanning mirror by a 40 V ac voltage at resonant frequencies in the kilohertz range.

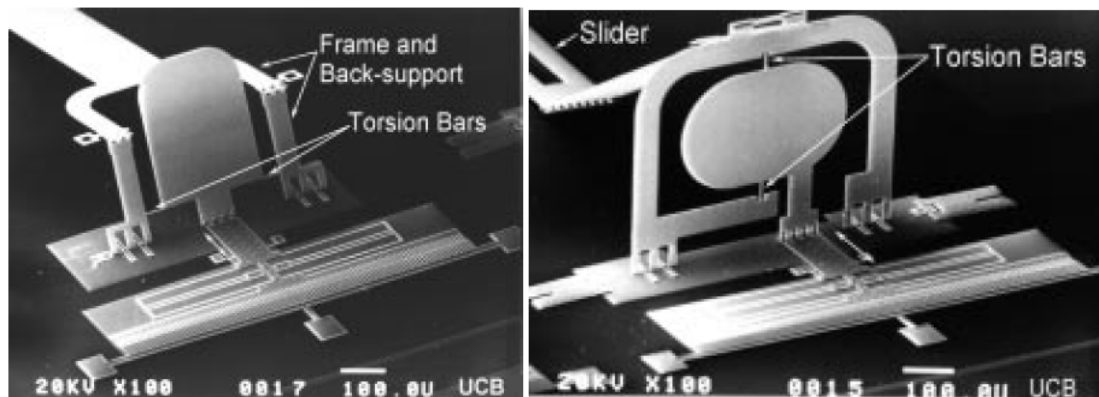


Figure 1-8. SEM micrographs of vertical and horizontal micro scanning mirrors [2].

1-2-1-2 Thermal actuation

Thermal actuator can be used to actuate micro scanning mirrors due to the difference in the coefficients of thermal expansion of the bimorph beam. When the current passes through the bimorph actuator, the generated heat can actuate the actuator. Compared to electrostatic or magnetic actuators, thermal actuator has relatively higher power consumption and lower switching speed.

Schweizer et al. presented a monolithic integrated thermal micro scanning mirror [7]. The device consists of a mirror located on the tip of a thermal bimorph actuator beam that is made of silicon dioxide and a thin film conductor. The residual stress in the two layers is used to achieve an out-of-plane rest position of the mirror, as shown in Figure 1-7. The device is excited electrothermally at its resonance frequency, enabling large angular deflections at low power consumption. Different length of the beams would generate different rest positions. The SEM micrographs are shown in Figure 1-9. Mirrors with resonant frequencies varying from 100 to 600 Hz were

realized. Mechanical scan angles of above 90° were achieved.

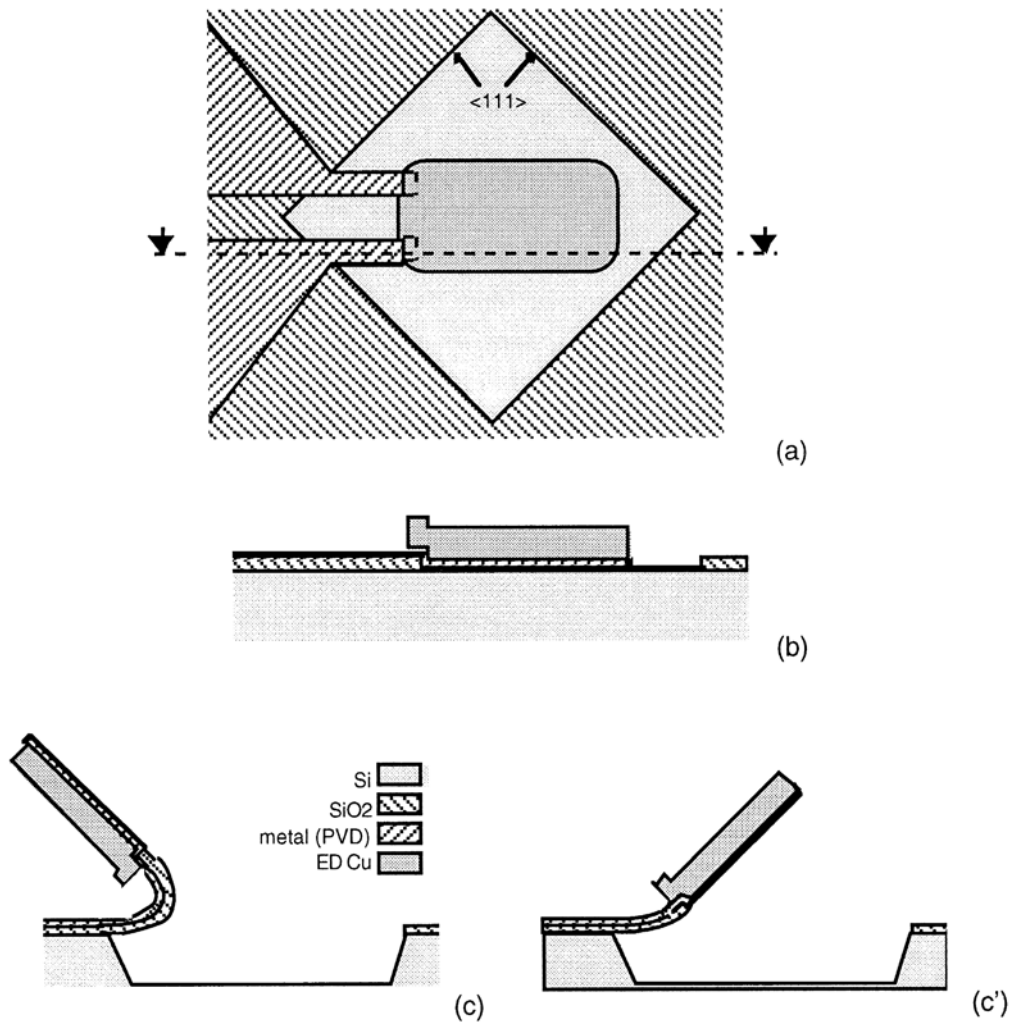


Figure 1-9. Schematic of the thermal actuator, (a) device top view, (b) cross-section of the device before release, (c) cross-section of the device after releasing the long beam, (c') cross-section of the device after releasing the short beam [7].

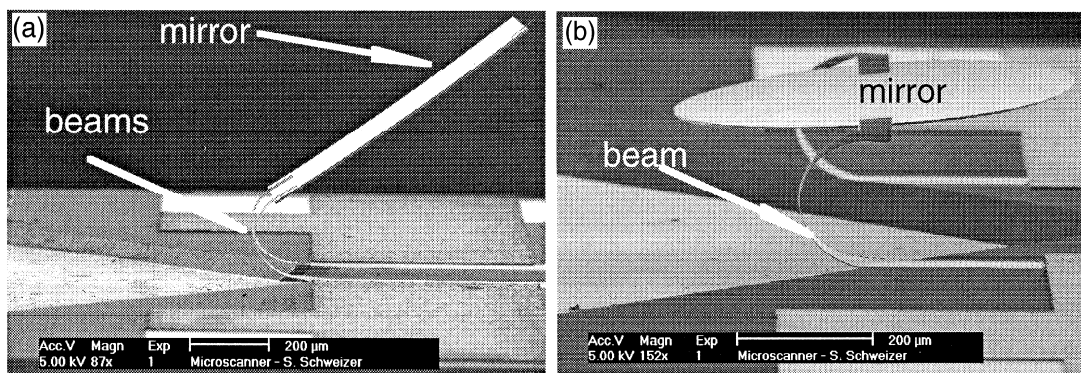


Figure 1-10. SEM micrographs of thermally actuated micro scanning mirror [7].

Singh et al. presented a two-axes thermally actuated SOI scanning mirror that consisted of a mirror plate, four flexural springs and four thermal actuators as shown in Figure 1-11 [8]. The thermal actuators were formed by using single crystal silicon and aluminum composite beams. When the beam was heated, it bent due to the difference in the coefficients of thermal expansion of the two materials. The SEM micrographs of the device are shown in the Figure 1-11. The measured maximum angular deflection was 17° at an applied voltage of less than 2 V.

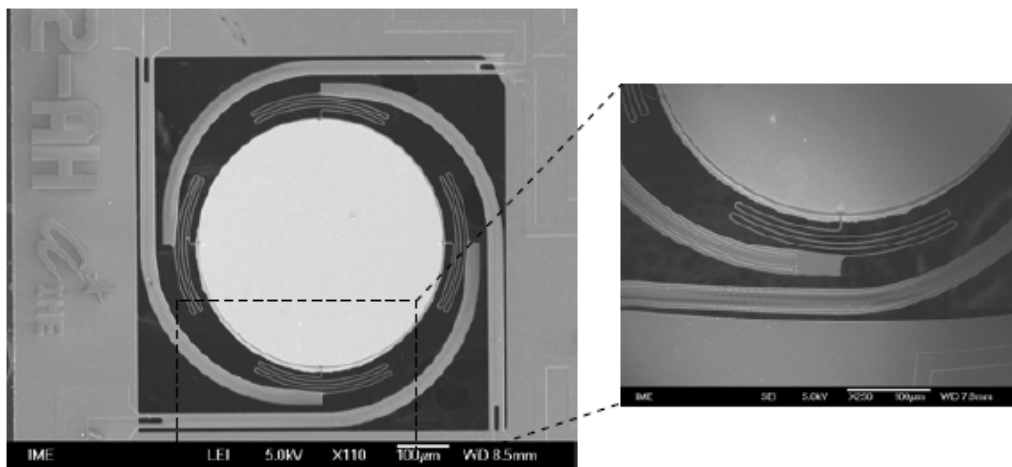


Figure 1-11. SEM micrographs of the thermally actuated micro scanning mirror [8].

1-2-1-3 Magnetic actuation

Magnetic forces can be applied to actuate microstructures by passing a current to generate the Lorentz forces or by coating magnetic materials like Permalloy on the structures. The magnetostatic force can be induced by the interaction of magnetic material and the magnetic field to drive the micro scanning mirror. Generally speaking, magnetic actuation provides higher switching speed, both attractive and repulsive forces, and large deflection angles, but the assembly of external magnets and coils is a big problem.

Miller et al. presented two types of magnetic scanning mirrors which combined magnetic thin films and silicon bulk micromachining [9]: (1) mirrors with permalloy

coating could only be controlled by an external magnetic field but did not experience thermal heating effects and (2) mirrors with both permalloy and copper coils also required an external field and could be operated by applying a current to the on-plate coils. The schematic and the micrographs of the mirrors are shown in Figure1-12 and Figure1-13. The 60° deflection range of both types of mirrors in an external field ($H = 23.9 \text{ kA/m}$) was achieved.

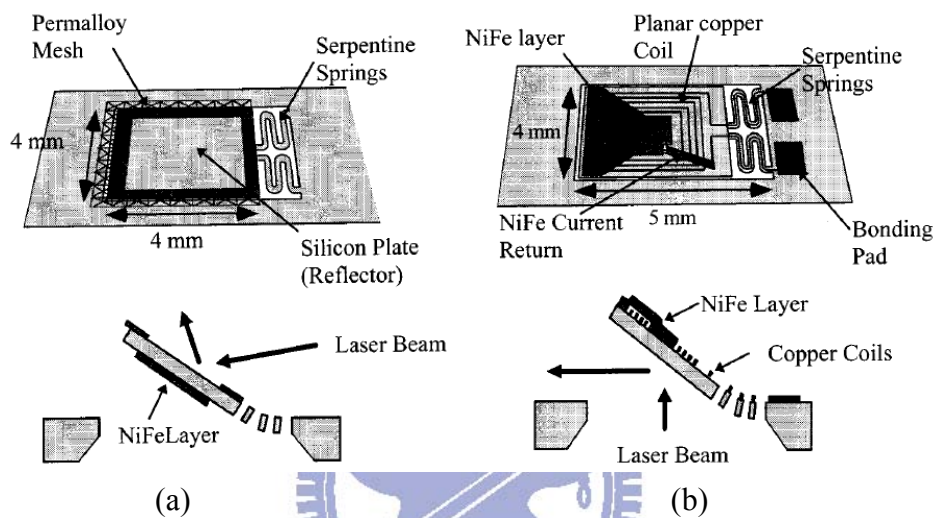


Figure 1-12. Schematic and side views of two types of magnetic scanning mirrors: (a) mirror with permalloy only and (b) mirror with permalloy and copper coils [9].

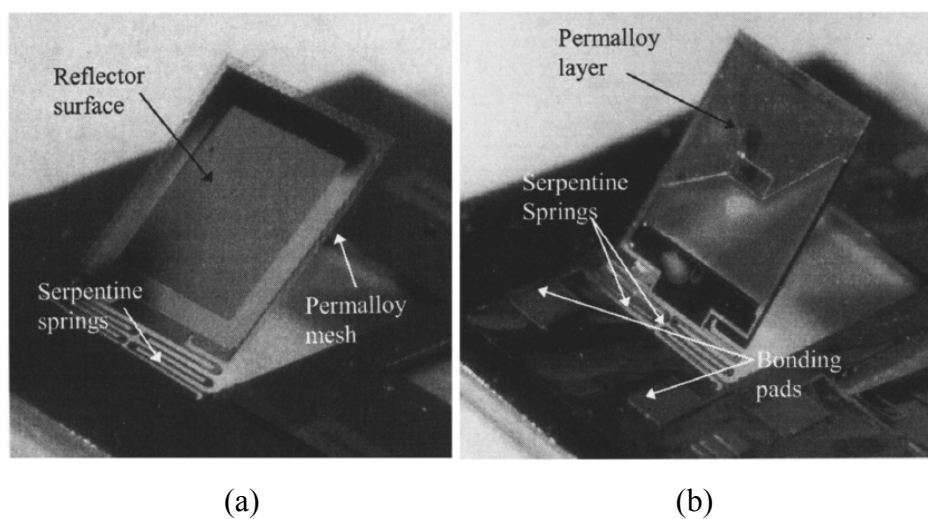


Figure 1-13. Micrographs of two types of magnetic scanning mirrors: (a) mirror with permalloy and (b) mirror with permalloy and copper coils [9].

Cho et al. presented a three-axis micro scanning mirror with large static angular and vertical displacements [10] as shown in Figure 1-14. The micro scanning mirror has z-axis linear motion as well as x-axis and the y-axis rotation as the schematic shows in Figure 1-15. The micro mirror consists of a gold coated mirror plate, incorporated actuation coils, frame and cantilever-type actuators with actuation coils. The actuator coils integrated on the mirror plate is used for the y-axis actuation and the other coil actuators integrated on the cantilevers are used for the x-axis and z-axis actuation. The maximum static deflection angles were measured as $\pm 4.2^\circ$ for x-axis actuation and $\pm 9.2^\circ$ for y-axis actuation, respectively. The maximum static vertical displacement was measured as $\pm 42 \mu\text{m}$ for z-axis actuation. The actuation voltages were below 3 V for all actuation.

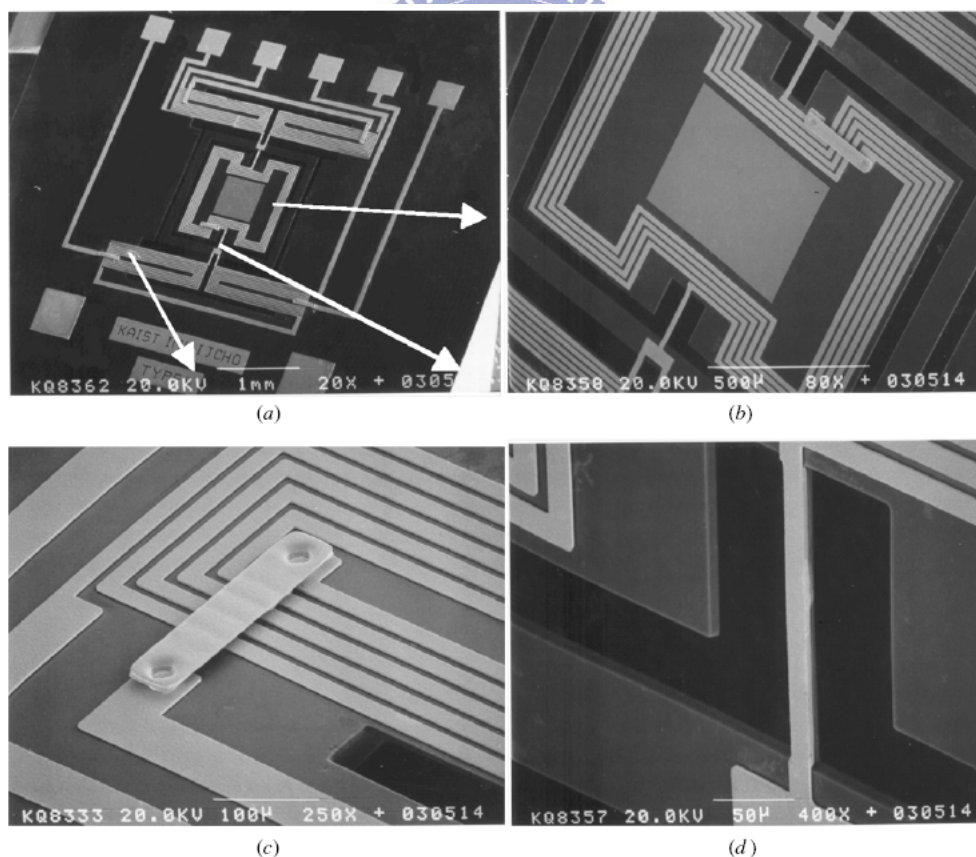


Figure 1-14. SEM micrographs of the fabricated mirror, (a) overall view, (b) enlarged view of the mirror plate, (c) electrical connection between two points and (d) torsion bar [10].

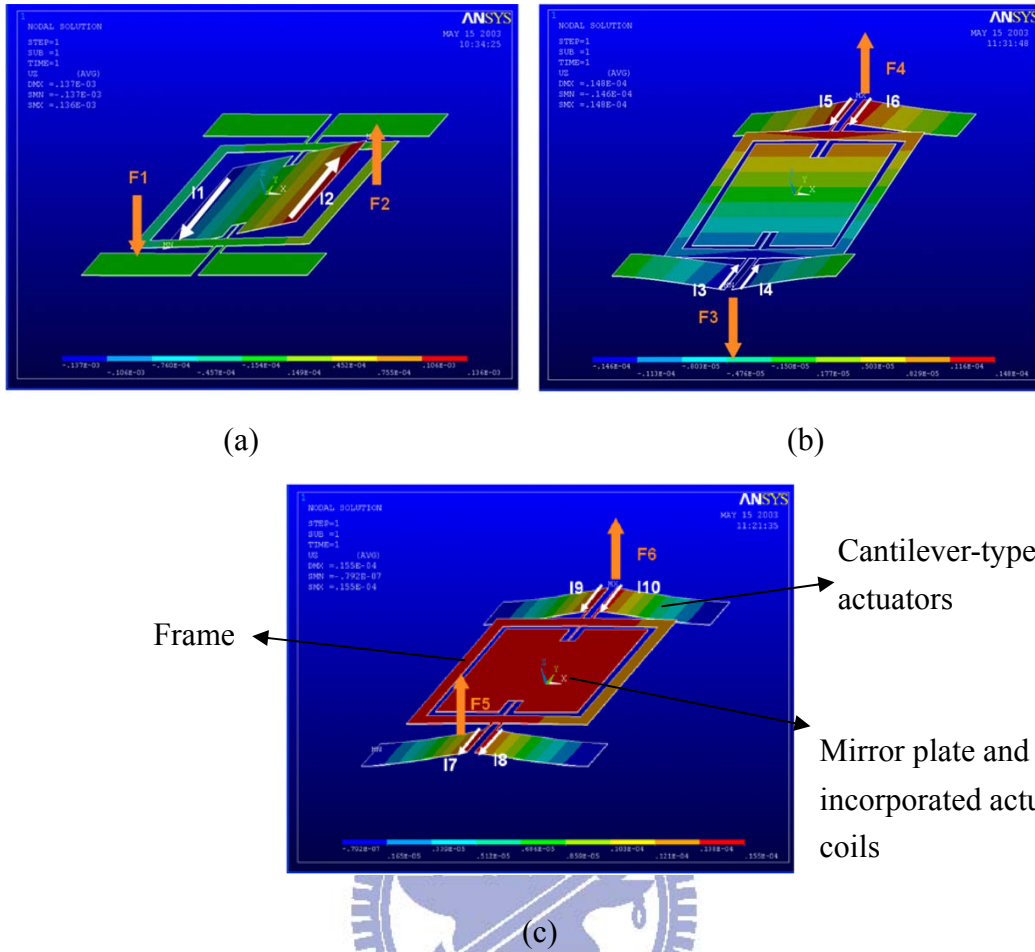


Figure 1-15. Operation principle of the magnetic scanning micro scanning mirror: (a) y-axis rotational actuation, (b) x-axis rotational actuation and (c) z-axis linear actuation [10].

Tang et al. presented a 2-axis magnetostatic SOI micro scanning mirror driven by a double-side electroplated ferromagnetic film [11]. The fabrication processes enabled simultaneous double-side electroplating to increase the volume of the ferromagnetic materials and enhance the force on the mirror. As shown in Figure 1-16, the magnetostatic force can be induced by the interaction of the ferromagnetic material and the magnetic field provided by the solenoid to drive the micro mirror. Figure 1-17 shows the SEM micrographs of a fabricated micro scanning mirror. The front side of the supporting frame contains the electroplated Ni with tilt-pattern design. The back side of mirror and supporting frame contains the electroplated Ni film. The outer scan

and inner scan of this 2-axis scanning mirror were respectively operated at 584 Hz with an optical scan angle of $\pm 6.6^\circ$ and 11149 Hz with an optical scan angle of $\pm 5.5^\circ$.

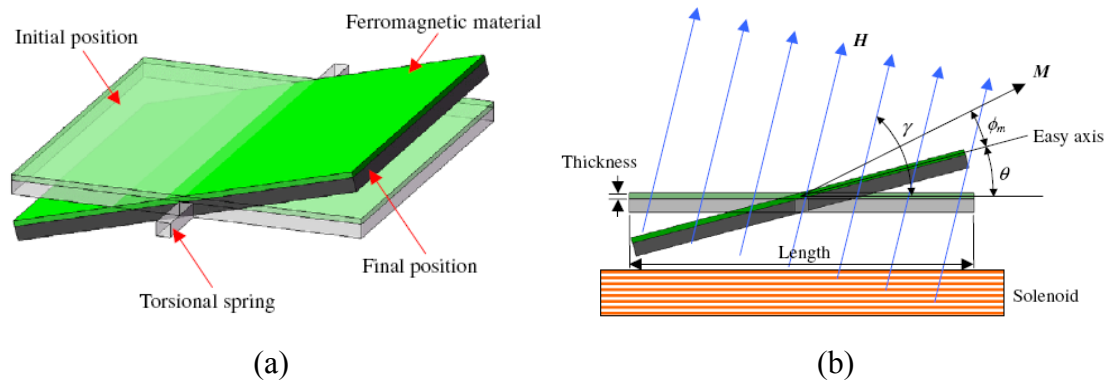


Figure 1-16. Actuation concepts of the magnetostatic mirror, (a) schematic and (b) cross-section view [11].

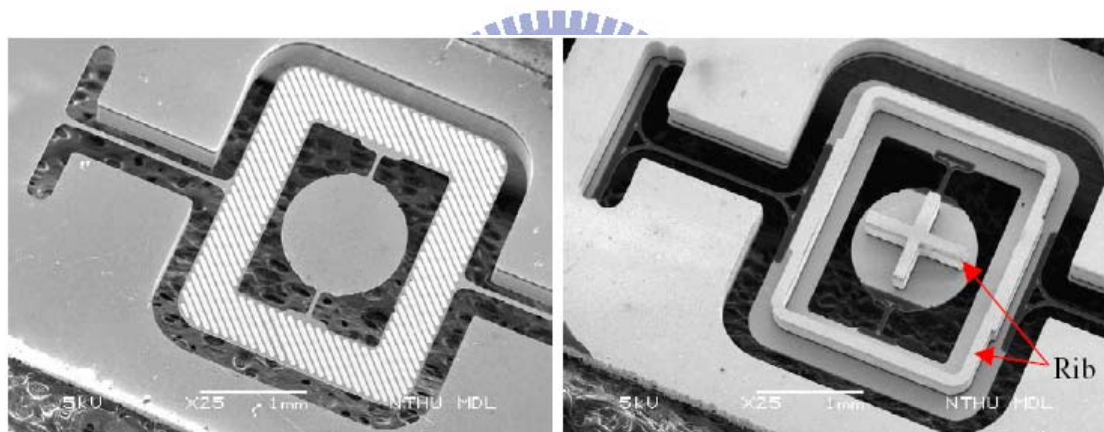


Figure 1-17. SEM micrographs of the magnetostatic mirror: (a) front side and (b) back side [11].

1-2-1-4 Summary

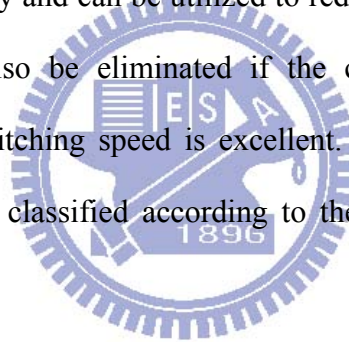
In many applications, electrostatic actuation is preferred due to its low power consumption. The power issue is important particularly in large array systems. But the parallel-plate electrostatic actuation suffers from the pull-in phenomenon. Thermal actuators have advantages of large deflection angles and simple fabrication processes. However, the switch speed is lower than other methods due to the thermal conduction.

Electromagnetic actuation can generate a relatively large force with lower voltage and provide good dynamic performance. Nevertheless, magnetic materials are not compatible with standard IC manufacturing and packaging the external magnetic may be an issue.

In addition to the above methods, another popular method is the vertical comb drive actuators. It has advantages over traditional electrostatic actuators. In the next section, various kinds of vertical comb micro scanning mirrors are reviewed.

1-2-2 Micro scanning mirror with vertical comb actuator

Many micro scanning mirrors driven by vertical comb actuators have been studied. They have large force density and can be utilized to reduce the actuation voltage. The pull-in phenomenon can also be eliminated if the comb geometries are chosen adequately. Besides, the switching speed is excellent. Micro scanning mirrors with vertical comb actuation are classified according to the fabrication processes in the following review.



1-2-2-1 Wafer bonding

This method starts with a silicon wafer or a SOI wafer. Deep reactive-ion etching (DRIE) is applied to make a comb finger set. Then another silicon wafer is bonded on the original wafer and etched back to make the other comb finger set.

Conant et al. presented a staggered torsional electrostatic combdrive (STEC) micromirror made of two layers of single-crystal silicon separated by a silicon dioxide layer [12]. The mirror, torsion hinge, and moving comb teeth are in the top silicon layer, and the fixed comb teeth are in the bottom silicon layer, as shown in Figure 1-18. The STEC micromirrors were fabricated using DRIE and a bond-and-etchback process, as shown in Figure 1-19. The micro scanning mirror has advantages of high

scan speed, small size, and low cost with diffraction-limited optical performance. The optical scan angle of $\pm 12.45^\circ$ at 34 kHz resonant frequency with 0.18mW power consumption can be achieved.

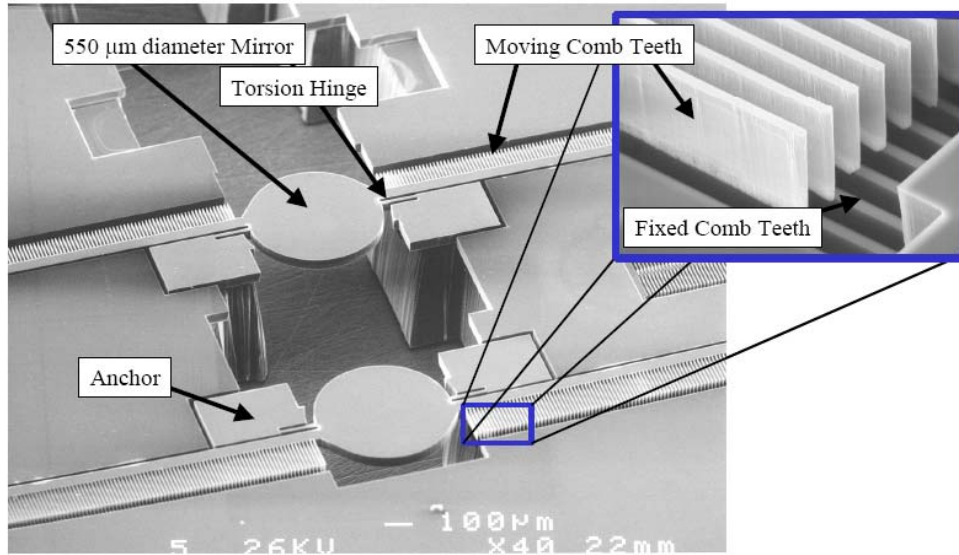


Figure 1-18. SEM micrograph of the STEC micro scanning mirror [12].

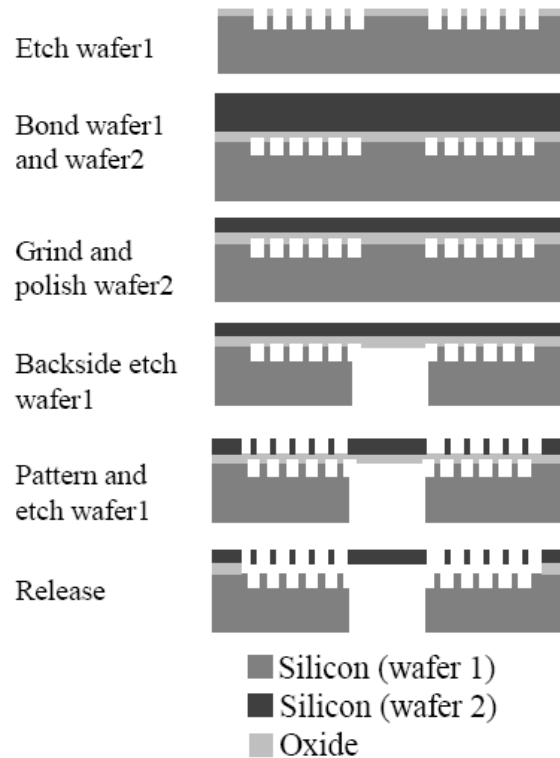


Figure 1-19. Fabrication flow of the STEC micro scanning mirror [12].

Lee et al. presented a micro mirror actuated by self-aligned vertical electrostatic combdrives with multi-level electrical isolation that allows bi-directional and dual-mode (independent rotation and piston motion) operation [13]. The fabrication flow is shown in Figure 1-20. The process starts with the coarse patterning of the bottom combteeth in SOI wafers. An unpatterned wafer is then bonded by thermal fusion bonding to the patterned SOI wafer. Next, two mask layers are deposited and patterned to define the contact area and the upper combteeth. The final steps are the DRIE of the upper and the lower combteeth. Figure 1-21 shows the SEM micrographs of the device. The micro scanning mirror with $\pm 9^\circ$ optical scanning with 155 V actuated voltage and 7.5 μm of piston motion with 110V actuated voltage were achieved. The resonant scanning has optical scan angles up to $\pm 25^\circ$ with a 96 V dc bias and 40V ac voltage at 13.5 KHz.

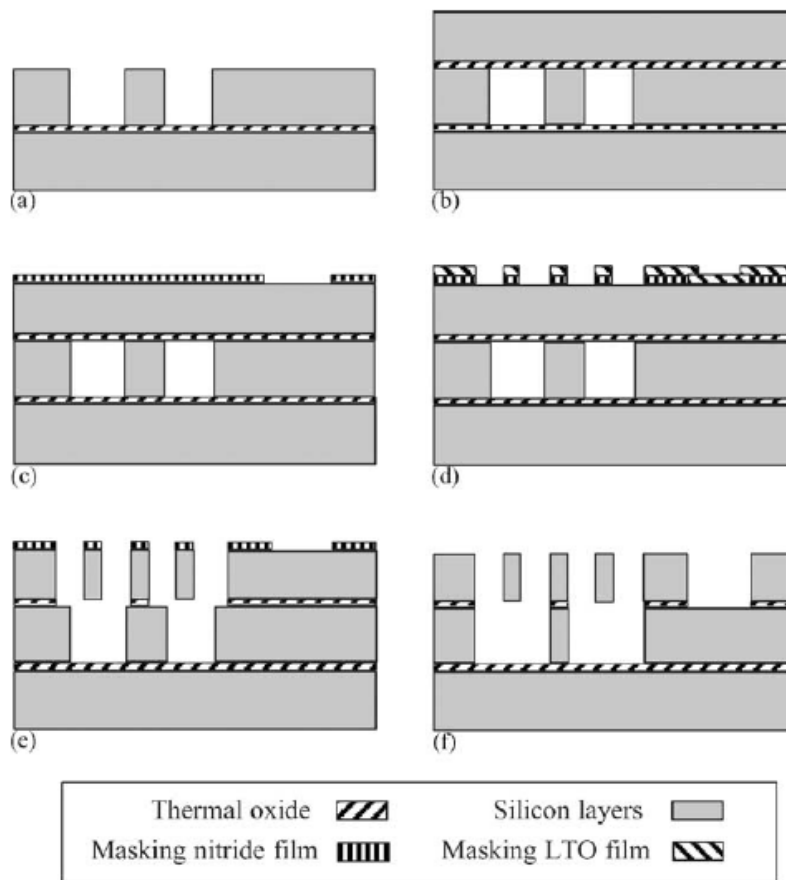


Figure 1-20. Fabrication flow of the self-aligned micro scanning mirror [13].

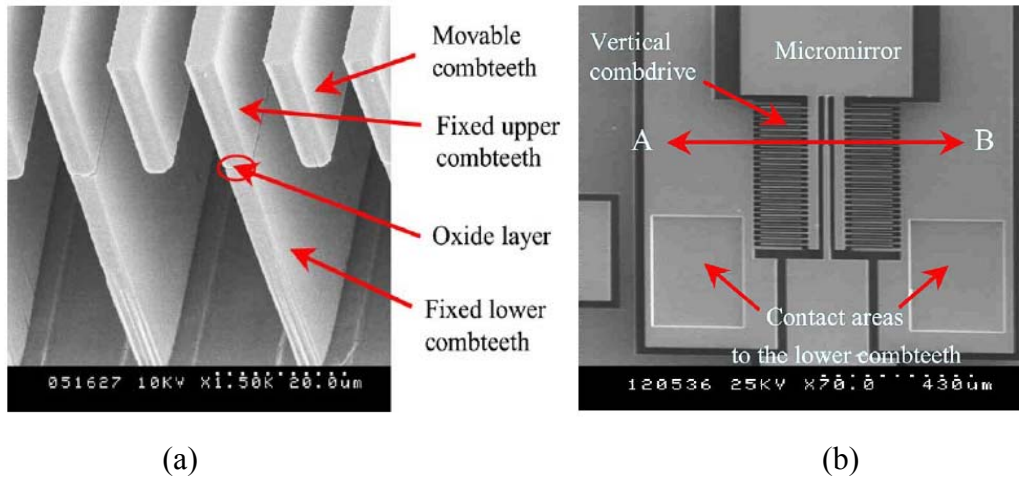


Figure 1-21. SEM micrographs of the dual-mode and double-stacked device: (a) self-aligned combteeth and (b) top view of the mirror [13].

Ra et al. presented a two-dimensional micro scanning mirror for dual-axes confocal microscopy [14]. The fabrication process of the mirror is the same as [13]. The cross-section schematic and SEM micrograph are shown in Figure 1-22. Maximum optical deflections of $\pm 4.8^\circ$ at 160 V and $\pm 5.5^\circ$ at 170 V are achieved in static mode for the outer and inner axes, respectively. The dynamic characterization was measured with a 77 V dc bias and a 58 V ac voltage. Torsional resonant frequencies are at 500 Hz with $\pm 12.4^\circ$ optical deflection and at 2.9 kHz with $\pm 7.2^\circ$ optical deflection for the outer and inner axes, respectively.

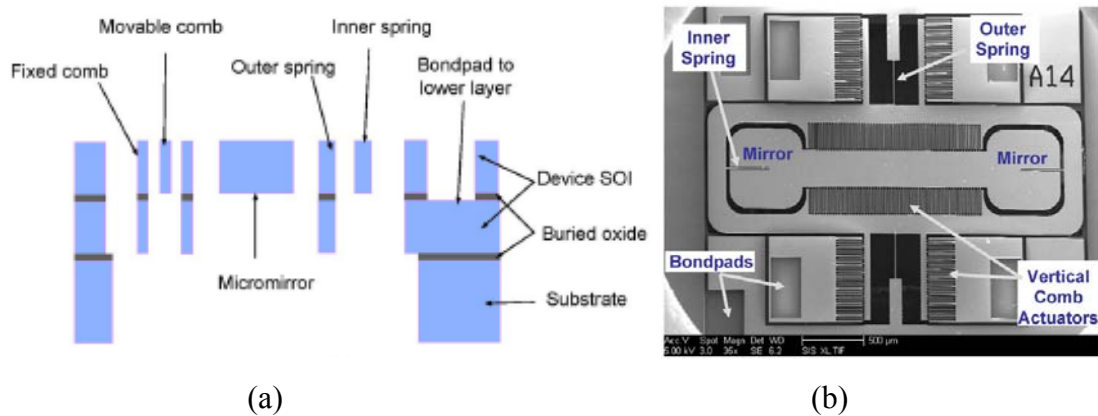


Figure 1-22. Schematic and SEM of the two dimensional self-aligned scanning mirror: (a) cross-section schematic and (b) SEM micrograph [14].

The upper and lower comb fingers of the micro scanning mirror can also be fabricated individually on two substrates by the front side and back side DRIE, bonding, polishing, metal coating, electroplating, and releasing processes. And then the upper and the lower finger were bonded with each other with a fine flip chip bonder. The whole fabrication processes are too complicated in spite of the good performance. The complicated flow was applied in the following two works.

Lee et al. presented a micro scanning mirror for laser display systems [15]. Figure 1-23 and Figure 1-24 show the basic structure and the assembly process of the scanning mirror. It is composed of two structures. The upper structure is composed of a scanning mirror plate, two torsion bars, a supporting frame and upper comb fingers. The lower structure is composed of lower comb fingers, a supporting frame, gold signal lines and pads on a Pyrex glass substrate. The comb fingers are beneath the mirror to increase the fill factor. Figure 1-25 shows the upper structure with a bonded glass plate. The $\pm 6^\circ$ optical scan angle was obtained when driven by a 28V ac control voltage at 60 Hz with a 35 V dc bias voltages.

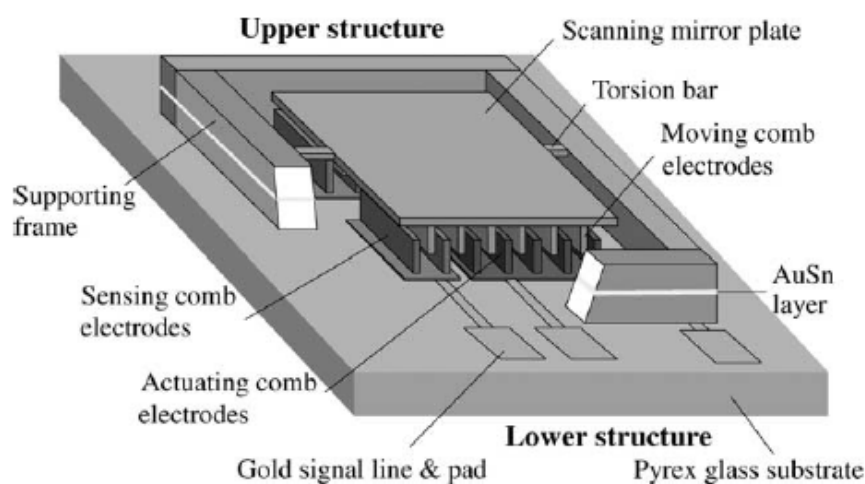


Figure 1-23. Basic structure of the two-structure bonded scanning mirror [15].

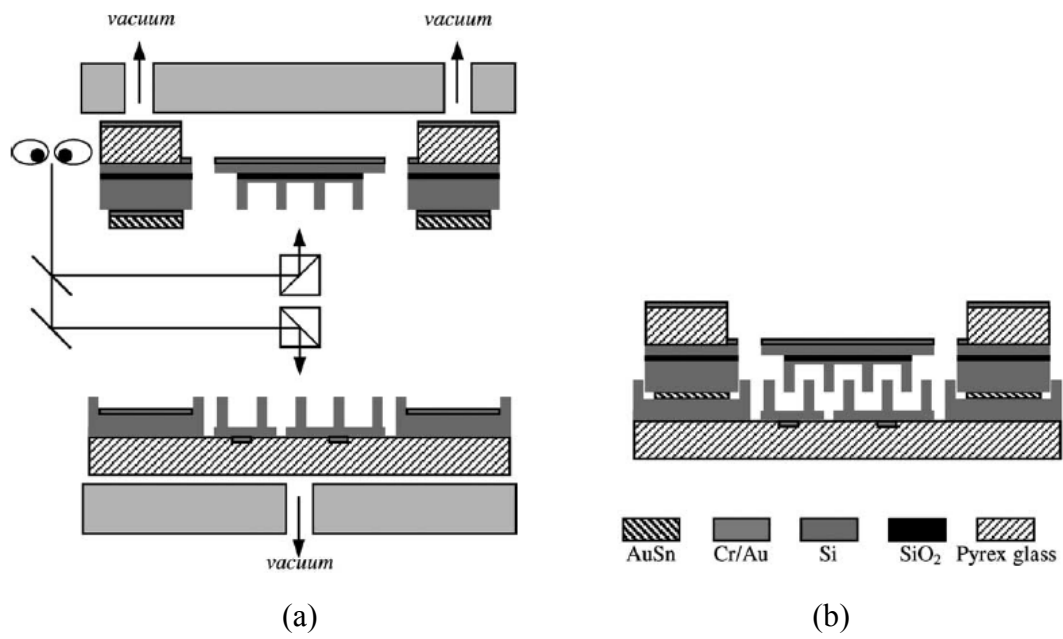


Figure 1-24. Assemble processes of the two-structure scanning mirror: (a) alignment and (b) eutectic bonding [15].

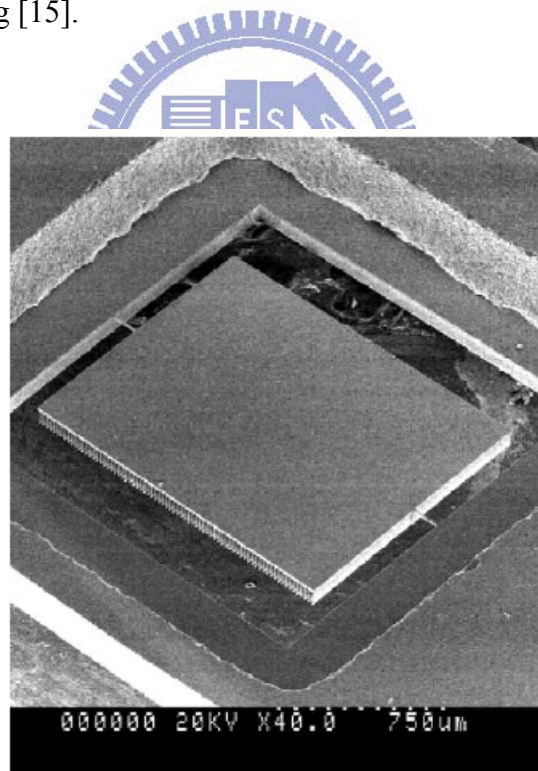


Figure 1-25. SEM micrograph of the upper structure with a bonded glass plate [15].

Ko et al. demonstrated an eye-type micro scanning mirror for laser display [16]. The micro scanning mirror consists of a circular mirror plate and an elliptic outer frame with vertical combs to increase the number of fingers. This eye-type mirror showed larger deflection angle compared to the traditional works using rectangular mirrors. But the fabrication flow is complicated. Figure 1-26 shows the SEM micrographs of the structure. The $\pm 16^\circ$ optical scanning angle was achieved when driven by the 65-75 V sinusoidal control voltage and a 100 V dc bias at resonant frequency of 22.1-24.5 kHz.

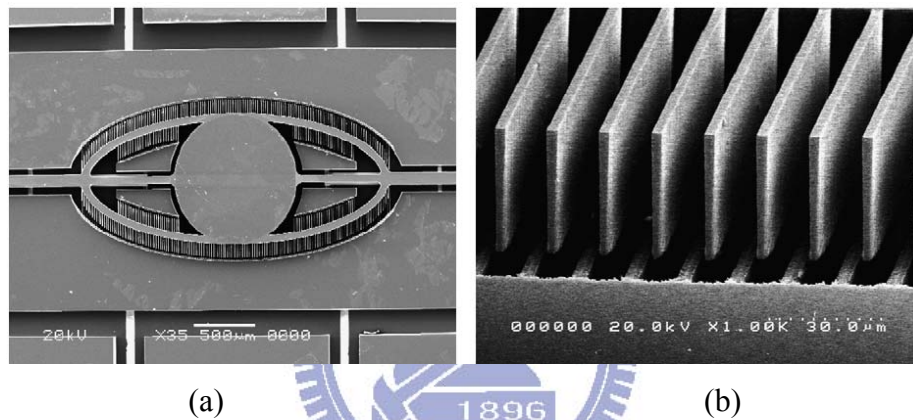


Figure 1-26. SEM micrographs of the eye-type micro scanning mirror: (a) upper view and (b) enlarged view of the combteeth [16].

1-2-2-2 Multi-mask etching

This method employs a delay-mask process (DMP) in the fabrication process. The concept is shown in Figure 1-27. After multiple mask layers are patterned, the main layer is etched to a certain depth with all masking layers and then the topmost mask 1 is removed. Then, the main layer is etched again and the next masking layer is removed. This procedure is repeatedly until all the masking layers are removed. The vertical offset between the upper and the lower comb fingers can be achieved by applying the DMP. The comb fingers made by DMP are self-aligned. Self-alignment between moving and fixed fingers is important in order to avoid lateral instability

leading to an in-plane pull-in during actuation.

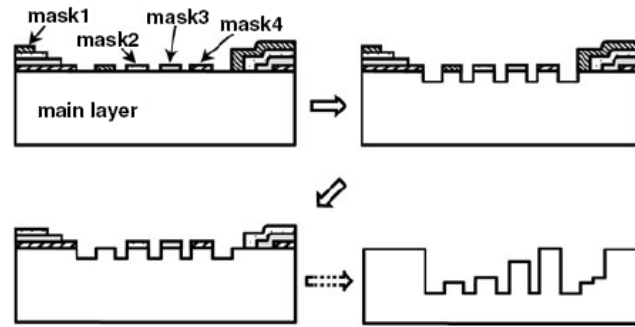


Figure 1-27. Concept of the delay-mask process [17].

Hah et al. presented a self-aligned vertical comb-drive actuator for a two-axis micro scanning mirror [17]. This work applied DMP to achieve self alignment between the moving and the fixed fingers. This method was also useful to fabricate comb fingers with narrow gap spacing and reduce the operation voltage. Figure 1-28 shows the SEM micrographs of the mirror. The DC mechanical scan angles of the micro scanning mirror were measured as $\pm 2.1^\circ$ at 48V around the inner axis and $\pm 1.8^\circ$ at 44 V around the outer axis, respectively. The mechanical resonant frequencies of 1.2 kHz around the inner axis and 0.9 kHz around the outer axis were measured, respectively.

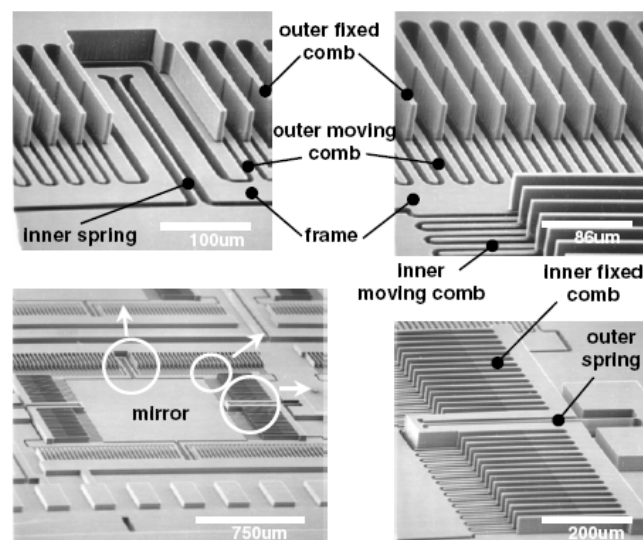


Figure 1-28. SEM micrographs of a micro scanning mirror fabricated by DMP [17].

Kim et al. presented a two-axis micro scanning mirror array with high fill-factor [18]. In order to achieve high fill-factor, the mirror plate is mounted on a self-aligned vertical comb drive actuator achieved by the DMP. The schematic of the micro scanning mirror is shown in Figure 1-29. Figure 1-30 shows the SEM micrographs of the mirror array. The maximum static optical deflections are $\pm 2.16^\circ$ at 60 V bias for the outer axis and $\pm 1.41^\circ$ at 96 V bias, respectively. The torsion resonant frequencies along the outer and inner axes were 1.94 kHz and 0.95 kHz, respectively.

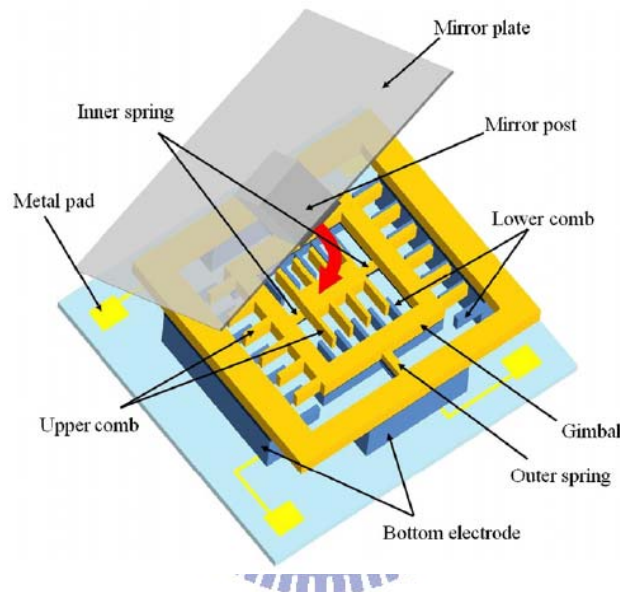


Figure 1-29. Schematic view of the micro scanning mirror with high fill-factor [18].

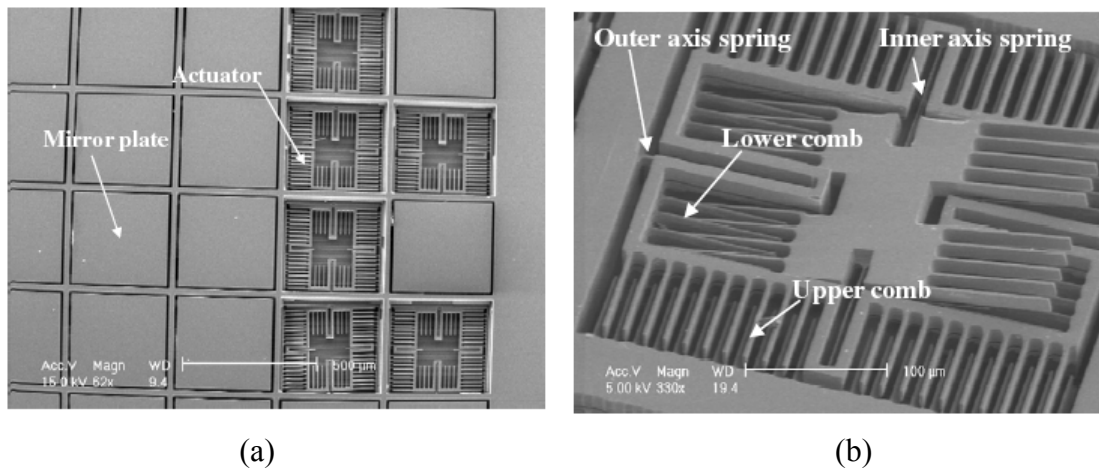


Figure 1-30. SEM micrographs of the scanning mirror with high fill-factor: (a) mirror array, (b) vertical comb actuator [18].

1-2-2-3 Offset by self assembly

Vertical offset between the upper and the lower comb fingers can be achieved by self assembly. Since the upper and lower comb fingers are fabricated on the same layer, they are self-aligned and the gap can be minimized.

Patterson et al. presented a micro scanning mirror with self-aligned comb fingers patterned in a single etching process [19]. In the fabrication processes shown in Figure 1-31, the self-aligned comb fingers are rotated out of the wafer plane by the surface tension of the reflowed photoresist. The fabrication processes are relatively simple compared to other methods. Figure 1-31 shows the SEM micrograph of the micro scanning mirror. The resonant optical scan angle of $\pm 18^\circ$ was measured with a 21 V sinusoidal input at 1.4 kHz.

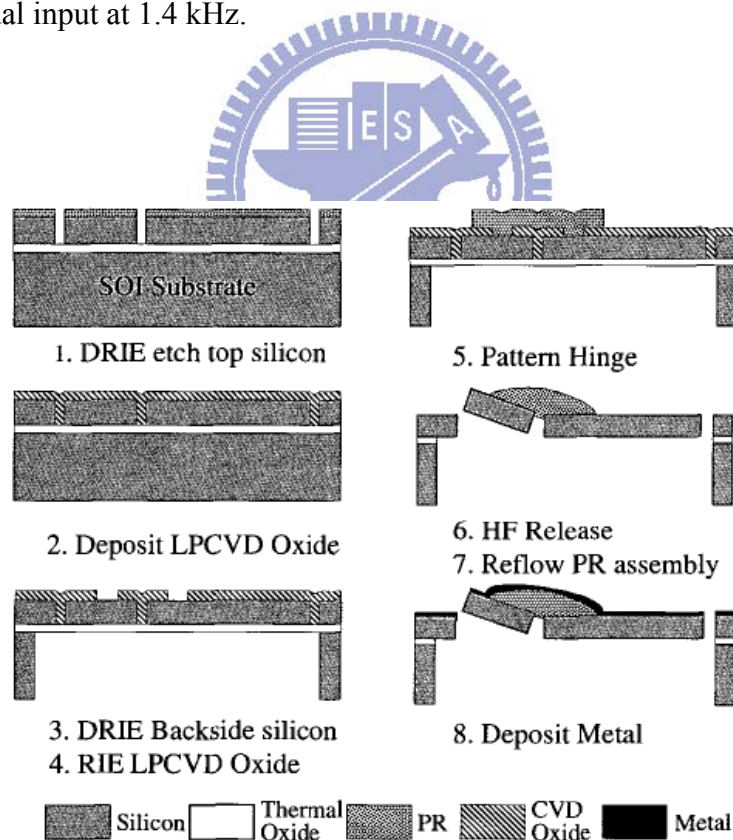


Figure 1-31. Fabrication processes of the self assembly vertical comb actuator [19].

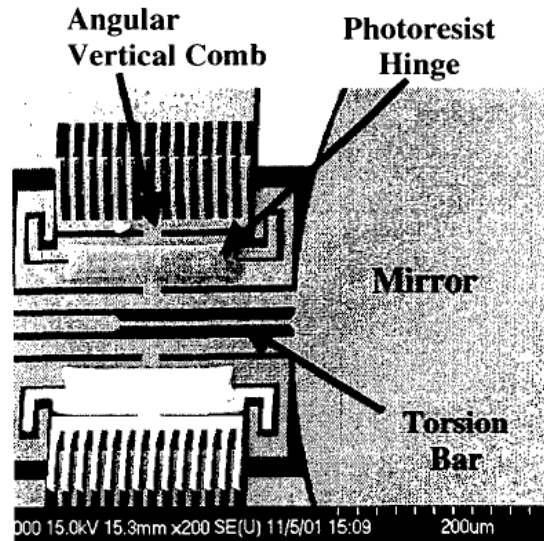


Figure 1-32. SEM micrograph of a scanning mirror with self assembly vertical comb drive [19].

Jeong et al. presented a self-aligned vertical comb drive fabricated in the device layer of a SOI wafer [20]. As Figure 1-33 shows, the fixed combs are anchored to bimorph cantilevers made of two materials with dissimilar thermal coefficients of expansion. The cantilevers, which provide the vertical offset between the fixed combs and the moving combs, are deflected by the residual stress during cooling down from the oxidation temperature to the room temperature. The deflection of the bimorph cantilever provides the initial offset between the moving and the fixed comb fingers. The fabrication processes are relatively simple. However, the fill-factor is low due to the large areas of the cantilever beam and the comb fingers. Figure 1-32 shows the SEM micrograph and schematic diagram of self-aligned vertical comb fingers. The optical deflection angle was $\pm 3.25^\circ$ by a 5.5 V dc bias and 10 V ac voltage at the resonant frequency of 830 Hz.

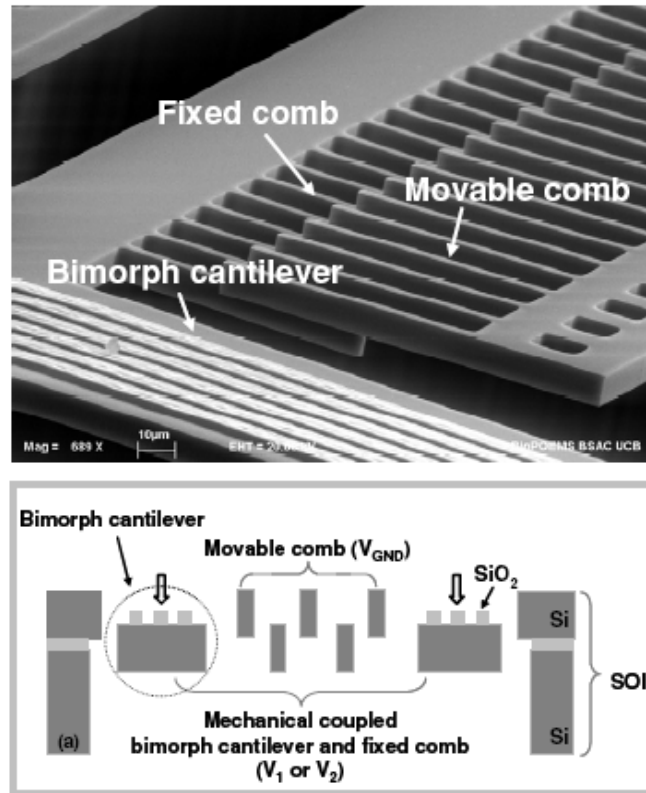
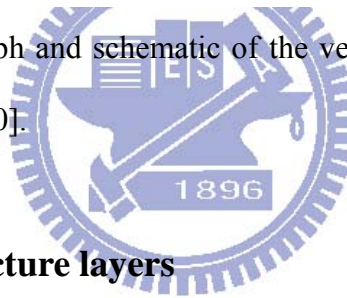


Figure 1-33. SEM micrograph and schematic of the vertical comb actuator achieved by the bimorph cantilever [20].



1-2-2-4 Multiple structure layers

The standard processes like Sandia's ultraplanar multilevel MEMS technology-V (SUMMiT-V) processes, which provide well-understood and documented properties, can be applied to fabricate the scanning mirror. The SUMMiT-V fabrication process is a five-layer polycrystalline silicon surface micromachining process. In this section, a micro scanning mirror using the standard processes is reviewed.

Hah et al. presented a surface-micromachined scanning mirror array with hidden vertical comb actuators [21]. The fixed fingers consist of poly1 and poly2 layers, and the movable fingers are made of the poly3 layer. The mirror plate is fabricated on the top polysilicon layer. The mirror, moving fingers, and torsion springs are connected to a ground plane. The actuation voltage is applied to the fixed fingers. The micro

mirrors provide large DC scan angle, low-operating voltage and high fill factor by the underneath vertical comb actuator. In spite of the good performance, it might suffer from the pull-in phenomenon between the mirror plate and the underneath comb fingers. Figure 1-34 shows the schematic of two types of mirrors. Type I has one set of vertical combs underneath the mirror. Type II has two sets of vertical comb-drives at two different levels; one underneath the mirror and the other attached to the edges of the mirror. Figure 1-35 shows the SEM micrographs. A $\pm 11.8^\circ$ DC optical scan angle with 6 V actuating was achieved. The measured resonant frequency of the mirror ranges from 3.4 to 8.1 KHz.

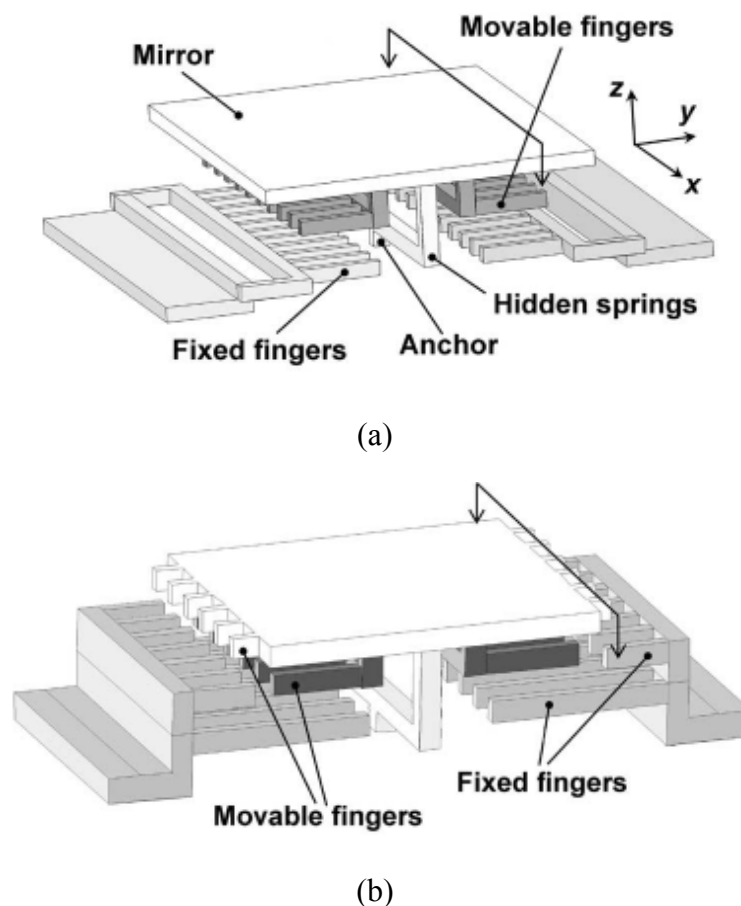


Figure 1-34. Schematic view of two types of mirrors, (a) type I device has one level of comb-drives and (b) type II device has two levels [21]

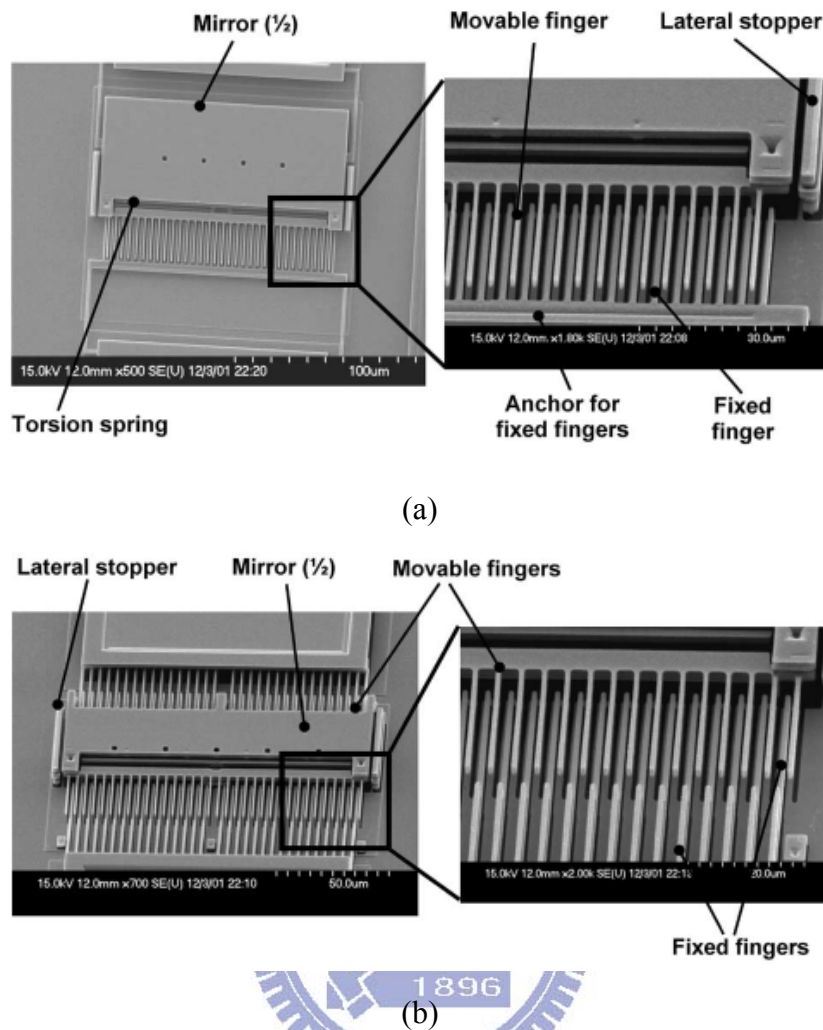


Figure 1.35. SEM micrographs of the mirror, (a) type I device has one level of comb-drives (b) type II device has two levels [21].

Multiple structure layers can be formed by deposited thin films. The small thickness of commonly-used thin films such as polysilicon limit the static rotation angle.

Tsou et al. presented a multi-layer process to fabricate micro scanning mirrors with self-aligned electrostatics dual combdrives [22]. The schematic of the structure is shown in Figure 1-36. The deposited silicon nitride and polysilicon are used as the insulation layer and the upper comb fingers, respectively. The device layer of the SOI wafer forms the lower comb fingers. The moving and the fixed comb fingers are

divided into six individual electrodes that can be used to produce bi-directional rotation and both upward and downward vertical piston motions. The working principle is illustrated in Figure 1-37. Figure 1-38 shows the SEM micrograph of the micro scanning mirror. The mechanical tilt angle of $\pm 1^\circ$ at 100 V dc bias was achieved. The micro scanning mirror can scan an angle of 62° at the resonant frequency of 10.46 kHz with a 60 V sinusoidal input.

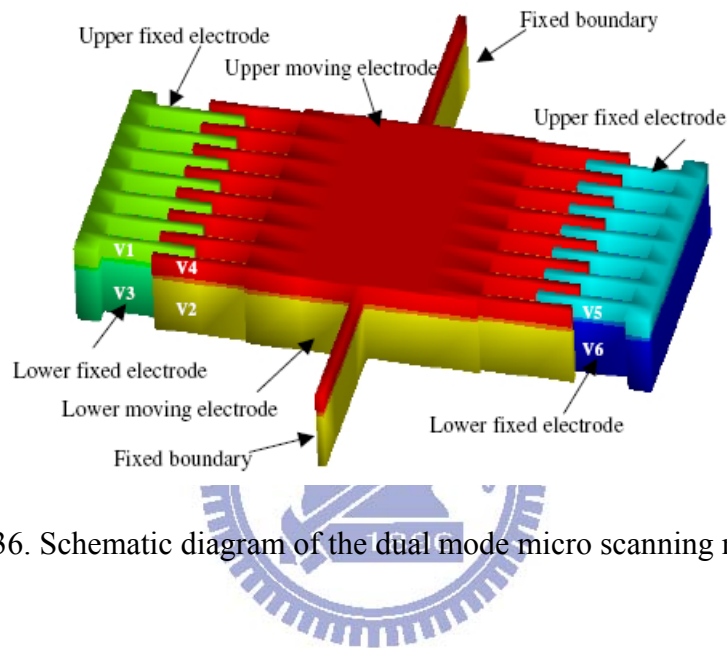


Figure 1-36. Schematic diagram of the dual mode micro scanning mirror [22].

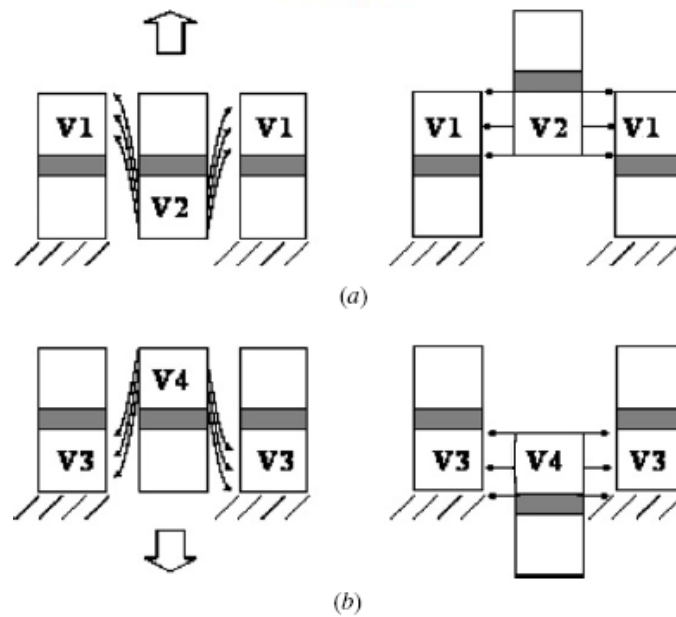


Figure 1-37. Principle of the vertical combdrive actuator, (a) upward actuation and (b) downward actuation [22].

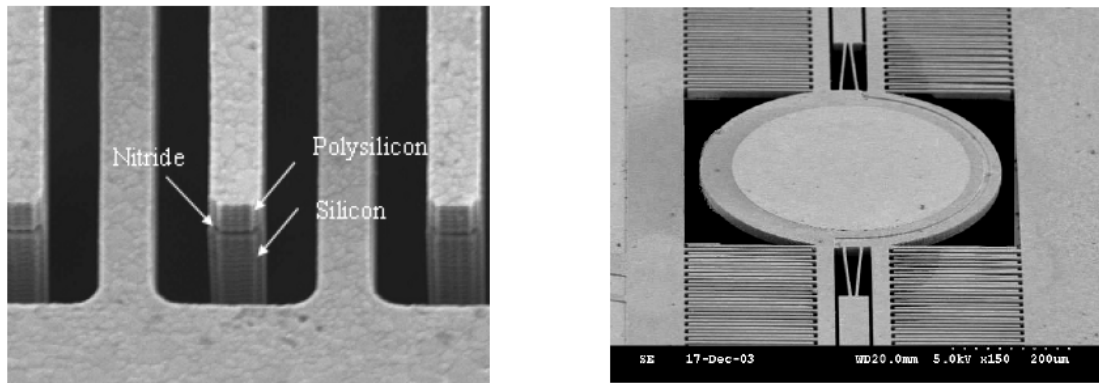


Figure 1-38. SEM micrograph of the dual mode micro scanning mirror [22].

1-2-2-5 Summary

Many kinds of vertical comb actuators were reviewed. The wafer bonding method provides good performance but needs fine aligned bonder. The multi-mask etching method provides a relatively simple fabrication process and compatible with the IC manufacturing but the performance would be worst than other methods. Offset by self assembly also provides a relatively simple fabrication process, but the assembly must be well controlled or it would fail during the assembly process. The standard process with multi structure layers provides good performance but the design flexibility is limited by the fixed fabrication process. Multiple structure layers formed by deposited thin films provide a simple fabrication process but the performance is limited by the thickness of the deposited layer. Furthermore, all these vertical comb actuated micro scanning mirrors are assembled in the plane of the wafer. In order to fabricate a flip-up micro scanning mirror, various out-of-plane assembly methods are reviewed in the next section.

1-2-3 Micro assembly

Micro structures fabricated by surface micromachining have to be flipped up to form 3-D structures. Scratch drive actuators [23], thermal actuators [24], electrostatic force generated by the parallel plate [25] or ultrasonic waves [26], magnetic force [27], centrifugal force [28], residual stress [29], and surface tension [30] have been used for self-assembly. In addition, manual assembly by the microprobes [31] and robot-assisted assembly [32] have been proposed.

In our previous work [5], flip-up micromirrors with arbitrary angles had been fabricated and assembled by the simple push method. The push method has large probe positioning tolerance in both vertical and lateral directions to reduce assembly failure. Figure 1-39 shows the assembly process of a 45° micromirror. Two push operations are needed in the assembly process. First, Probe 1 pushes the support to over 60° and hold in this position (Figure 1-39 (a)). Then Probe 2 pushes the mirror plate to 40° to 50° (Figure 1-39 (b)). Subsequently Probe 1 is removed and the torque from the torsional beams drives the support to lie on the mirror plate (Figure 1-39 (c)). After Probe 2 is removed, the torque of the torsional beams connected to the mirror plate also drives the mirror plate to lie on the support. Finally, the support and the mirror plate are interlocked (Figure 1-39 (d)). Figure 1-40 shows the SEM micrographs of our previous work.

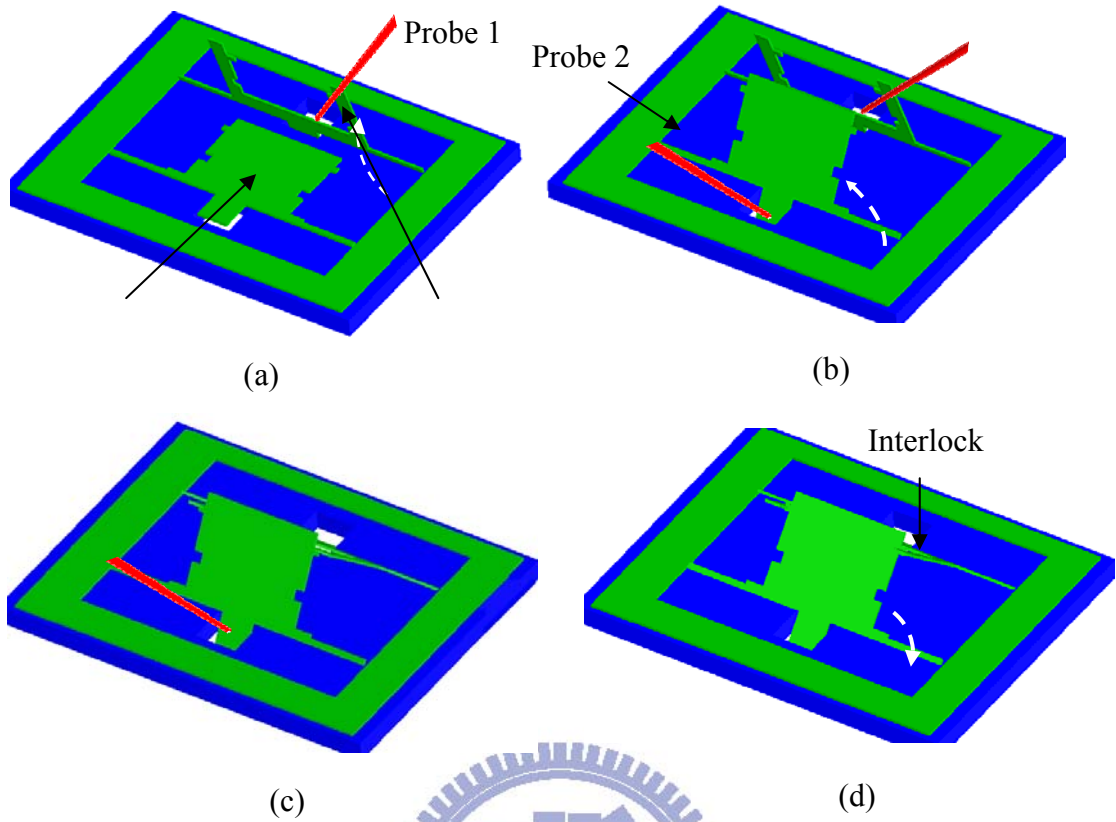


Figure 1-39. Schematic of the simple push assembly flow [5].

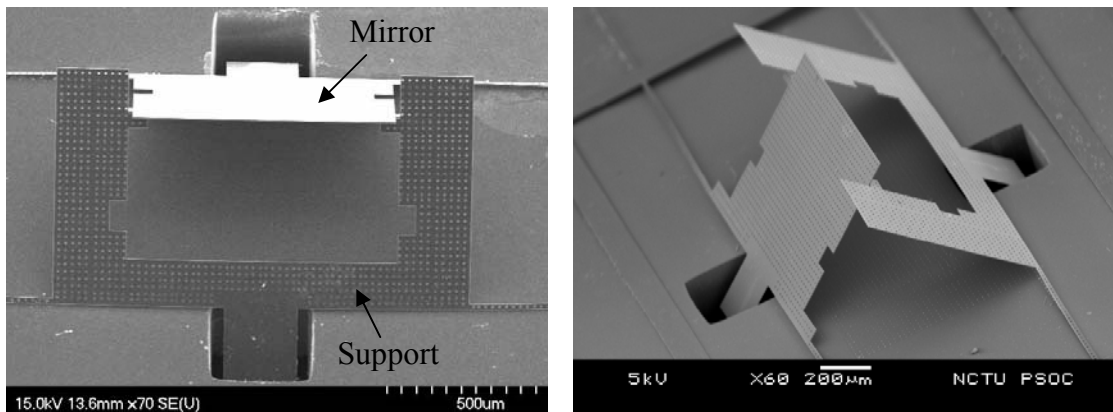
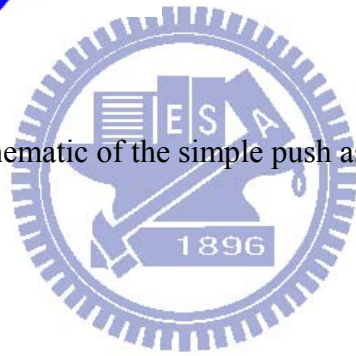
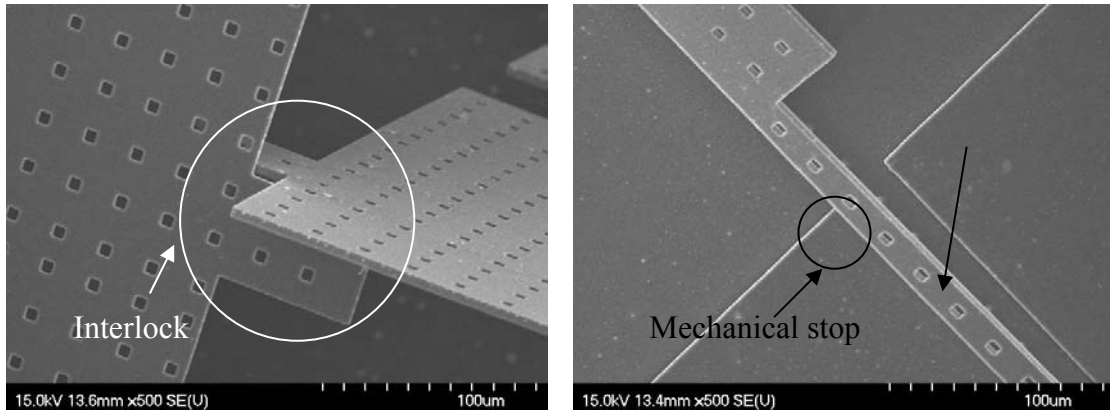


Figure 1-40. An assembled 45° device, (a) top view, (b) side view.



(c)

(d)

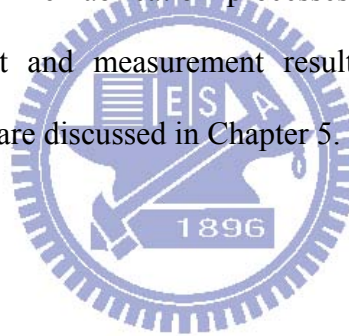
Figure 1-40. An assembled 45° device (continued), (c) interlock, (d) torsional beam of the mirror plate with mechanical stop.



1-3 Objective and organization of the thesis

Many micro scanning mirrors assembled in-plane have been demonstrated. They provide good performance and have been commercialized. But flip-up micro scanning mirrors are rare and still have room for improvement. MEMS-based flip-up microstructures can be integrated on a bench to realize the miniaturized optical system. The proposed MEMS-based optical pickup is a good example [5]. Therefore, the main objective in the thesis is to develop flip-up micro scanning mirrors assembled by the simple push operation. The flip-up micro scanning mirror can be integrated in the optical pickup unit to realize tracking.

The basic principle and simulation of the proposed flip-up micro scanning mirror are depicted in Chapter 2. The fabrication processes and issues are discussed in Chapter 3. The experiment and measurement results are shown in Chapter 4. Conclusion and future work are discussed in Chapter 5.



Chapter 2

Principle and Design

2-1 Introduction

The proposed flip-up micro scanning mirror is actuated by vertical comb actuators and assembled by the simple push assembly method [5]. The mirror is fabricated on the SOI wafer, whose single-crystalline-silicon device layer has good surface smoothness suitable for optical mirrors. The buried oxide layer of the SOI wafer is the etching stop for the deep reactive-ion etching process. Therefore, the thickness of the torsional spring is uniform in the SOI-based fabrication processes. SU-8 photoresist is used for the vertical offset between the moving and fixed combs due to its high aspect ratio and vertical sidewalls [33].

As shown in Figure 2-1, the devices consist of mirror supports, torsional beams, and plates with vertical comb drives. The moving comb fingers are made of the device layer of the SOI wafer; the fixed comb fingers are made of the SU-8 photoresist stacked on the device layer. It is easy to modify the thickness of the SU-8 photoresist between 1 μm to 100 μm to control the rotational angle. The moving comb fingers attached to the mirror are electrically grounded. The fixed comb fingers are the driven electrodes. The mirror plate is actuated by the induced strong fringe field between the fingers. The electrical isolation is realized by dividing the moving and fixed combs into two parts. The isolated parts are connected mechanically by the substrate of the SOI wafer. The topside, backside and cross-section views are shown in Figure 2-2.

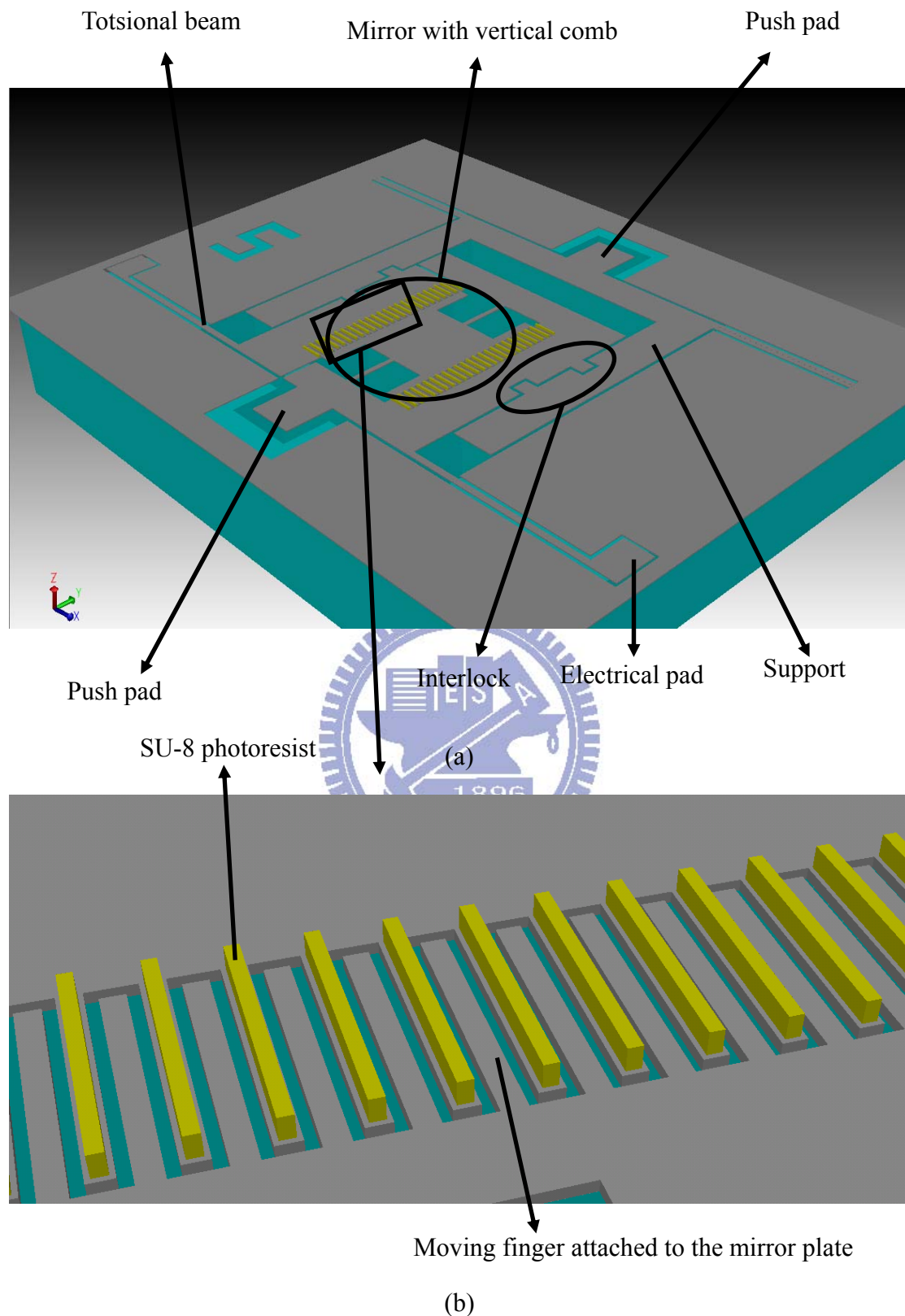
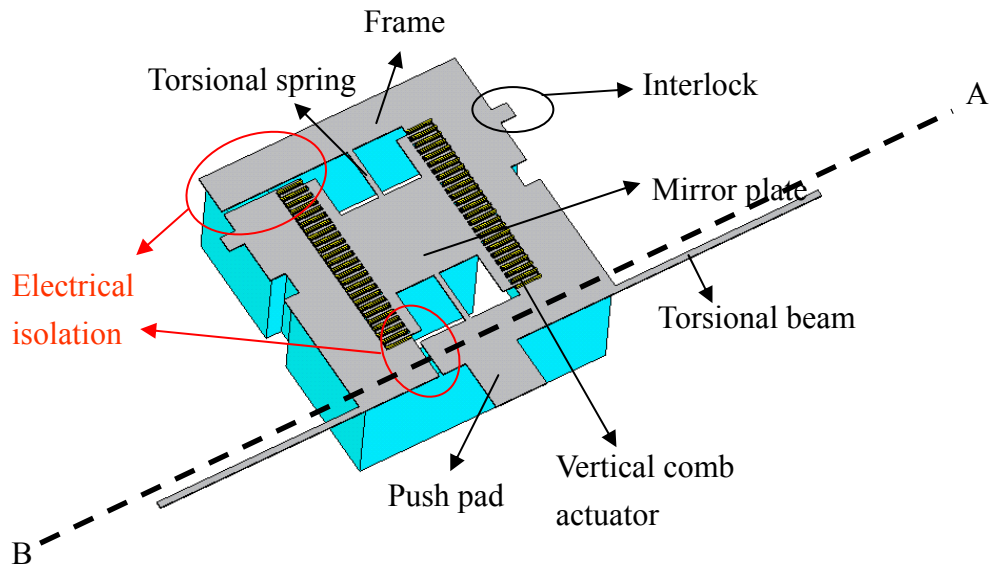
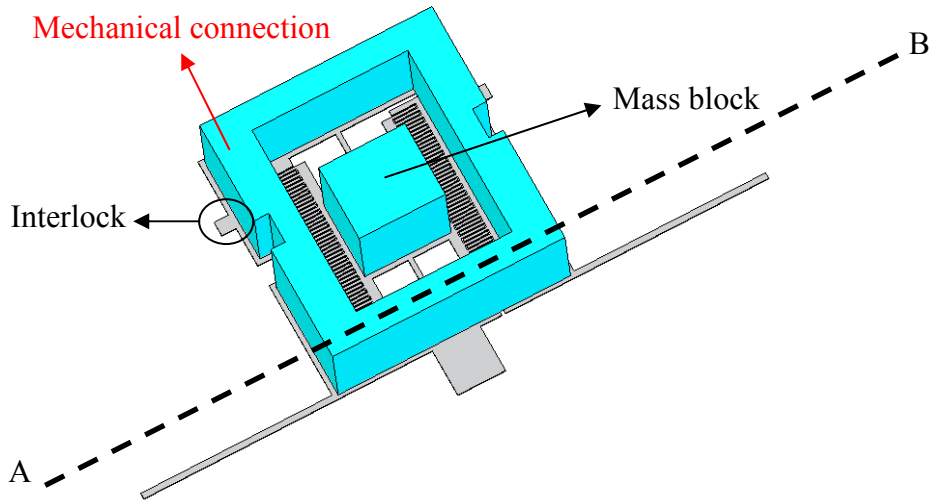


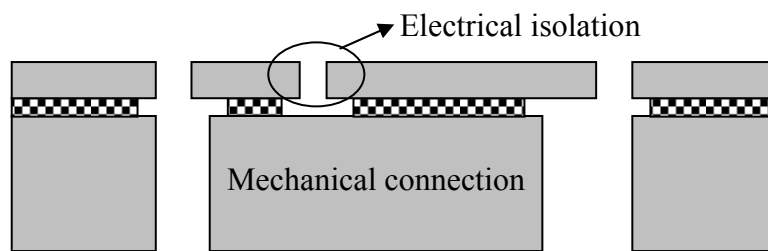
Figure 2-1 (a) 3D model of the proposed scanning mirror, (b) vertical comb fingers.



(a)



(b)



(c)

Figure 2-2. Illustrations of electrical isolation and mechanical connection, (a) front side view, (b) back side view and (c) cross-section view along A-B.

2-2 Push assembly process

Figure 2-3 shows the assembly process by the simple push operation [5]. The mirror plate and the support are in the device layer of the SOI wafer. The substrate underneath the push pad needs to be etched by ICP DRIE to provide space for the push operation. The assembly processes need two microprobes and two push operations. First, Probe 1 pushes the support to about 60° and holds in position (Figure 2-3 (b)). Then Probe 2 pushes the mirror to about 45° and holds in position (Figure 2-3 (c)). Then Probe 1 is removed and the restoring forces of the torsional beams make the support lie on the mirror (Figure 2-3 (d)). Finally Probe 2 is removed and the mirror and the support are interlocked by the lock mechanism (Figure 2-3 (e)). The large area of the push pad provides large probe positioning tolerance that can reduce the assembly time.



Torsional beam

The torsional beams provide the restoring force to interlock the mirror in position. The torsional beam must be long enough or it would break during pushing. However, extending the length of the torsional beams reduces the fill factor. Therefore, an appropriate length of the torsional beam needs to be chosen. In addition, the restoring forces of the mirror plate and the support may cause lateral displacement of the torsional beams. Therefore a mechanical stop mechanism was designed on both sides of the torsional beam in the same SOI device layer to prevent the lateral displacement which would cause angular error, as shown in Figure 2-3 (f).

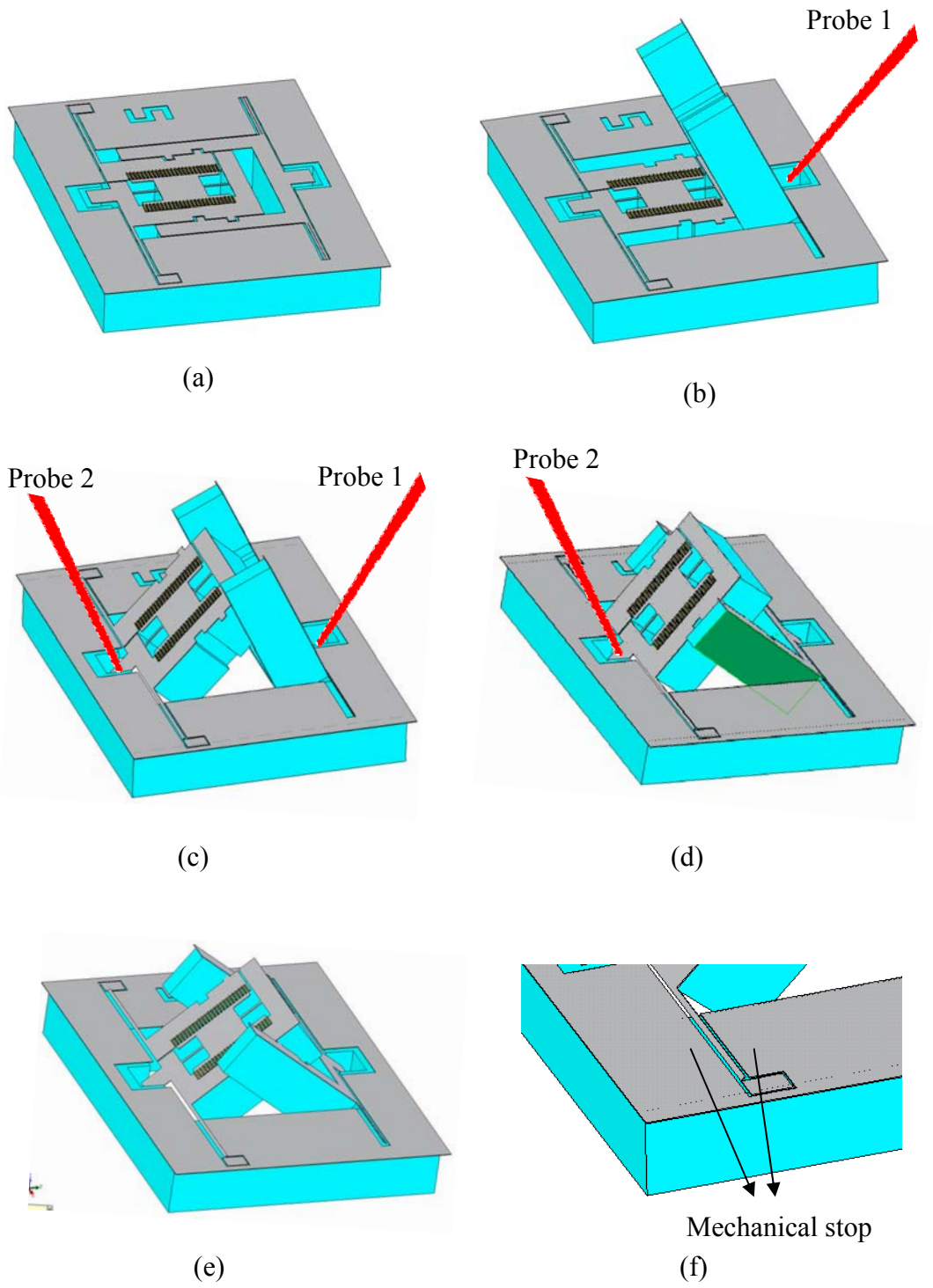


Figure 2-3. Assembly processes of the flip-up micro scanning mirror.

For a 45° mirror plate, the maximum twist angle is approximate 80° during the assembly process. The length of the torsional beams can be found from the torsional formula of a beam with a rectangular cross section as follows [34],

$$\theta_a = \frac{TL}{KG}, \quad (2-1)$$

$$K = ab^3 \left[\frac{16}{3} - 3.36 \frac{b}{a} \left(1 - \frac{b^4}{12a^4} \right) \right], \text{ for } a > b, \quad (2-2)$$

$$\sigma_{\max} = \frac{3T}{8ab^2} \left[1 + 0.6095 \frac{b}{a} + 0.8865 \left(\frac{b}{a} \right)^2 - 1.8023 \left(\frac{b}{a} \right)^3 + 0.9100 \left(\frac{b}{a} \right)^4 \right], \text{ for } a \geq b, \quad (2-3)$$

where θ_a is the angle of twist in radius, T is the applied torque, L is the torsional beam length, K is the cross-section shape-dependant factor, G is the shear modulus of the material, σ_{\max} is the maximum shear stress in the beam with the applied torque, a is the half of the longer side of the cross section and b is the shorter side of the torsional beam (figure 2-4).

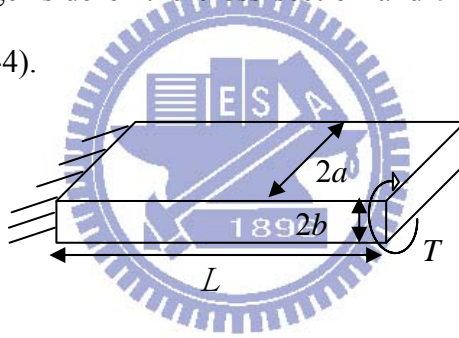


Figure 2-4. Dimensions of the torsional beam

The thickness of the device layer of the SOI wafer is 5 μm therefore b is 2.5 μm . The width of the torsional beam is 25 μm therefore a is 12.5 μm . The shear modulus of the single-crystal silicon is 79.9 GPa [35]. The yield stress is 7 GPa at room temperature [36] but the yield stress of the manufactured silicon would be lower to 2 GPa. The maximum shear stress must be lower than the yield strength, therefore $\sigma_{\max} = 0.7$ GPa is used for a safety factor of 3. By substituting the values into Equations 2-2 and 2-3, we can get K and T as $9.1 \times 10^{-22} \text{ m}^4$ and $1.27 \times 10^{-7} \text{ N} \cdot \text{m}$, respectively. The length of the torsional beam can be found to be approximately 800 μm from Equation 2-1.

2-3 Static analysis

As Figure 2-2 (a) shows, the mirror plate is connected to the frame by torsional springs. A DC bias is applied to the fixed comb electrodes to provide an electrical torque (τ_e) to rotate the mirror around the torsional springs. The mechanical restoring torque (τ_m) from the torsional springs is induced during rotation and is directly proportional to the rotation angle (θ_{scan}). The maximum rotational angle is proportional to the vertical finger offset (T_{SU8}) but is inversely proportional to the finger length (L_f). The cross section profile of the finger is shown in Figure 2-5. L_f is the length from rotation axis to the tip of the moving comb finger, and L_{f0} is the length from rotation axis to the tip of the fixed comb finger.

When a voltage is applied, the mechanical restoring torque increases as the rotation angle increases. The rotation angle can be calculated when the mechanical restoring torque equals to the electrical torque. The electrical torque can be approximated as [17]:

$$\tau_e = \frac{1}{2} \frac{\partial C_t}{\partial \theta_{scan}} V^2 = \frac{1}{2} \varepsilon_0 N_f \frac{(L_f^2 - L_{f0}^2)}{g} V^2, \quad (2-4)$$

where C_t , V , ε_0 , N_f and g are the total capacitance of the comb fingers, applied DC bias voltage, permittivity of air, number of fingers and lateral finger gap, respectively.

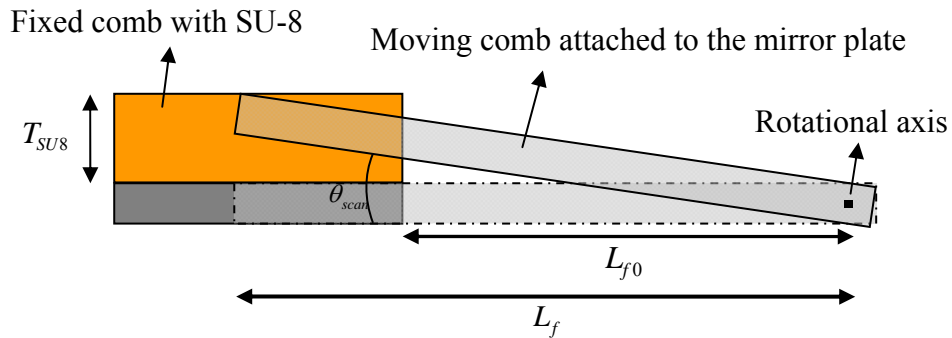


Figure 2-5. Cross section profile of the finger.

The mechanical restoring torque can be expressed as [37]:

$$\tau_m = 2k_s \cdot \theta_{scan} \cong \frac{2Gwt^3}{3l} \left(1 - \frac{192}{\pi^5} \frac{t}{w} \tanh\left(\frac{\pi w}{2t}\right)\right) \cdot \theta_{scan}, \text{ for } w > t \quad (2-5)$$

where k_s is the torsional spring constant, G is the shear modulus, l is the length of the torsional spring, w and t are the cross-section geometry with $w > t$. Note that $2k_s$ is due to the parallel connection of the two torsional springs on both sides of the mirror. The rotation angle can be obtained by solving $\tau_e = \tau_m$ as,

$$\theta_{scan} = \frac{1}{2} \varepsilon_0 N_f \frac{(L_f^2 - L_{f0}^2)}{2k_s g} V^2. \quad (2-6)$$

As the rotation angle approaches the maximum angle, Equation 2-6 can not depict the rotation angle precisely. Because the electrical torque decreases as the rotation angle increases. The rotation angle is saturated at a maximum angle. Dimensions of the micro scanning mirror are described in Table 2-1.

CoventorWare MEMS design software was applied to calculate the rotational angle versus the applied voltage as shown in Figure 2-6. It can be found that the saturation angle is about 0.5° .

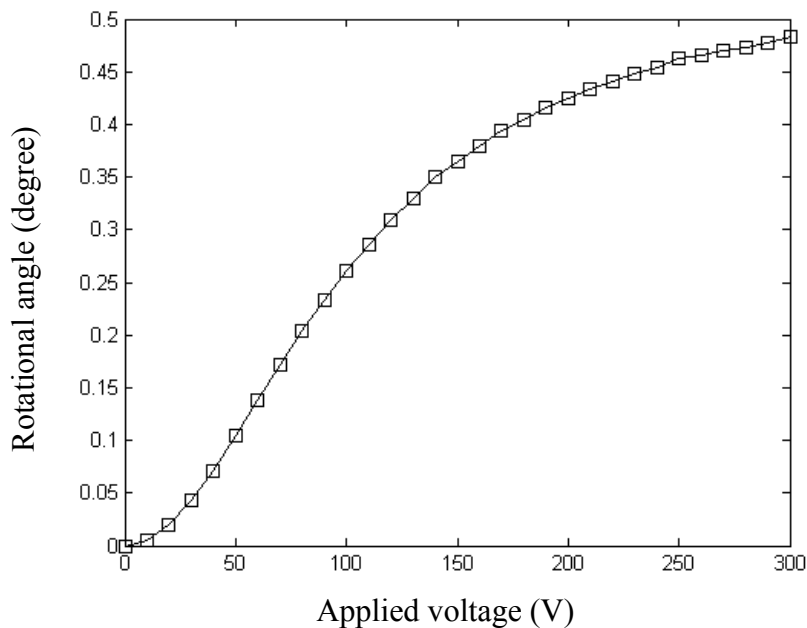


Figure 2-6. Simulated rotation angle versus applied voltage

Table 2-1. Dimensions of the micro scanning mirror.

Description	Symbol	Value (μm)
Mirror size	-	400×360
Number of fingers	N_f	24
Vertical finger offset	T_{SU8}	10
Finger gap	g	7
Finger length	-	100
Finger width of the moving comb (silicon)	-	10
Finger width of the fixed comb (SU-8)	-	6
Torsional spring width	w	20
Torsional spring thickness	t	5
Torsional spring length	l	220
Length from rotation axis to the tip of the fixed comb finger	L_{f0}	205
Length from rotation axis to the tip of the moving comb finger	L_f	300

2-4 Dynamic analysis

The resonant frequency of a rotational system can be calculated as follow:

$$f_R = \frac{1}{2\pi} \sqrt{\frac{2k_s}{I_m}}, \quad (2-7)$$

$$I_m = \rho t_m w_m l_m \left(\frac{w_m^2}{12} + \frac{t_m^2}{3} \right), \quad (2-8)$$

where I_m is the total mass moment of inertia, ρ is the density of mass; t_m , l_m and w_m are the dimensions of the rotational mirrors as shown in Figure 2-7. Note that $2k_s$ represents the parallel connection of torsional springs. The calculation of I_m is shown below. The thin nitride and oxide layers are ignored during the calculation.

$$\begin{aligned} I_m &= \rho \int_V R^2 dV \\ &= \rho \int_{-w_m/2}^{w_m/2} \int_0^{l_m} (w_m^2 + t_m^2) l_m dt_m dw_m \\ &= \rho t_m w_m l_m \left(\frac{w_m^2}{12} + \frac{t_m^2}{3} \right) \end{aligned} \quad (2-9)$$

By substituting the values in Table 2-1 into Equations 2-7 and 2-8, the resonant frequency is about 1362 Hz.

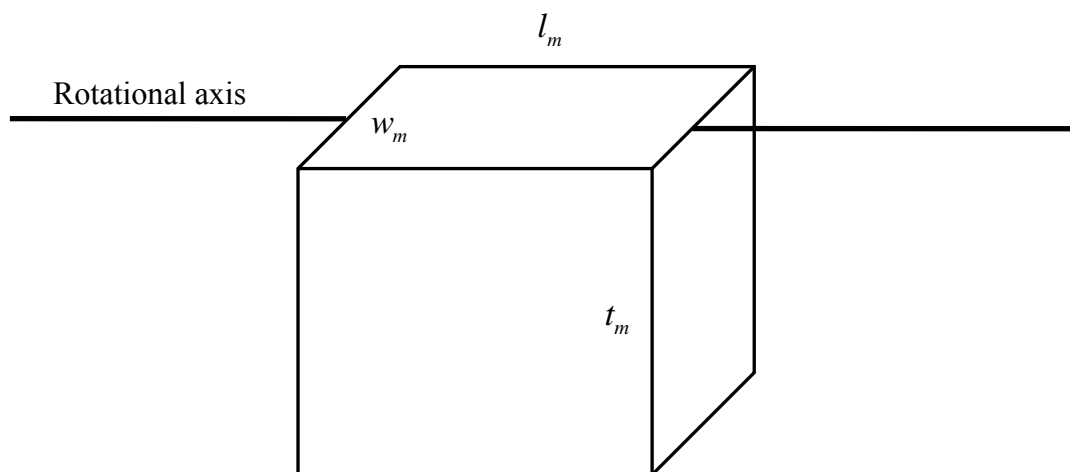


Figure 2-7. Illustration of the mirror dimensions

Figure 2-8 shows the solid model of the beam type micro scanning mirror for modal analysis by using CoventorWare. The first four resonant modes are summarized in the Table 2-2. Mode 1 is the rotational motion around the y-axis along the torsional spring as shown in Figure 2-9. Mode 2 is the piston motion along the z-axis as shown in Figure 2-10. Mode 3 shows the rotational motion around the x-axis as shown in Figure 2-11. Mode 4 is the rotational motion around a y-axis at the bottom of the substrate as shown in Figure 2-12. The simulated resonant frequency of the first mode is 1380 Hz, which is very close to the theoretical calculation of 1362 Hz.

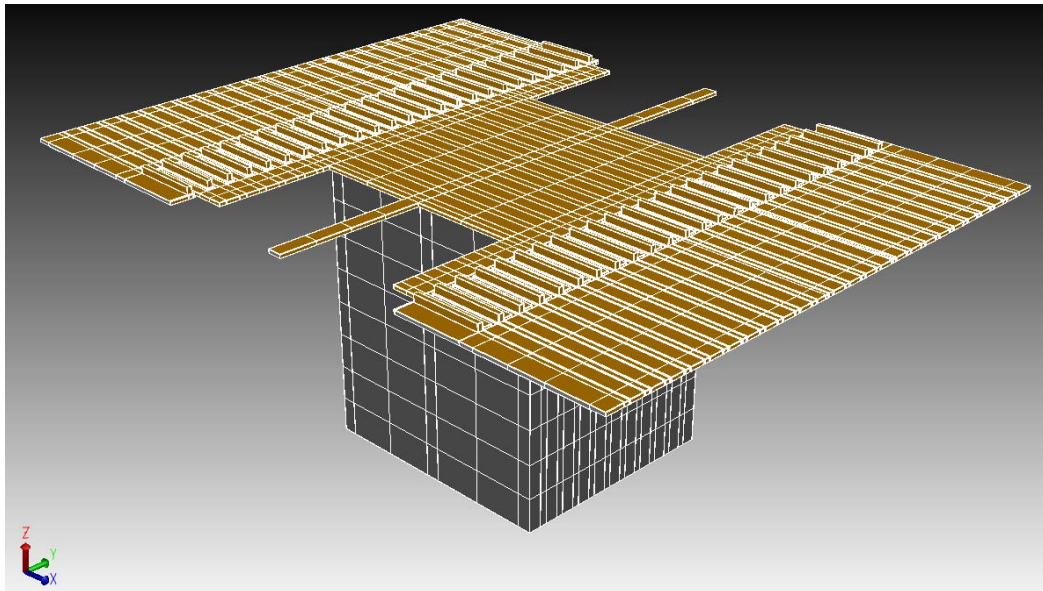
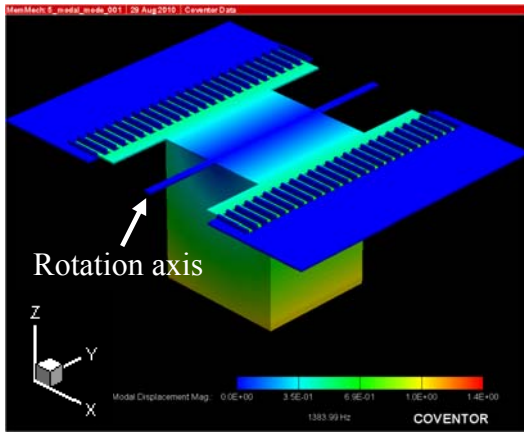


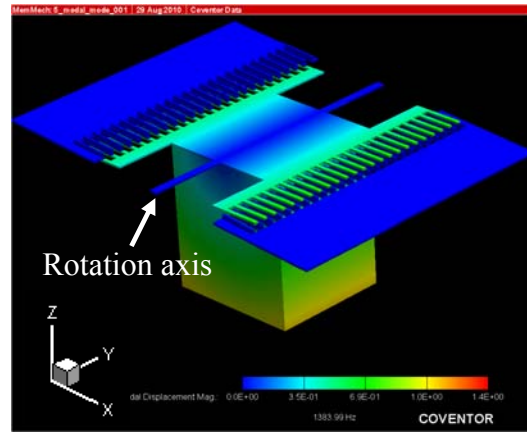
Figure 2-8. Model for modal analysis

Table 2-2. Result of the modal analysis of the beam type micro mirror.

Mode	Frequency	Description
1	1.38KHz	Rotation around y-axis
2	4.65KHz	Piston motion along z-axis
3	5.34KHz	Rotation around x-axis
4	28.44KHz	Rotation around y-axis

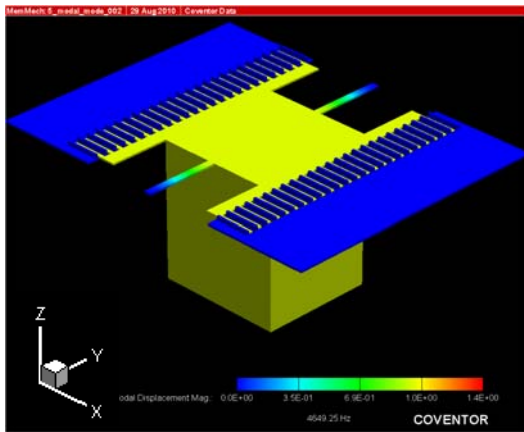


(a)

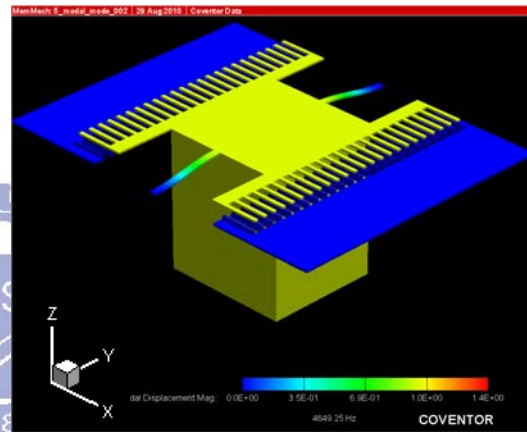


(b)

Figure 2-9. Mode 1 of the beam type mirror: rotation around the spring.

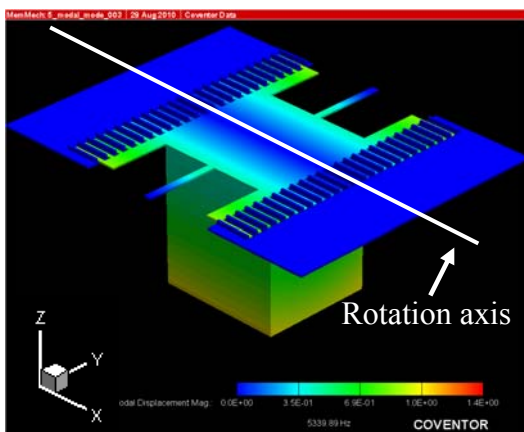


(a)

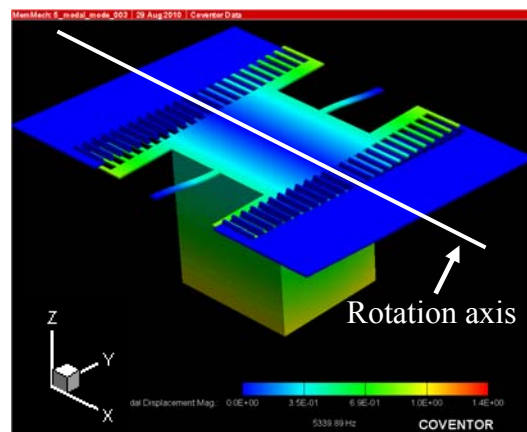


(b)

Figure 2-10. Mode 2 of the beam type mirror: piston motion along z-axis.



(a)



(b)

Figure 2-11. Mode 3 of the beam type mirror: rotation around x-axis.

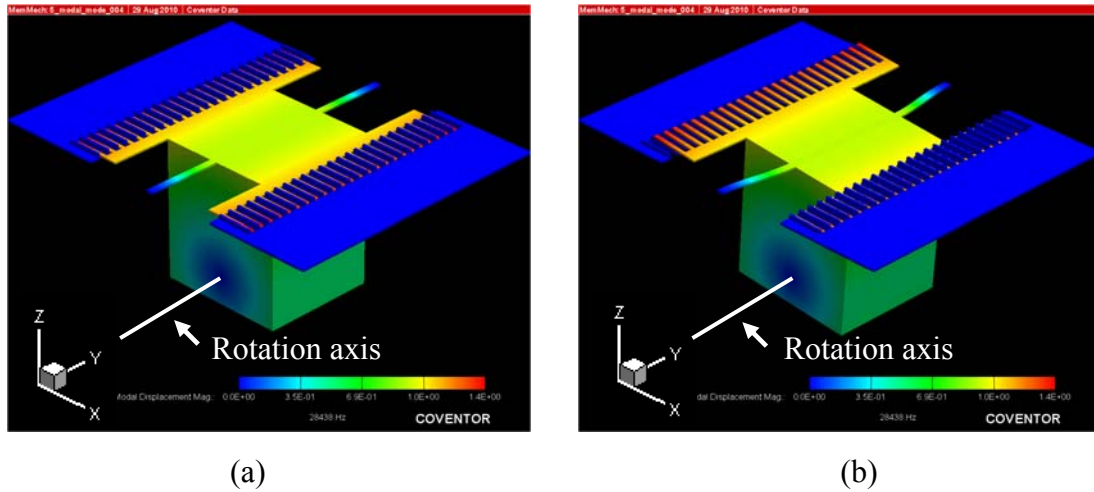
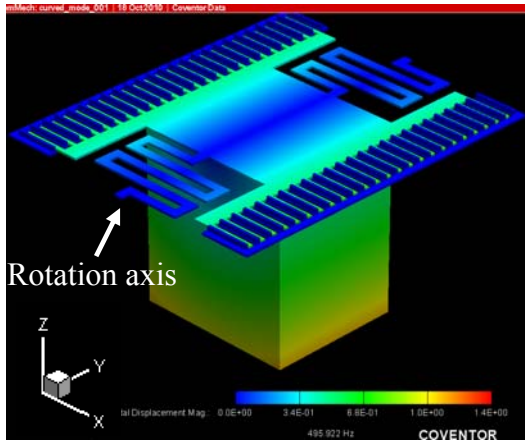


Figure 2-12. Mode 4 of the beam type mirror: rotation around y-axis.

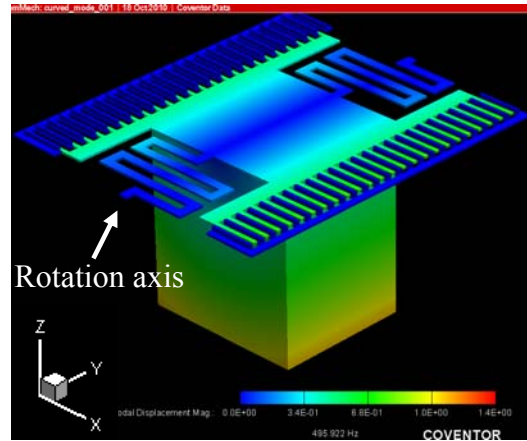
The modal analysis of the meander spring type micro scanning mirror was also simulated by using CoventotWare. Table 2-3 shows the first four resonant modes. Mode 1 is the rotational motion around the y-axis along the torsional spring as shown in Figure 2-13. Mode 2 is the piston motion along the z-axis as shown in Figure 2-14. Mode 3 shows the rotational motion around the x-axis as shown in Figure 2-15. Mode 4 is the rotational motion around a x-axis at the bottom of the substrate as shown in Figure 2-16.

Table 2-3. Result of the modal analysis of the meander type micro mirror.

Mode	Frequency	Description
1	0.496 KHz	Rotation around y-axis
2	1.483 KHz	Piston motion along z-axis
3	1.728 KHz	Rotation around x-axis
4	10.978 KHz	Rotation around x-axis

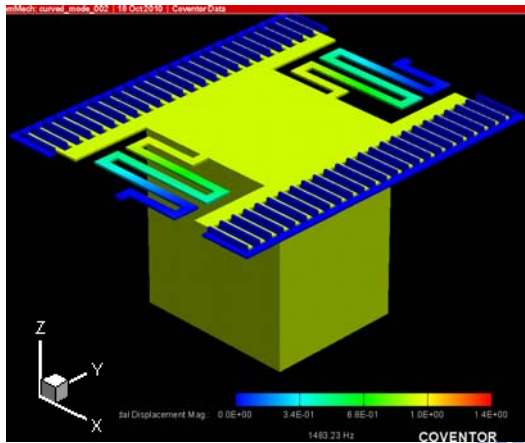


(a)

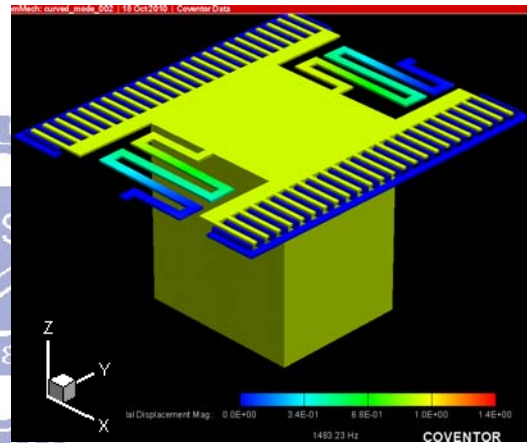


(b)

Figure 2-13. Mode 1 of the meander type mirror: rotation around the spring.

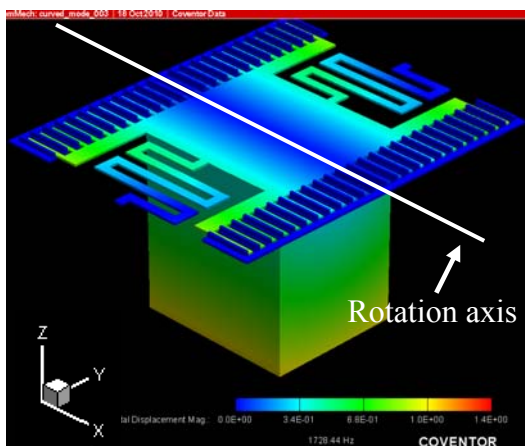


(a)

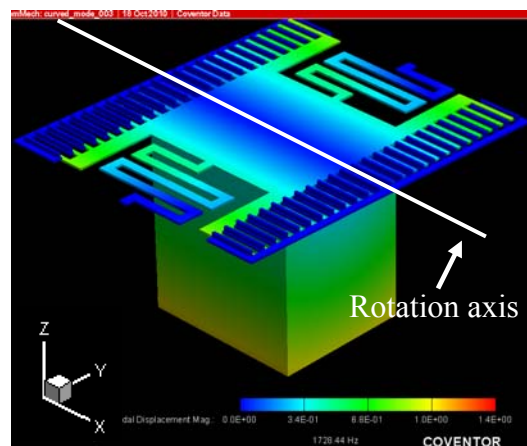


(b)

Figure 2-14. Mode 2 of the meander type mirror: piston motion along z-axis.

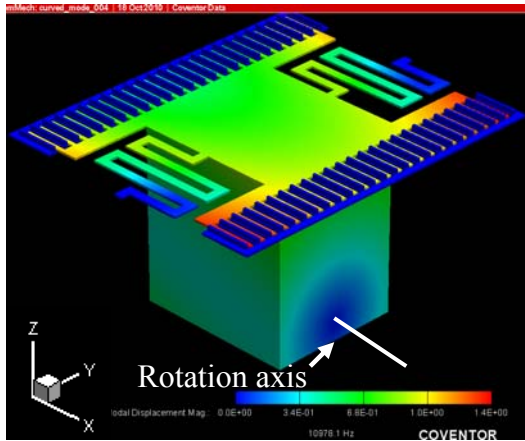


(a)

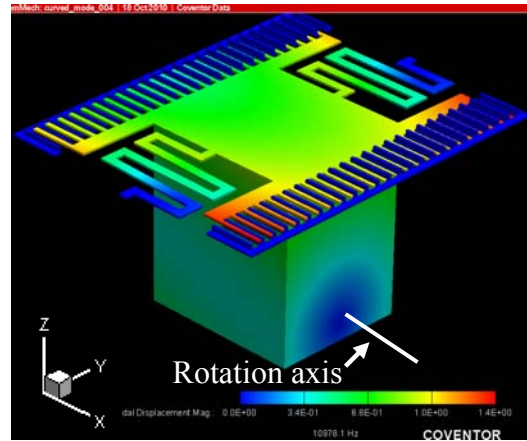


(b)

Figure 2-15. Mode 3 of the meander type mirror: rotation around x-axis.



(a)



(b)

Figure 2-16. Mode 4 of the meander type mirror: rotation around x-axis.



2-5 Torsional spring analysis

Three types of springs as shown in Figure 2-17 are connected to the mirror plate for comparison. The torsional spring constant should be as small as possible to provide larger rotational angle. But the imperfection of the fabrication process such as lithography misalignment would cause side instability and lead to pull-in effect. The pull-in effect occurs when the applied electrostatic lateral force overcomes the spring restoring force. For this reason, the lateral spring constant is an important parameter. The lateral and torsional spring constants of the three type springs were simulated and compared by CoventorWare MEMS design software. The dimensions of the three types of springs are shown in Figure 2-18.

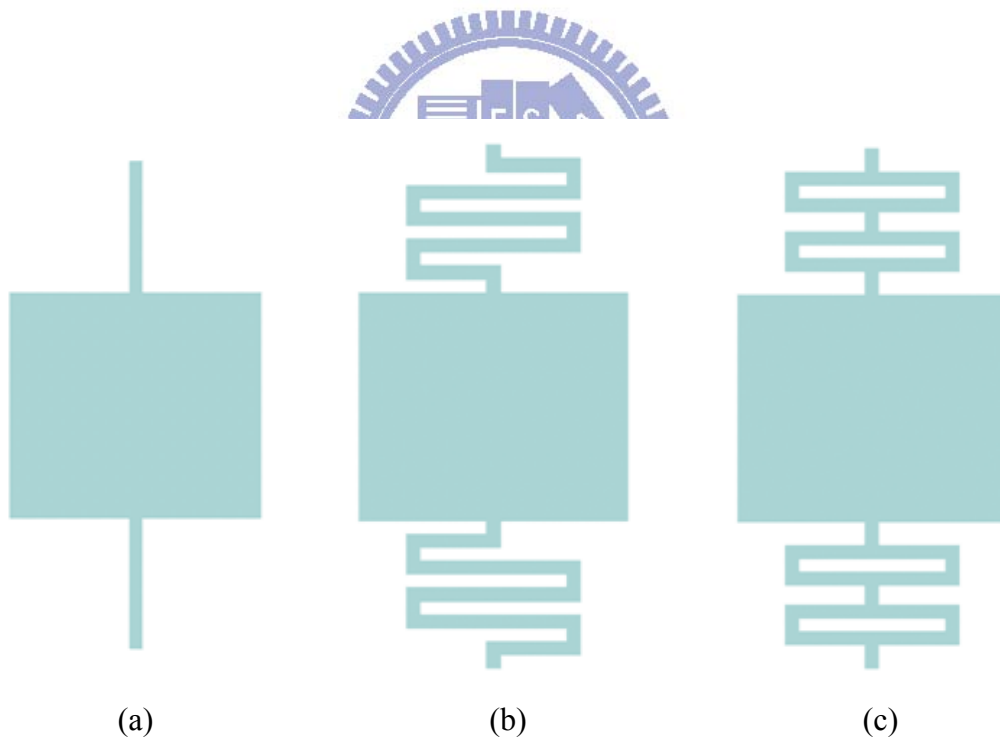


Figure 2-17. Three types of the springs, (a) beam type, (b) meander type and (c) box type.

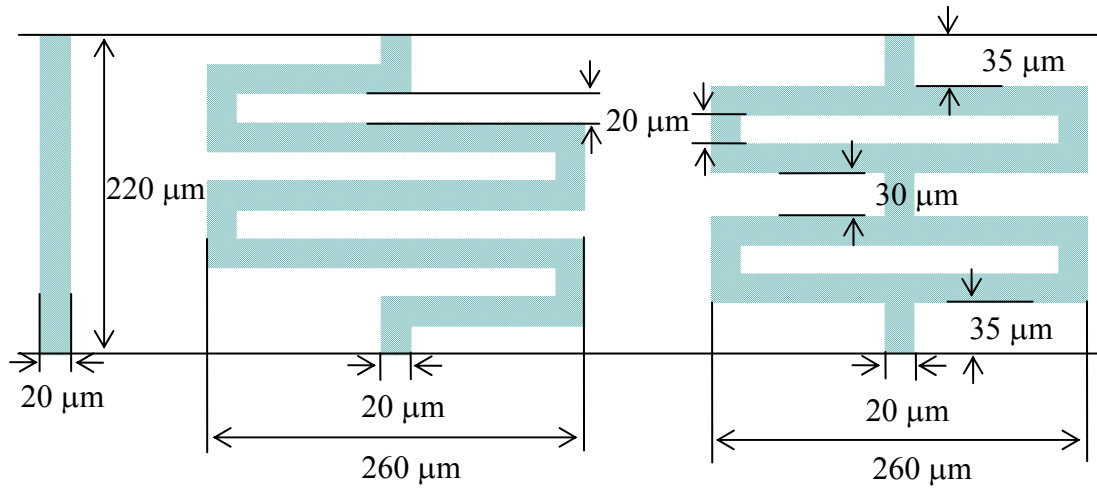
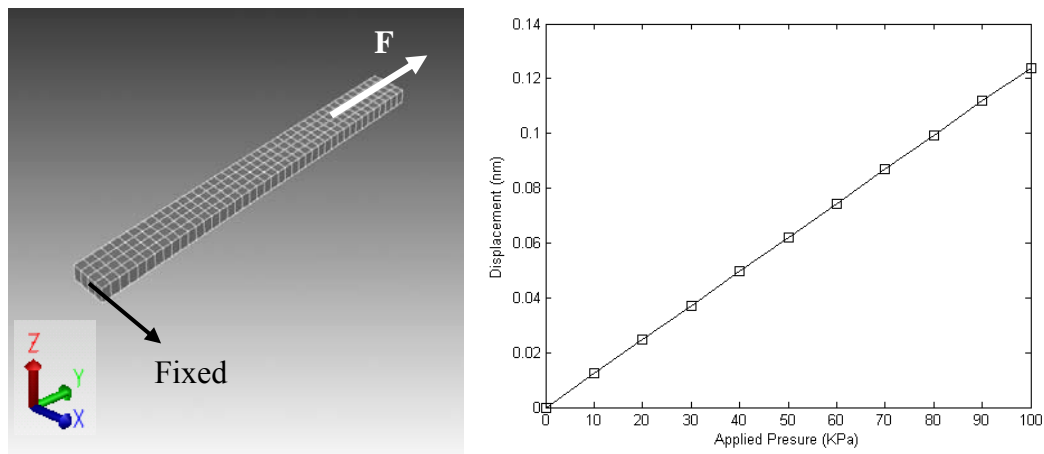


Figure 2-18. Dimensions of the springs

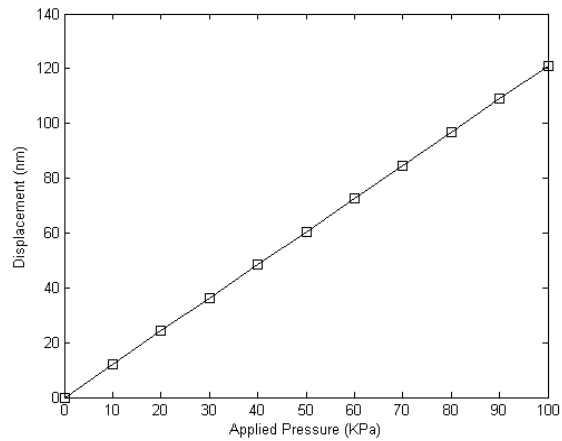
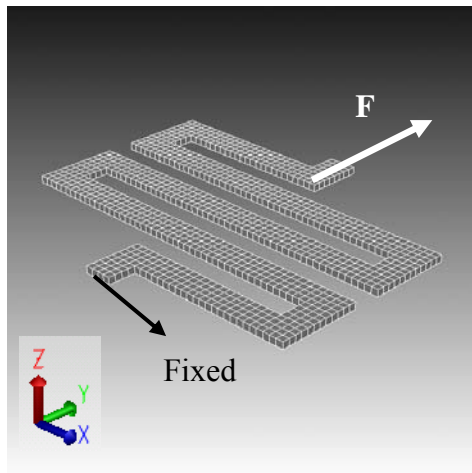
2-5-1 Lateral spring constant k

The spring was fixed in one side and a y-direction pressure was applied on the other side ($20 \mu\text{m} \times 5 \mu\text{m}$) as shown in Figure 2-19. The simulated displacements versus applied pressure for three types of springs are plotted in Figure 2-19. From the simulation, the calculated spring constants are 8.06×10^4 (N/m), 8.26×10 (N/m) and 1.52×10^3 (N/m) respectively.

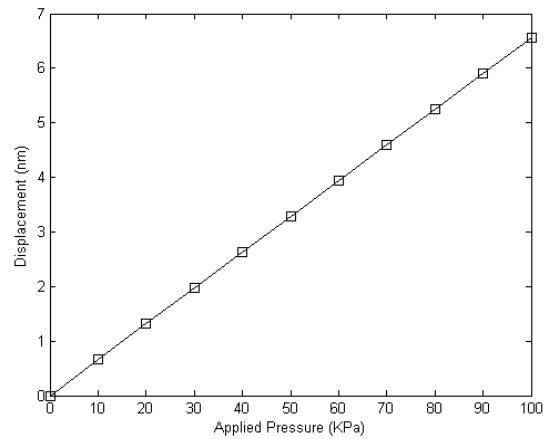
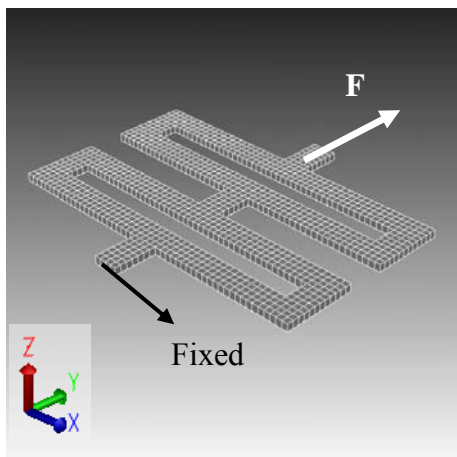


(a) beam type

Figure 2-19. Displacement versus applied pressure of three types of springs.



(b) meander type

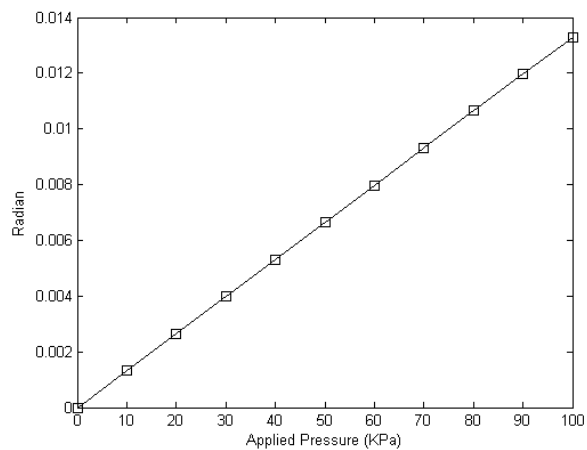
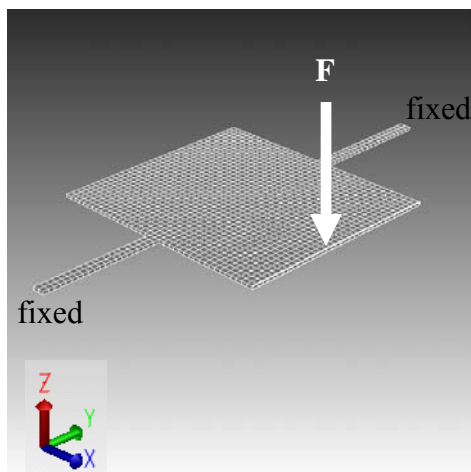


(c) box type

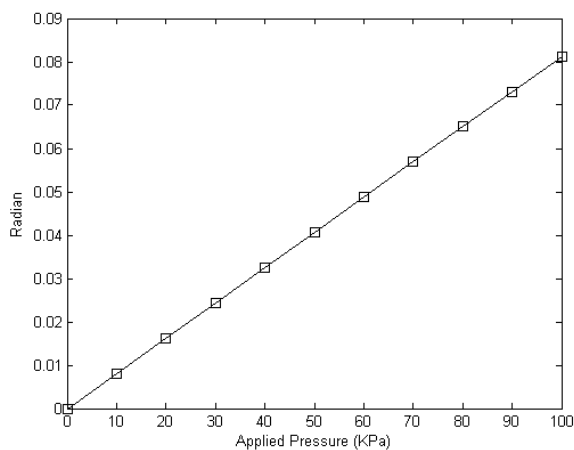
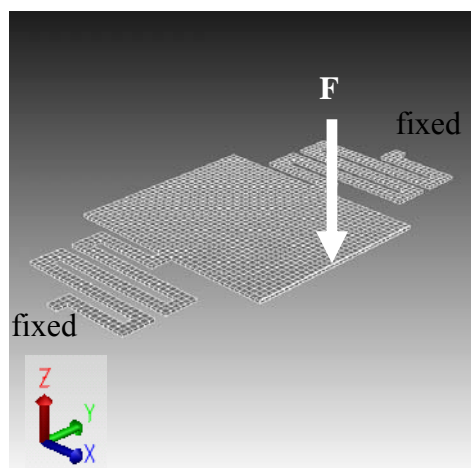
Figure 2-19. Displacement versus applied pressure of three types of springs (continued).

2-5-2 Torsional spring constant k_s

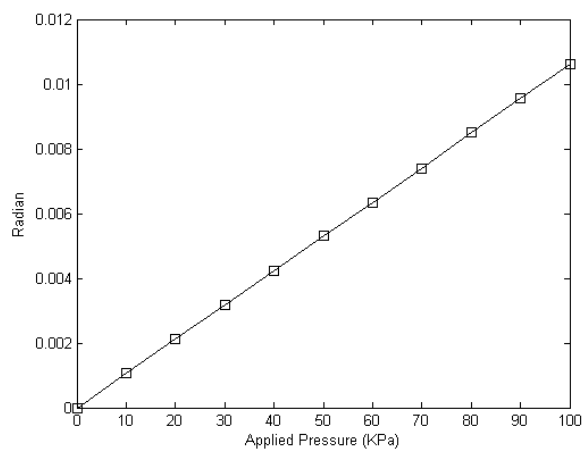
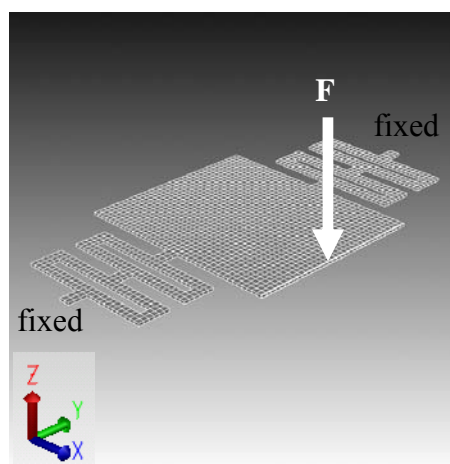
This simulation of torsional spring constants contained two springs and a mirror plate. Both sides of the springs were fixed, and the pressure was applied on the edge of the mirror plate as shown in Figure 2-20. The simulated rotation angle versus the applied pressure results are shown in Figure 2-20. The calculated torsional spring constants from the simulation are 6.1×10^{-7} (N·m/rad), 9.7×10^{-8} (N·m/rad) and 8.0×10^{-7} (N·m/rad) respectively.



(a) beam type



(b) meander type.



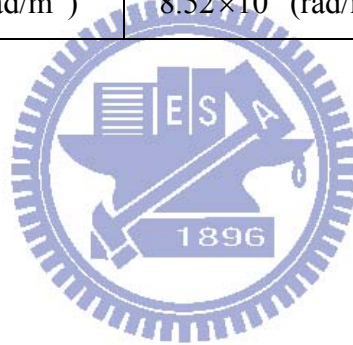
(c) box type

Figure 2-20. Rotation angle versus applied pressure of three types of springs.

To summarize, the parameter Z which represents the ratio of lateral spring constant and torsional spring constant is presented in Table 2-4. The Z parameter can determine the best solution for the spring design of the vertical comb-drive scanning mirror. Larger Z implies that the mirror can rotate more easily and without lateral displacement. The best spring design is the beam type.

Table 2-4. Summary of spring simulation.

Parameter	(I) beam type	(II) meander type	(III) box type
k	8.06×10^4 (N/m)	8.26×10 (N/m)	1.52×10^3 (N/m)
k_s	6.06×10^{-7} (N·m/rad)	9.70×10^{-8} (N·m/rad)	8.03×10^{-7} (N·m/rad)
Z	1.33×10^{11} (rad/m ²)	8.52×10^8 (rad/m ²)	1.90×10^9 (rad/m ²)



2-6 Summary

From the static, dynamic and spring analyses, a flip-up micro scanning mirror is designed. The layout is shown in Figure 2-21. In Chapter 3, the fabrication is discussed.

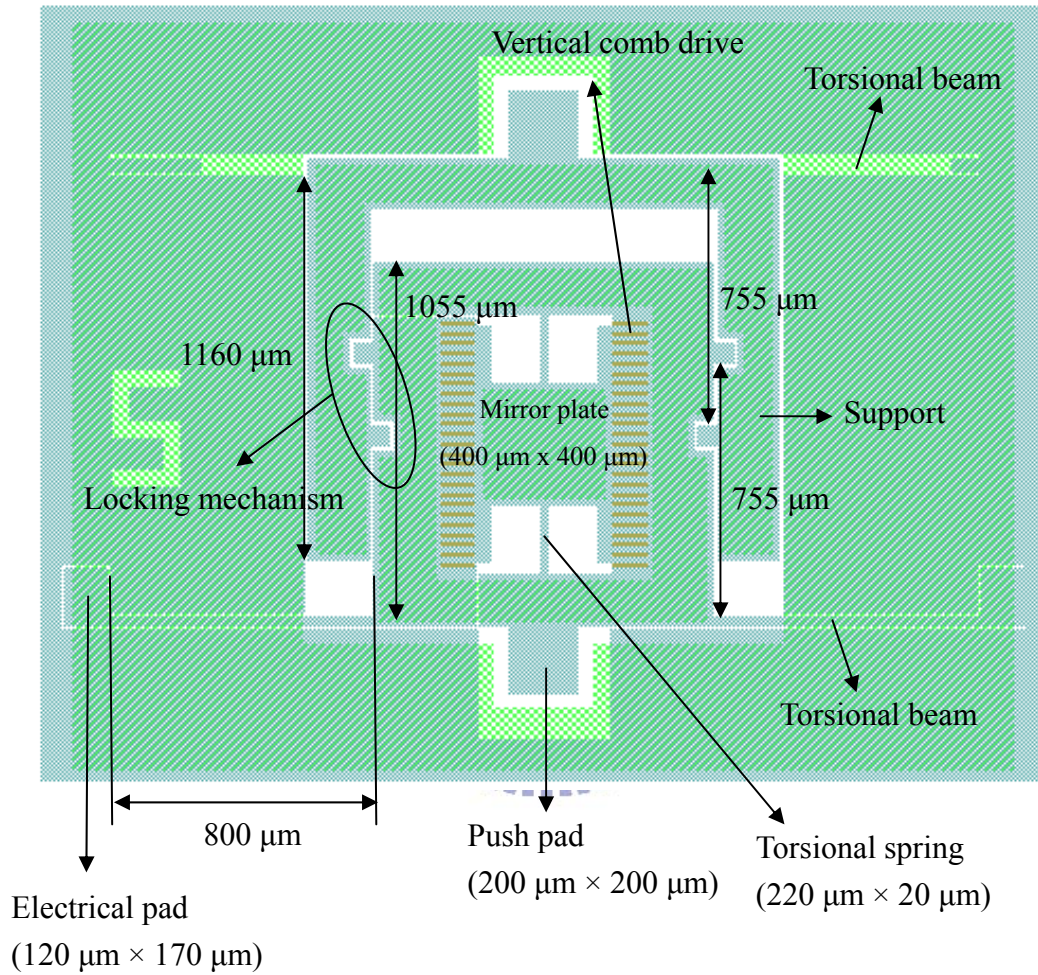


Figure 2-21. Layout of the flip-up micro scanning mirror.

Chapter 3

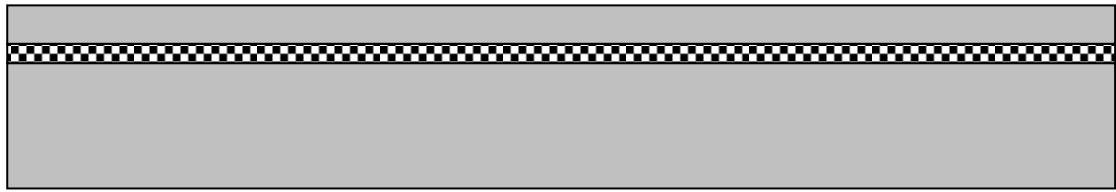
Fabrication Process

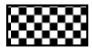

3-1 Introduction

In this chapter, the detailed fabrication processes of flip-up micro scanning mirrors are depicted. The mirrors are fabricated on the SOI wafers due to its flatness. Using SOI wafers can also reduce the complexity of the process. There are only three masks in the process. One is for patterning the front side device layer, one is for the back side handle layer of the substrate and the other is for upper comb fingers made by SU-8 photoresist. The SU-8 photoresist provides not only good mechanical properties for the structure, but also relatively simple fabrication processes. The handle layer of the SOI wafers is used for mechanical connection as depicted in Chapter 2, as well as for enhancing the strength of the structure to avoid bending and improve the mirror flatness. The buried oxide is the sacrificial layer. The nitride layer deposited on the device layer is the hard mask for the DRIE process. Gold is deposited for electrical connection and good reflectivity. The detailed fabrication processes are described in the following. Finally, fabrication issues are discussed.

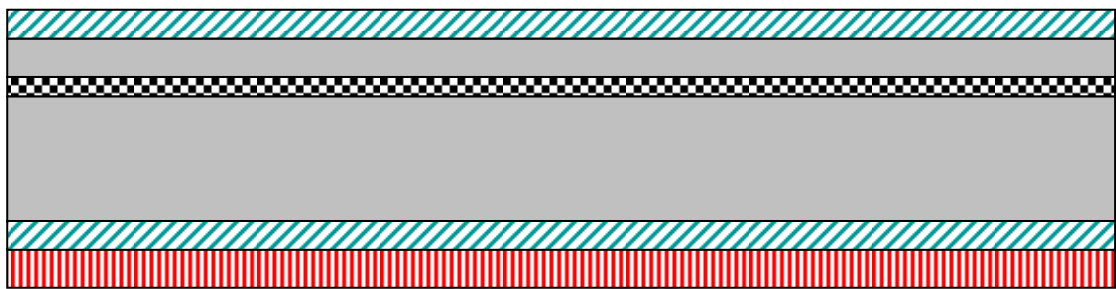
3-2 Fabrication flow

Figure 3-1 shows the schematic of the fabrication flow. The device layer of the SOI wafer is 5 μm thick, the buried oxide layer is 2 μm thick and the substrate is 400 μm thick. The device is fabricated at the Nano Facility Center of National Chiao Tung University and the National Tsing Hua University Center for Nanotechnology, Materials Science, and Micro Systems.



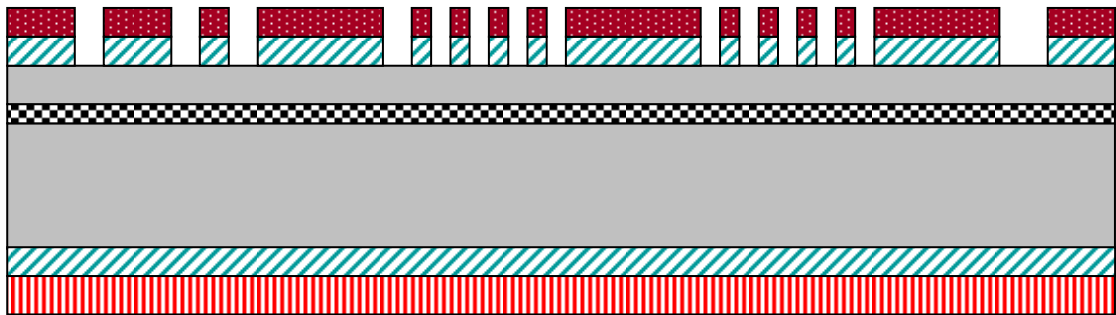
 Buried oxide  Silicon

(a) RCA cleaned SOI wafer (step A)



 Buried oxide  LPCVD nitride  PECVD oxide  Silicon

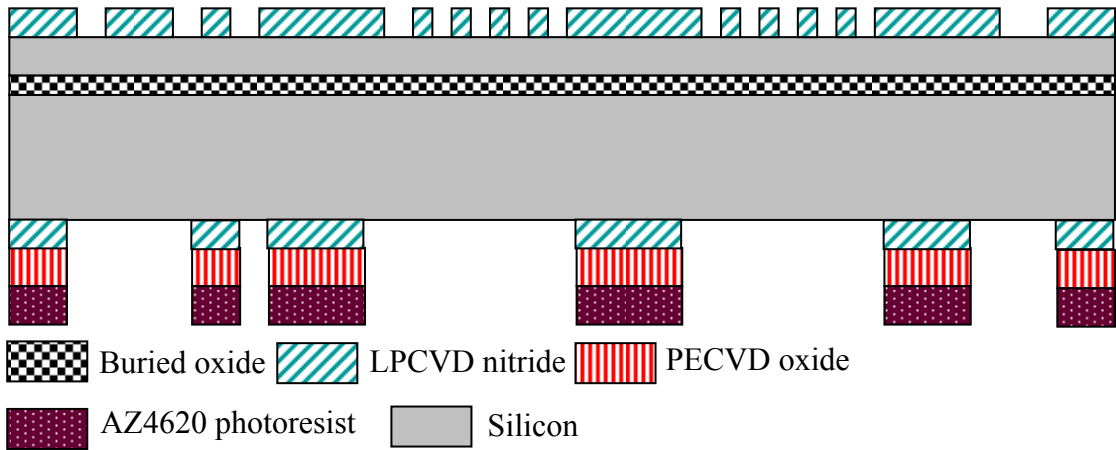
(b) Front side nitride and back side oxide deposition (step B, step C)



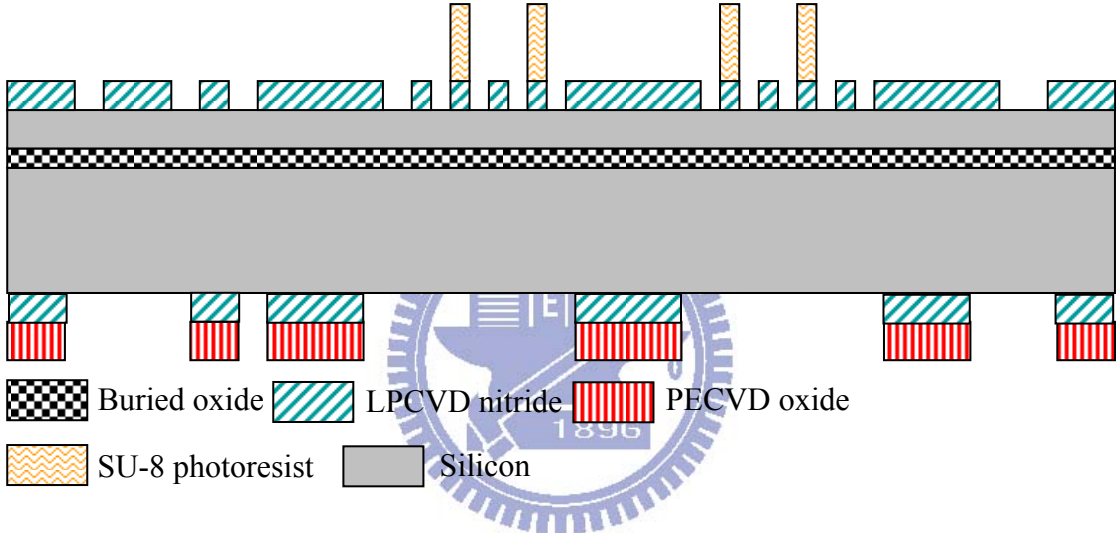
 Buried oxide  LPCVD nitride  PECVD oxide
 FH 6400 photoresist  Silicon

(c) Front side nitride patterning (step D, step E)

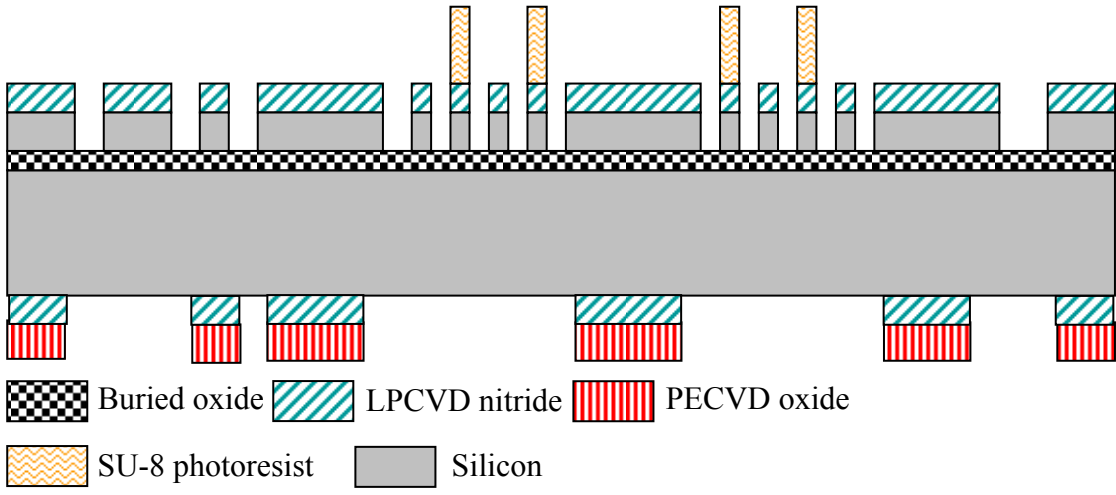
Figure 3-1. Fabrication flow



(d) Back side oxide patterning (step F, step G, step H, step I)

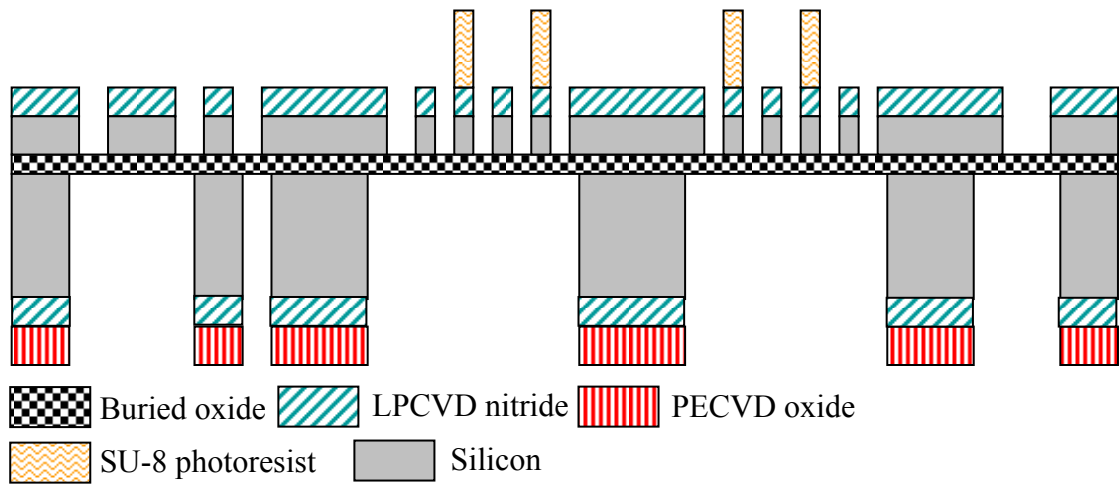


(e) SU-8 photoresist patterning (step J)

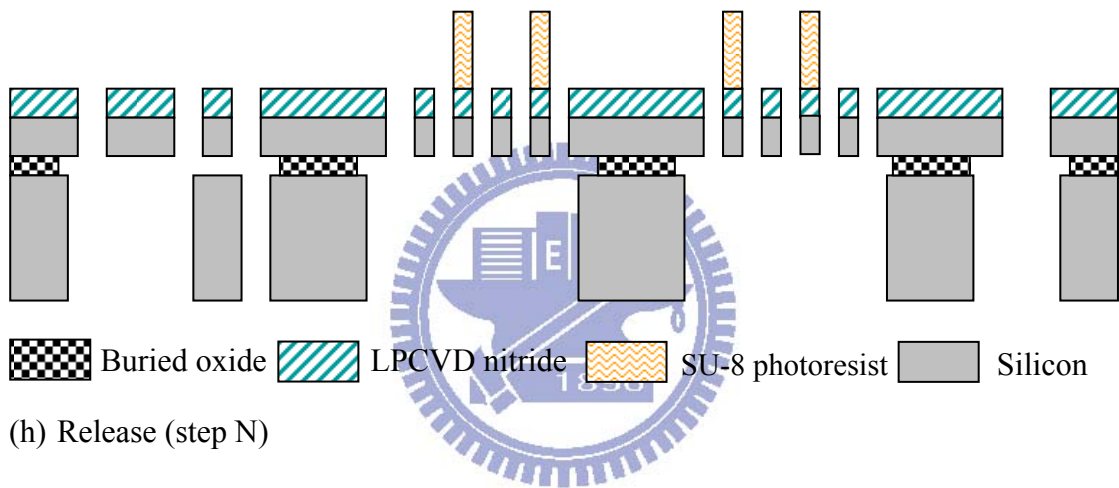


(f) Front side ICP (step K)

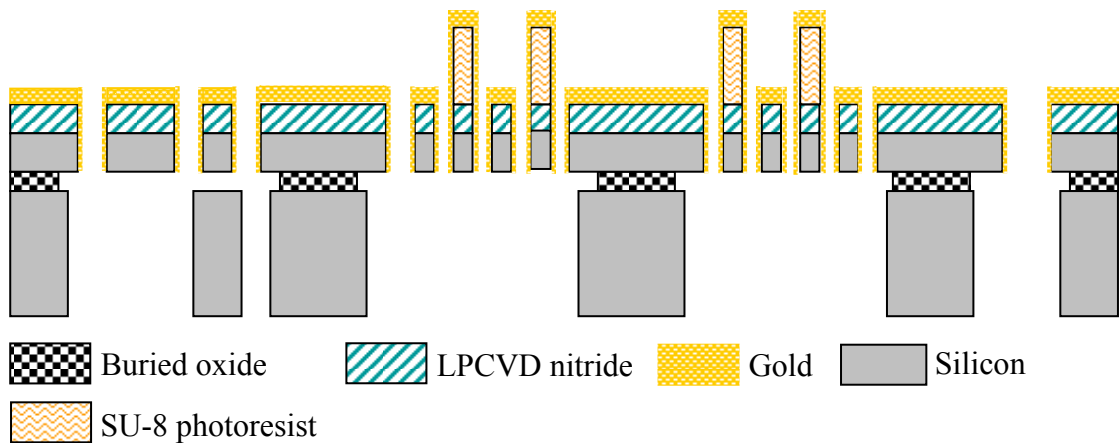
Figure 3-1. Fabrication flow (continued)



(g) Back side ICP (step M)



(h) Release (step N)



(i) Gold deposition (step O)

Figure 3-1. Fabrication flow (continued)

Step A: RCA clean

The SOI wafer was cleaned by the standard RCA clean process before the fabrication steps. The standard RCA clean can remove organic contaminants, native oxide layer, and ionic contamination on the surface. To clean wafer completely can increase the yield rate. Note that the native oxide removal must be reduced to 30 seconds because HF etched buried oxide of the SOI wafer as well. Detailed parameters are listed below.

Step	Parameters
0	D. I. water Rinse (5 min)
1	$\text{H}_2\text{SO}_4 : \text{H}_2\text{O}_2 = 3 : 1$ (10~15 min, 75 °C ~85 °C)
2	$\text{HF} : \text{H}_2\text{O} = 1 : 100$ (30 sec, room temperature)
3	$\text{NH}_4\text{OH} : \text{H}_2\text{O}_2 : \text{H}_2\text{O} = 1 : 4 : 20$ (10~15 min, 75 °C ~85 °C)
4	$\text{HCL} : \text{H}_2\text{O}_2 : \text{H}_2\text{O} = 1 : 1 : 6$ (10~15 min 75 °C ~85 °C)
5	$\text{HF} : \text{H}_2\text{O} = 1 : 100$ (30 sec, room temperature)

Step B: Front side nitride deposition

A 5000 Å thick low pressure chemical vapor deposition (LPCVD) nitride is deposited on the SOI wafer as the DRIE hard mask. The selectivity between the silicon and the LPCVD nitride in the ICP process is about 1: 70. The detailed parameters are listed below.

Description	Parameters
NH_3 flow rate	17 sccm
SiHCl_2 flow rate	85 sccm
Process pressure	180 mTorr
Process temperature	850 °C
Deposition time	10 minutes deposition for 0.1 μm

Step C: Back side oxide deposition

A 5- μm -thick oxide was deposited on the backside of the SOI wafer by plasma-enhanced chemical vapor deposition (PECVD). The process was done with an Oxford 100 PECVD Cassette System at the National Nano Device Laboratories. The deposited oxide layer was used as the hard mask during the ICP process due to its excellent selectivity. The selectivity between the oxide and the silicon in the ICP process is about 1: 100. The detailed recipes are shown below.

	Step1	Step 2	Step 3	Step 4
Recipe	Pump Down	Temp. Stabilization	N ₂ Flow	SiO ₂ Dep.
Pure SiH ₄ (sccm)	0	0	0	8.5
N ₂ O(sccm)	0	0	0	710
N ₂ (sccm)	0	0	1000	161.5
Pressure (mTorr)	0	0	1000	1000
HF RF power (W)	0	0	0	20
LF RF power (W)	0	0	0	0
Temperature (°C)	300	300	300	300
Time	1 min	5 min	5 min	740 Å/min

Step D: Front side nitride patterning (Mask 1)

Mask 1 defines the device layer pattern in the 5000 Å nitride layer. FH6400 photoresist was used for the mask of nitride etching. The selectivity between silicon nitride and FH6400 photoresist is about 1: 2. So the thickness of the photoresist must be larger than 1 μm . Therefore, 2 μm thick photoresist was coated on the wafer. The photolithography process was performed by Electronic Visions EV620 double side aligner at National Tsing Hua University.

Step	Description	Parameters
0	Photoresist	FH6400
1	HMDS coating	Vapor prime oven
2	Coating (spread cycle)	1000 rpm 10 sec
	Coating (spin cycle)	2000 rpm 35 sec
3	Soft bake	90 °C hotplate 150 second
4	Exposure	EV620 mask aligner (9 mW/cm ²) for 32 sec
5	Development	Developer FHD-5 for 90second
6	Rinse	D.I. water 1 min
7	Hard bake	120 °C hotplate 30 min

Step E: Nitride etching

After photolithography, the nitride layer was etched by SAMCO Poly-Si RIE-10N. After etching, the photoresist must be removed by ultrasonic agitation in acetone. The detailed parameters are listed below.

Description	Parameters
SF ₆ flow rate	30 sccm
CHF ₃ flow rate	10 sccm
Helium backside cooling	about 15 sccm
Process pressure	50 mtorr
RF power	100 W
Etch rate	10 min for 1 μm nitride.

Step F: Back side oxide patterning (Mask 2)

Mask 2 defines the through-wafer holes under the push pads and the mechanical connection of the micro scanning mirror. The pattern is transferred to the back side oxide layer as the hard mask for the back side ICP process. The thick oxide layer needs a thick photoresist to mask during the etching. The selectivity between PECVD oxide and AZ4620 is about 1: 1.8, so a 9 μm thick photoresist is needed. But a 9 μm thick AZ4620 photoresist has shrinkage problems that lead to pattern offset. So a 5

μm thick AZ4620 photoresist was used this step. Therefore, step F and step G must be repeated. The detailed parameters are listed below.

Step	Description	Parameters
0	Photoresist	AZ4620
1	HMDS coating	Vapor prime oven
2	Coating (spread cycle)	500 rpm 10 sec
	Coating (spin cycle)	4000 rpm 40 sec
3	Soft bake	90 °C hotplate 4.5 min
4	Exposure	EV620 mask aligner (9 mW/cm ²) for 13.5 sec
5	Development	Developer for 3 min
6	Rinse	D.I. water 5 min
7	Hard bake	120 °C hotplate 40 min

Step G: Back side oxide etching

The oxide was etched by Poly-Si RIE 10N. The etching depth in this step is 2.5 μm because the thickness of photoresist is not enough. The following is the detailed parameters.

Description	Parameters
SF ₆ flow rate	30 sccm
CHF ₃ flow rate	10 sccm
Helium backside cooling	about 15 sccm
Process pressure	50 mtorr
RF power	100 W
Etch rate	25 min for 2.5 μm oxide.

Step H: Back side oxide patterning (Mask 2)

This step was the same as step F except for the exposure time. The exposure time was extended from 13.5 seconds to 22 seconds because the AZ4620 photoresist filled the etched patterns in step G. The thicker photoresist needs more energy for exposure. Other conditions remained the same.

Step I: Back side oxide etching

This step was the same as step G. After etching, the photoresist was removed in acetone.

Step J: SU-8 photoresist patterning (Mask 3)

The 10- μm -thick negative photoresist SU-8 was used in this step to fabricate the fixed comb fingers. The SU-8 needs precise temperature control for pre-exposure and post-exposure bake. Hard bake is necessary for mechanical strength enhancement. The following is the detailed parameters.

Step	Description	Parameters
0	Photoresist	SU-8 2010
1	HMDS coating	Vapor prime oven
2	Coating (spread cycle)	500 rpm 10 sec
	Coating (spin cycle)	3000 rpm 30 sec
3	Pre-exposure bake	95 °C hotplate 3 min
4	Exposure	EV620 mask aligner (9 mW/cm ²) for 23.5 sec
5	Post-exposure bake	95 °C hotplate 3 min
5	Development	SU-8 Developer for 3 min
6	Rinse	IPA 10 sec
7	Hard bake	200 °C hotplate 30 min

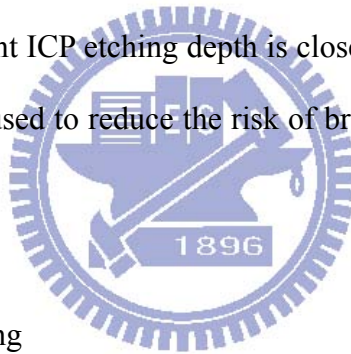
Step K: Front side ICP etching

Inductively-coupled plasma (ICP) RIE was used in this step to etch high-aspect-ratio features in the device layer. The process etched through the 5 μm device layer to the buried oxide layer, which plays the role of etching stop. This step was performed with a STS Multiplex ICP system at Instrument Technology Research Center (ITRC). The following lists the detailed parameters.

Description	Etch phase parameters	Passivation phase parameters
Time per cycle	11.5 seconds	7.0 seconds
SF ₆ flow rate	130 sccm	0 sccm
C ₄ F ₈ flow rate	0 sccm	85 sccm
O ₂ flow rate	13 sccm	0 sccm
Coil RF power	600 W	600 W
Platen RF power	11.5 W	0 W
Process pressure	APC position = 81.2 % Base pressure = 0.3 mtorr	
Helium backside cooling	Helium backside pressure = 10 torr Maximum helium leak up rate = 20 mtorr/min	
Etch rate	0.6-0.7 μm per cycle depending on pattern	

Step L: Wafer dicing

After the front side etching, the wafer was diced into approximate by 1cm × 1cm chips. Because the subsequent ICP etching depth is close to the entire thickness of the wafer, only diced chips are used to reduce the risk of breaking the whole wafer in the ICP chamber.



Step M: Back side ICP etching

In this step, the 400-μm-thick handle layer of the SOI wafer is etched by ICP. The ICP system provides high aspect ratio and vertical sidewall features. Thermal release tape was used to bond the diced chip on the carrier wafer which has a 5-μm-thick oxide on it. This step etched through the 400-μm-thick substrate to the buried oxide which served as the etching stop. The parameters were the same as step K.

Step N: Release.

HF vapor was used to etch the buried oxide in order to release the structure. The experiment was shown in Figure 3-2 [39]. Temperature is critical in this step. The

surface temperature of the chip was controlled by modifying the distance between the lamp and the sample. High temperature can decrease the etching rate and low temperature can cause water condensation and stiction problems. The best distance between the lamp and the sample is about 7 cm for the range of temperature about 35-40 °C.

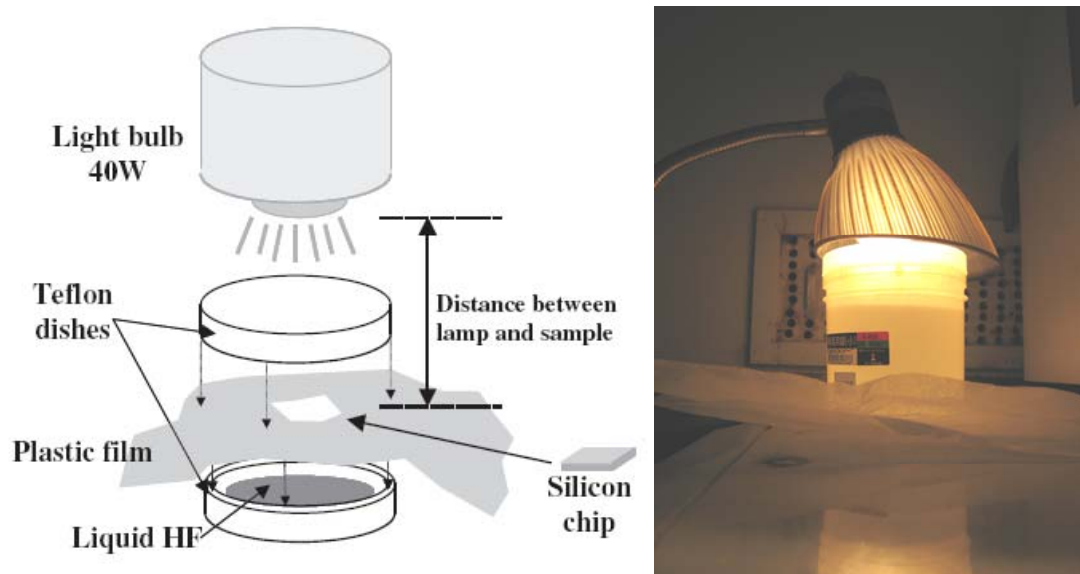


Figure 3-2. Schematic of the HF vapor release setup [39].

Step O: Gold deposition

After releasing the structure, the final step was to deposit gold. The gold layer was used for electrical conduction and improving the reflectivity of the mirror. The gold was deposited on the structure and the sidewall of the comb fingers. The device layer and the substrate are not shorted due to the undercut of the oxide layer in step N. For this reason, the comb fingers are electrical isolated. Figure 3-3 shows the schematic of the gold deposition performed in an ULVAC E-Gun System at CNMM of NTHU. A 500 Å titanium layer was deposited first as the adhesion layer to avoid peeling off of the gold layer. After the Ti deposition, the 5000 Å gold was deposited.

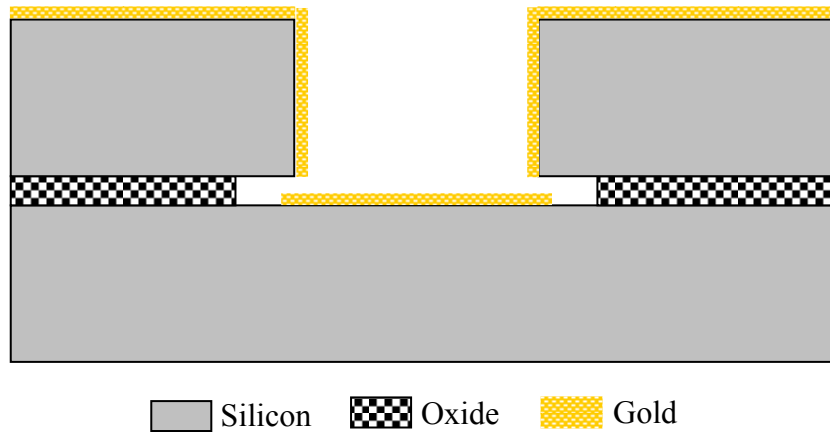


Figure 3-3. Schematic of the gold deposition.

3-3 Fabrication issues

Some problems were encountered during the process flow. It is discussed and the solutions are provided in this section.

3-3-1 SU-8 patterning

SU-8 is a negative photoresist with high viscosity. The adhesion promoter such as HMDS is not required as depicted in the processing guidelines. In general, coating on the silicon substrate without HMDS has good shape geometry and adhesion as shown in Figure 3-4. But in this design, the SU-8 photoresist is coated on nitride. Figure 3-5 shows the SU-8 patterns on the nitride layer under the same photolithography conditions except for the HMDS coating. It was found that the shape geometry and the adhesion were improved with HMDS coating. It was also found that the exposure needed to be modified. The standard exposure dose is for silicon substrates. For other substrates, it has to be modified. The recommended exposure dose for the nitride substrate is increased by 1.5-2.0 times compared to the silicon substrate in the processing guidelines. Figure 3-6 shows the optical micrographs of SU-8 patterns under the same photolithography conditions except for

exposure dose. It can be observed that low exposure dose would cause adhesion problem and high exposure dose would cause bad geometry. According to this experiment, the best exposure dose is about 1.25 times of that for the silicon substrate.

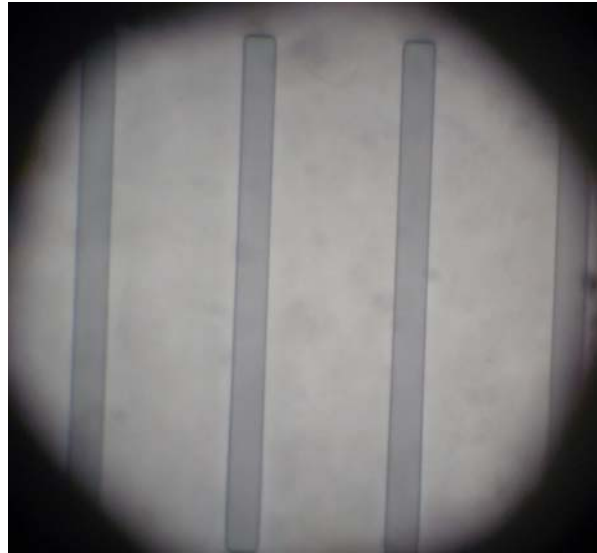


Figure 3-4. Optical micrograph of SU-8 patterned on the silicon substrate.

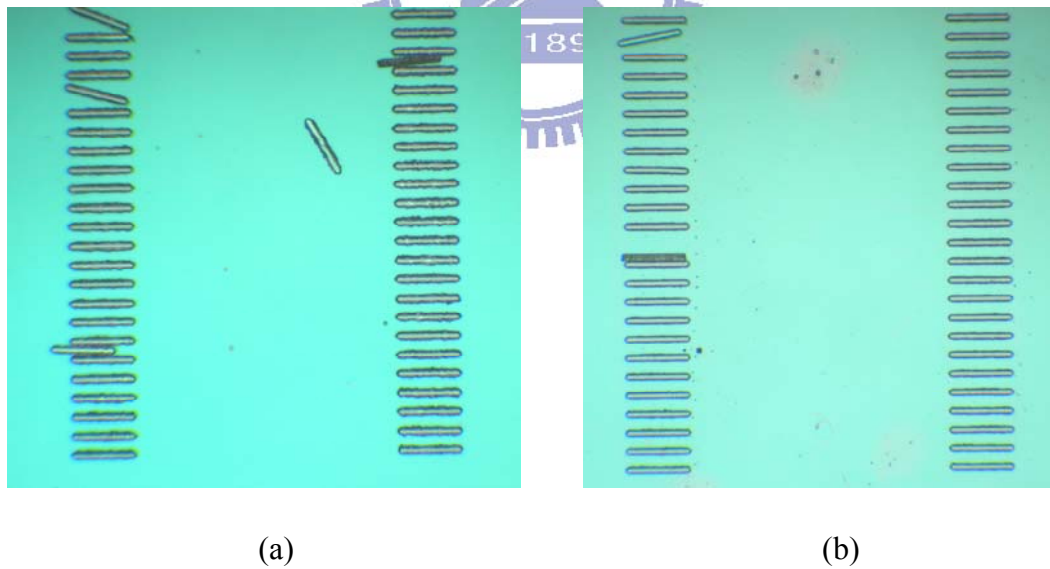
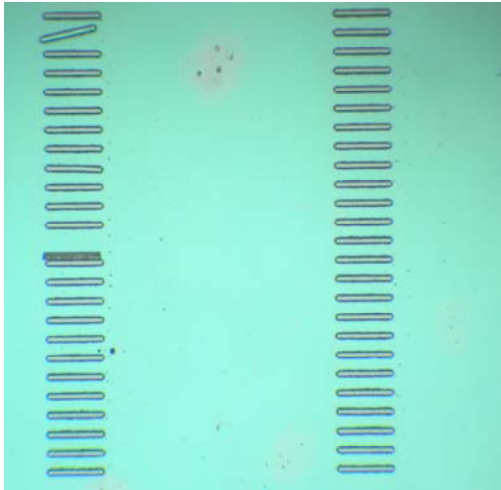
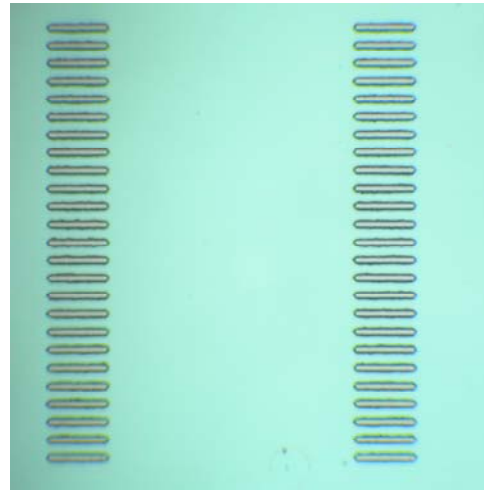


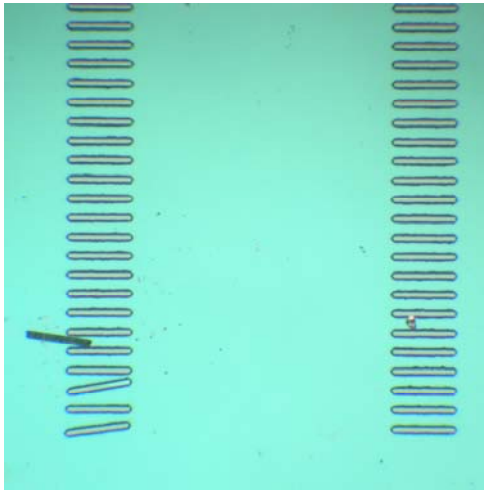
Figure 3-5. Optical micrographs of SU-8 patterns on nitride, (a) without HMDS and (b) with HMDS.



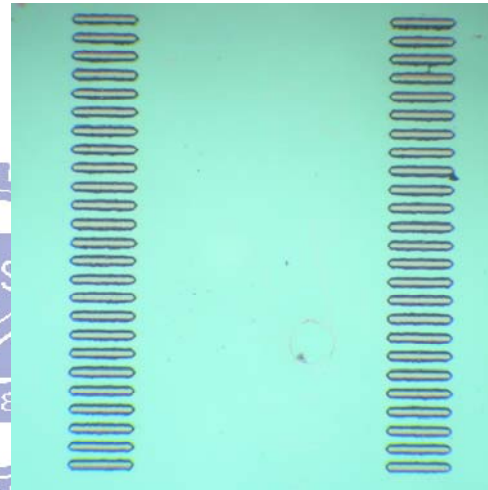
(a) 1X



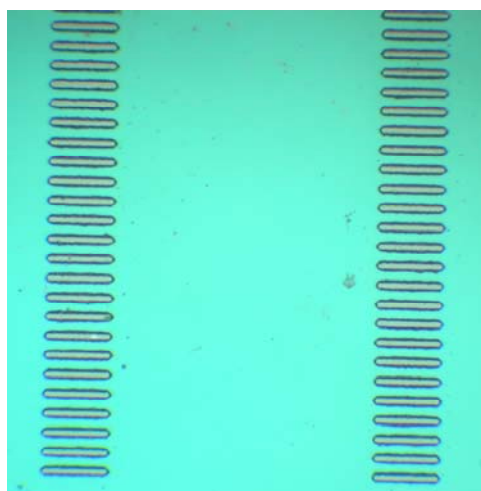
(b) 1.25X



(c) 1.5X



(d) 1.75X



(e) 2X

Figure 3-6. SU-8 patterns with different exposure dose, (a) 1 X, (b) 1.25 X, (c) 1.5 X, (d) 1.75 X and (e) 2 X.

3-3-2 RIE lag phenomenon

The etching rate in silicon deep reactive ion etching (DRIE) is related to the pattern geometry. A frequently observed defect, RIE lag, appears in feature sizes up to hundreds of micrometers [39]. The primary dominating factor in RIE lag is feature width and secondary factors are feature area, shape and length-to-width ratio. The effect becomes more severe for smaller feature width and larger etching depth. In general, the smaller the feature size, the lower the etching rate and the more obvious the RIE lag. In order to avoid the RIE lag phenomenon, the back side pattern should be modified to have constant feature width as shown in Figure 3-7. The extra patterns are removed during HF vapor releasing. Figure 3-8 shows the optical micrographs of the devices with and without the RIE lag phenomenon.

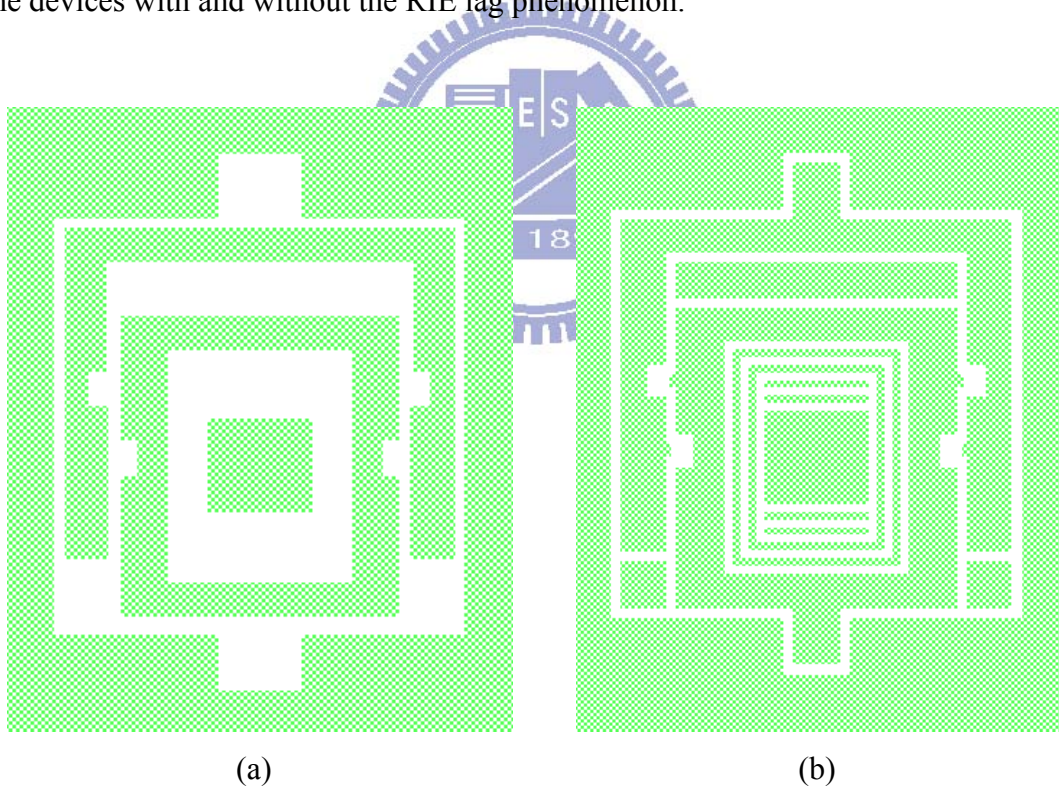


Figure 3-7. Back side patterns, (a) pattern without RIE lag prevention, (b) pattern with constant feature width.

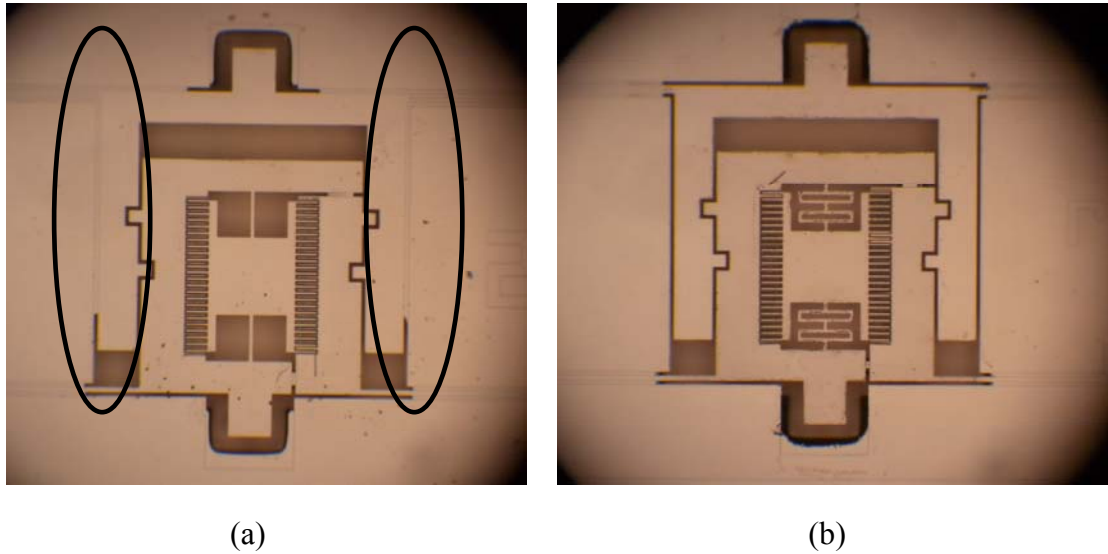


Figure 3-8. Optical micrographs of the device, (a) with RIE lag phenomenon, (b) without RIE lag phenomenon.

3-3-3 Thermal release tape problem

A thermal release tape was used to fix the chip on the carrier wafer during the back side etching. The entire chip has to be stuck on the thermal release tape for better thermal conductivity and etching performance. Poor thermal conductivity would result in lower selectivity between the silicon and the oxide as well as pattern deformation. Figure 3-9 shows the devices under different thermal conductivities.

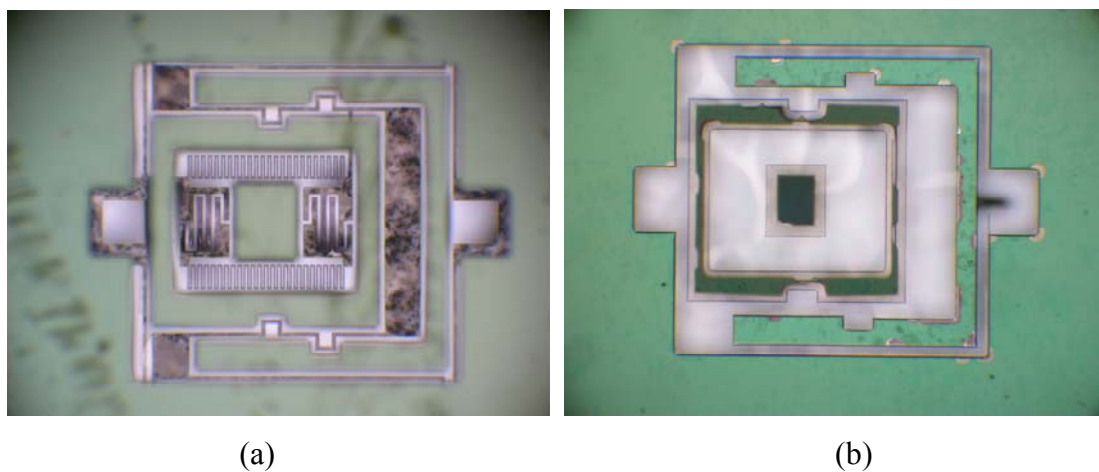


Figure 3-9. Optical micrographs of the devices, (a) with good thermal conductivity and (b) with poor thermal conductivity.

After back side etching, the chip can be removed from the thermal release tape by heating the carrier wafer. But structures such as mirror plates and supports in the device layer could stick on the thermal release tape due to residual stickiness as shown in Figure 3-10. Immersing the heated carrier wafer in isopropyl alcohol (IPA) for 5 minutes can slightly improve this stiction problem. Increasing the thickness of the device layer of the SOI wafer could enhance the structure strength to avoid the stiction problem. Etching the back side prior to the front side etching can avoid this problem because the thermal release tape would not be needed.

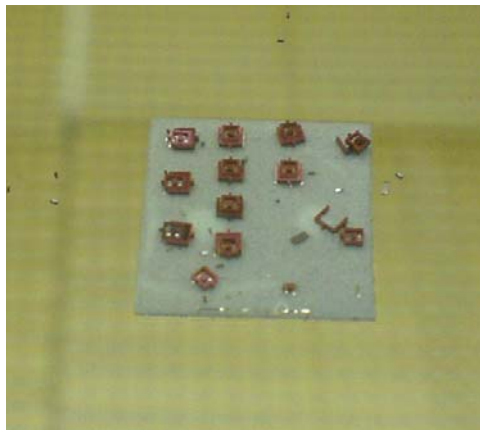


Figure 3-10. Devices stuck on the thermal release tape.

3-3-4 Release problem

HF vapor was used to etch the buried oxide to release the structure. Silicon nitride was also etched by HF vapor with a lower etching rate compared to oxide. But the selectivity was lower than expected. Therefore, the nitride underneath the SU-8 was under-cut and it resulted in the peel-off of the SU-8. Figure 3-11 shows the optical micrograph of the peeled-off SU-8 after 6 hours of releasing. Therefore, the release time has to be minimized to release the moving part of the mirror without peeling-off of SU-8. However, the limited release time can not release the torsional beams of the plate and the support. This problem can be solved by patterning SU-8 on

silicon instead of nitride to avoid the under cut problem. The release time can thus be extended until the torsional beams are released. Therefore the mirror can be flipped up and assembled.

During the HF vapor etching of nitride, residues are created according to [40]:



These residues form a white, non-transparent film on the surface of the mirror plate. It causes an apparent increase in the average roughness. Table 3-1 shows the roughness comparison between four different chips measured by a WYKO surface profilers. It can be found that the residues increased the average roughness from 4.85 nm to 60.22 nm. After all residues were etched, the surface of the mirror plate was silicon and the roughness was decreased to 1.22 nm. Gold deposition on the residues can improve the average roughness from 60.22 nm to 39.89 nm. Figure 3-12 shows the optical micrographs of the mirror plate of the samples.

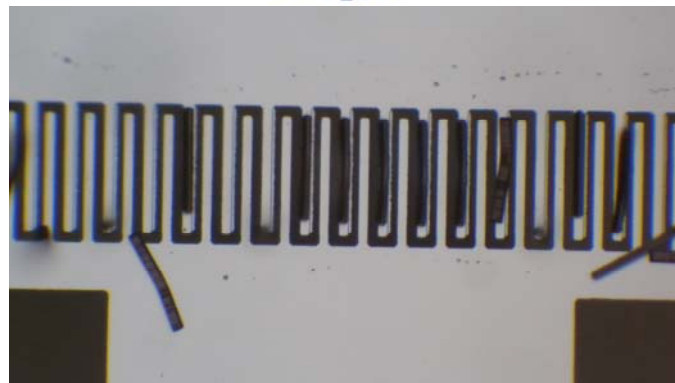


Figure 3-11. Optical micrograph of the peeled-off SU-8.

Table 3-1. Roughness comparison.

No.	Sample	Ra (average roughness)
1	Unreleased (with nitride)	4.85 nm
2	Released for 2 hours	60.22 nm
3	Gold coating on the sample 2	39.89 nm
4	Released for 6 hours (silicon only)	1.22 nm

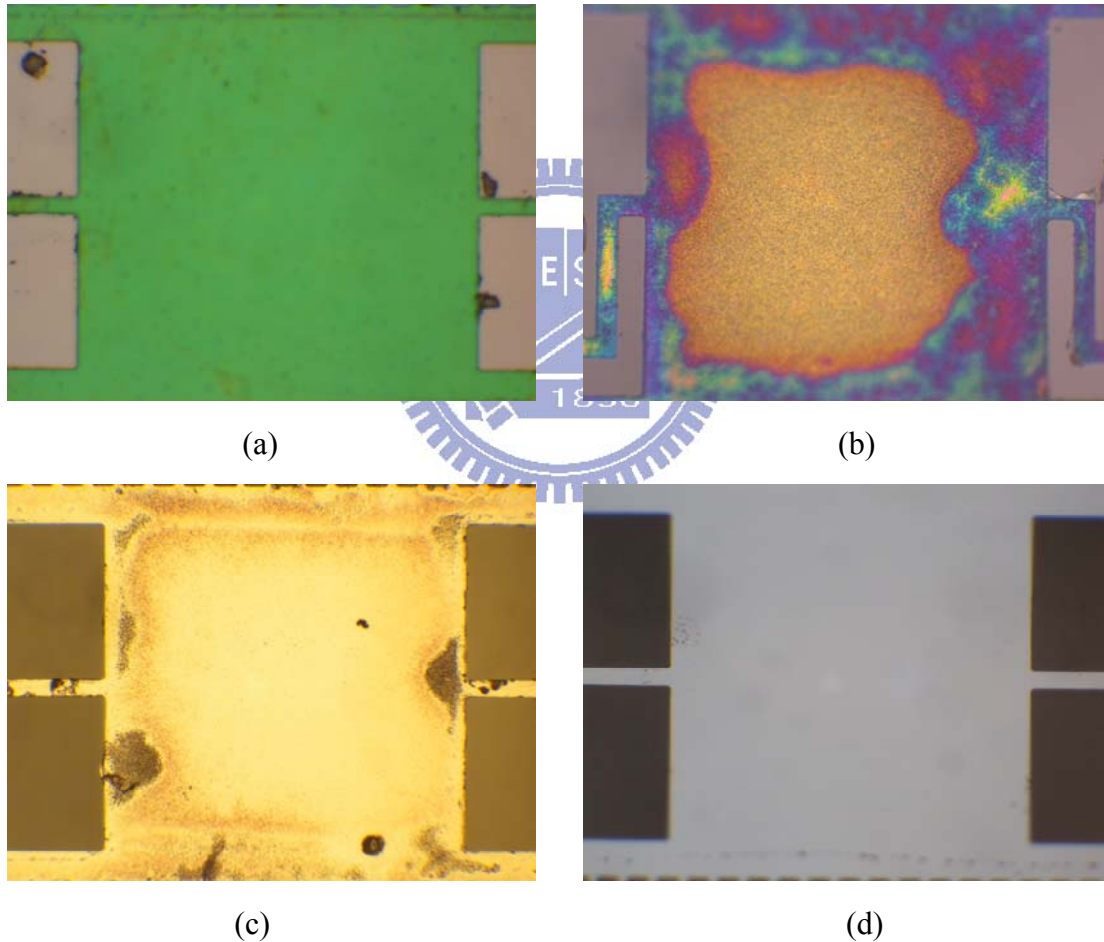


Figure 3-12. Optical micrographs of the mirror plate, (a) unreleased, (b) released for 2 hours, (c) gold coating on the 2 hours released mirror and (d) released for 6 hours.

3-4 Summary

The fabrication results and problems were presented. SEM micrographs of the fabricated devices are shown in Figure 3-13. Figure 3-13 (a) shows the top view of the box type mirror before back side ICP. Figure 3-13 (b), (c) and (d) show the fabricated structure. Figure 3-13 (b) shows the broken torsional beam. Figure 3-13 (c) shows the vertical comb actuator. Figure 3-13 (d) shows the electrical isolation.

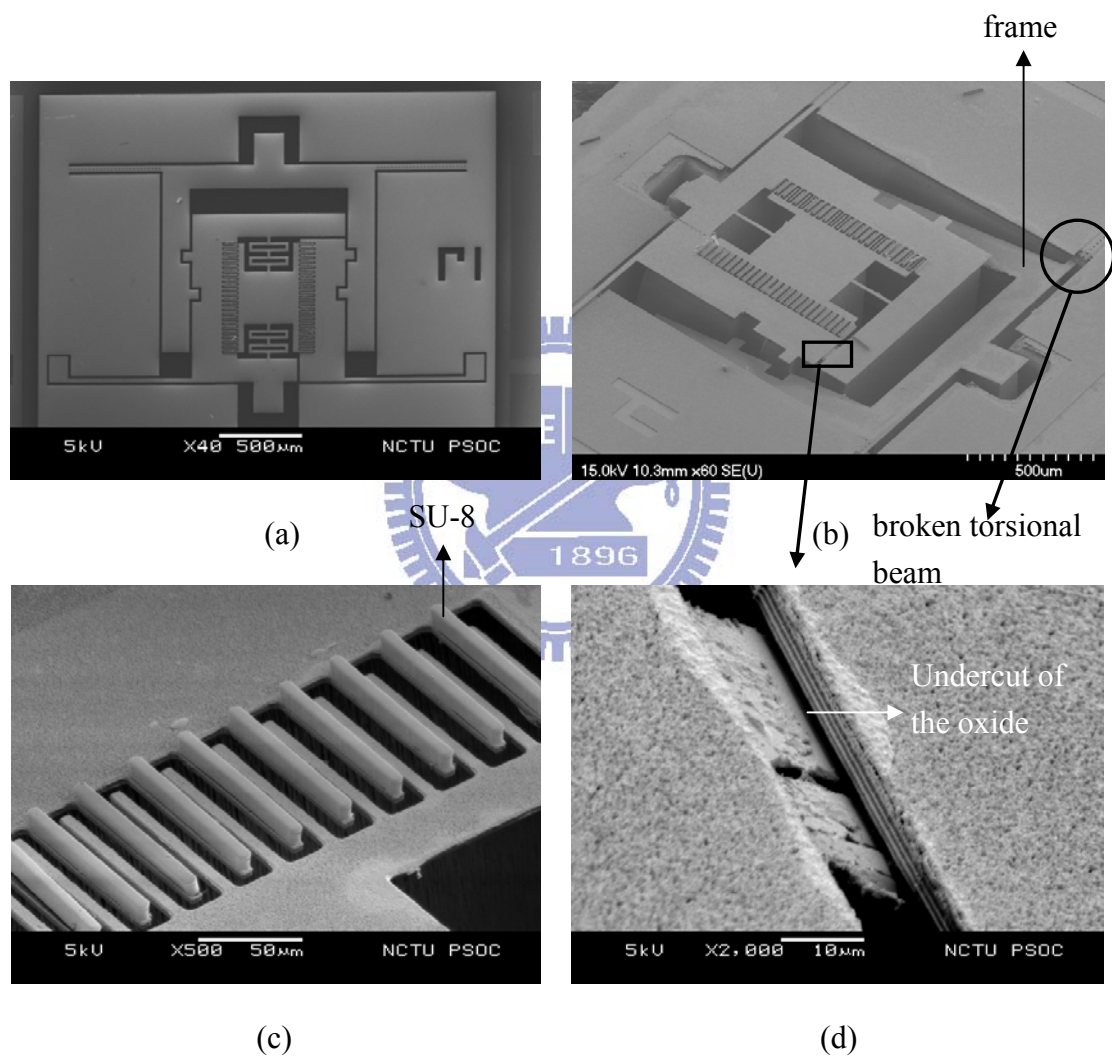


Figure 3-13. SEM micrograph of the devices, (a) top view of the mirror before back side ICP, (b) fabricated mirror and frame with broken torsional beam, (c) vertical comb actuator and (d) electrical isolation.

Figure 3-14 shows the SEM micrographs of the assembled device. But the mirror was locked by the friction between the interlock and the sidewall of the mechanical connection substrate. The assembled angle calculated from pixel coordinates is 33.67° . Figure 3-14 (a) shows the flip-up device and it can be seen the SU-8 has peeled-off. Figure 3-14 (b) shows the side view of the assembled mirror. Figure 3-14 (c) shows the mislocked interlock. Figure 3-14 (d) shows the torsional beam of the flip-up frame.

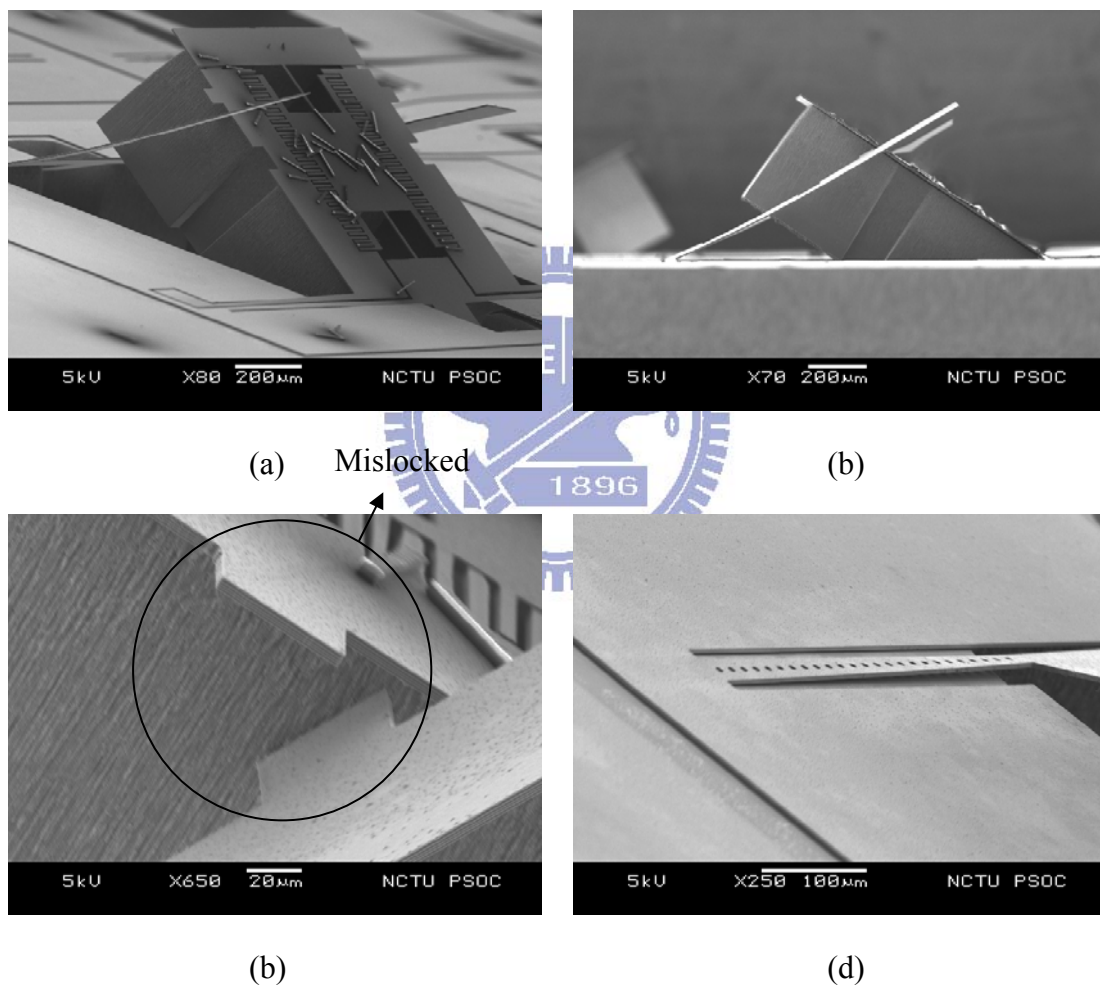


Figure 3-14. SEM micrographs of the assembled mirror, (a) mirror with peeled-off SU-8, (b) side view of the mirror, (c) mislocked interlock and (d) torsional beam of the flip-up frame.

Chapter 4

Measurement and Results

This chapter presents the experiment setups and the measurement results of the static and the dynamic performance of the micro scanning mirror. The measurement results are compared with the simulations in Chapter 3. Suggestions for future device redesign are discussed.

4-1 Surface profile measurement

The residual stress after HF release and gold coating causes bending of the structure. And the nitride residues increase the roughness of the mirror surface. Three samples were measured by a WYKO NT1100 optical profiler. Sample A was released for 6 hours and the nitride layer was all etched. The torsional beams for assembly were totally released. Sample B was released for 2 hours and the nitride layer was not etched entirely. The residues of nitride etching mentioned in Chapter 3 can be seen on the surface. The mirror plate, vertical comb fingers, and torsional springs were released, but the torsional beams for assembly were not. Sample C was released for 2 hours and a 5000 Å gold layer was coated. The micro scanning mirror can be actuated but can not be flipped up because the torsional beams for assembly were not released.

Sample A

Figure 4-1 shows the bending of the released part of the mirror. By comparing the flat area with the mass block under the mirror as shown in Figure 4-1 (b), about 50 μm undercut of the oxide can be found. It can be concluded the rate of HF vapor etching is about 8.3 μm per hour. The radii of curvature of the flat area mirror in the x-direction and y-direction are -6.62 m and -2.49 m, respectively. The roughness of the flat area is 1.22 nm as shown in Figure 4-2. Figure 4-3 shows the measurement of the torsional spring. The radius of curvature is -98.14 mm.

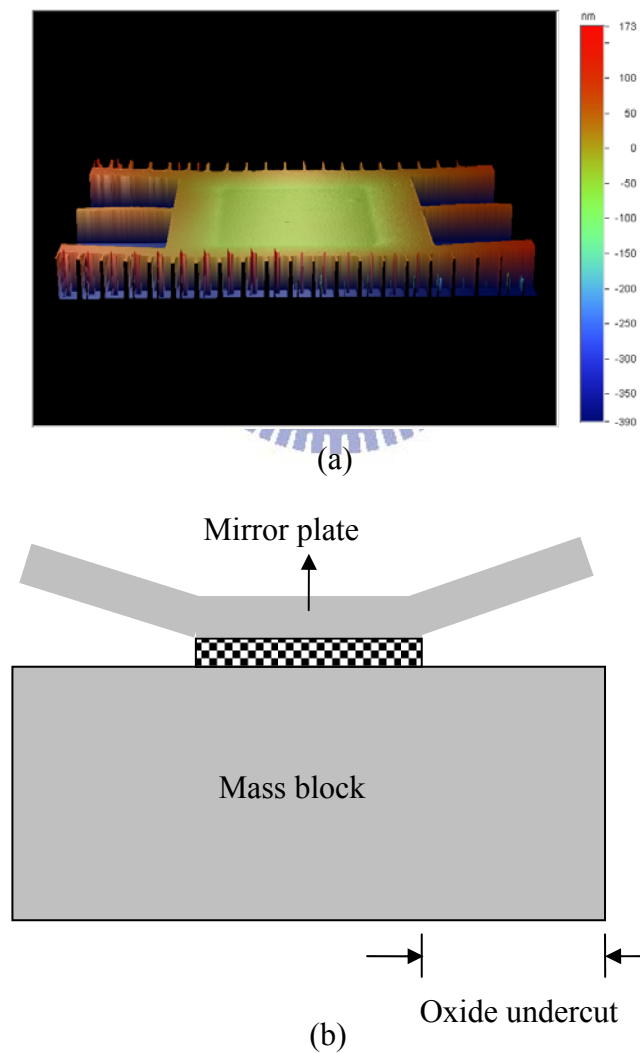
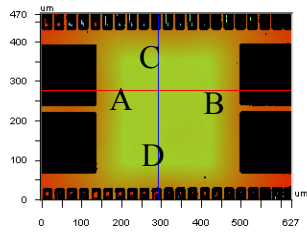
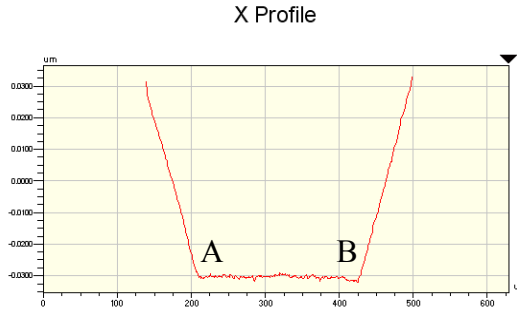


Figure 4-1. Bending of the mirror plate of sample A, (a) 3-D profile, (b) cross section schematic of the mirror plate.



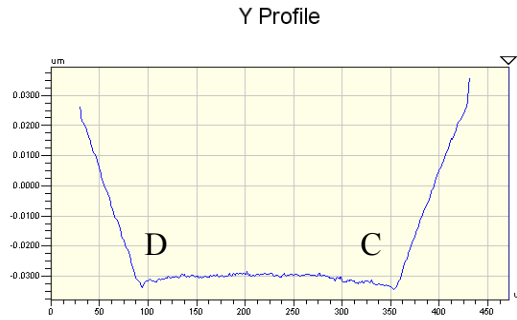
X	291.55	-	-	um
Y	276.83	-	-	um
Ht	-29.73	-	-	nm
Dist	-	-	-	um
Angle	-	-	-	°

Title:



Rq	0.02 um
Ra	0.02 um
Rt	0.07 um
Rp	0.03 um
Rv	-0.03 um

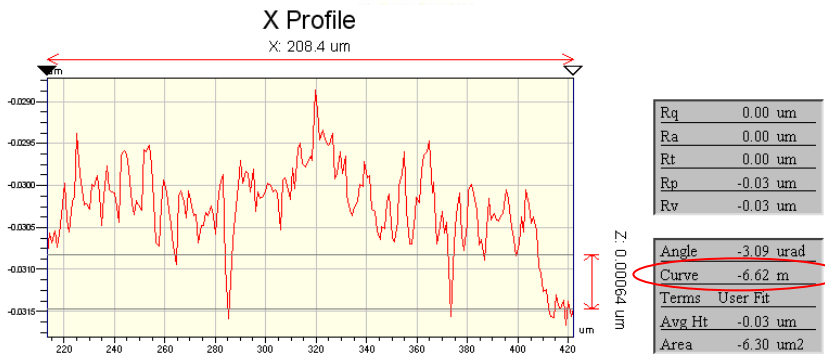
Angle	0.00 mrad
Curve	0.28 m
Terms	None
Avg Ht	-0.02 um
Area	-11.45 um ²



Rq	0.02 um
Ra	0.01 um
Rt	0.07 um
Rp	0.04 um
Rv	-0.03 um

Angle	0.00 mrad
Curve	0.40 m
Terms	None
Avg Ht	-0.02 um
Area	-9.88 um ²

(c)



Rq	0.00 um
Ra	0.00 um
Rt	0.00 um
Rp	-0.03 um
Rv	-0.03 um

Angle	-3.09 urad
Curve	-6.62 m
Terms	User Fit
Avg Ht	-0.03 um
Area	-6.30 um ²

(d)



Rq	0.00 um
Ra	0.00 um
Rt	0.01 um
Rp	-0.03 um
Rv	-0.03 um

Angle	-6.62 urad
Curve	-2.49 m
Terms	None
Avg Ht	-0.03 um
Area	-7.78 um ²

(e)

Figure 4-1. Surface profile of the mirror plate of sample A, (a) 3-D profile, (b) cross section schematic of the mirror plate, (c) 2-D profile, (d) 2D profile of the flat area along A-B and (e) 2D profile of the flat area along C-D (continued).

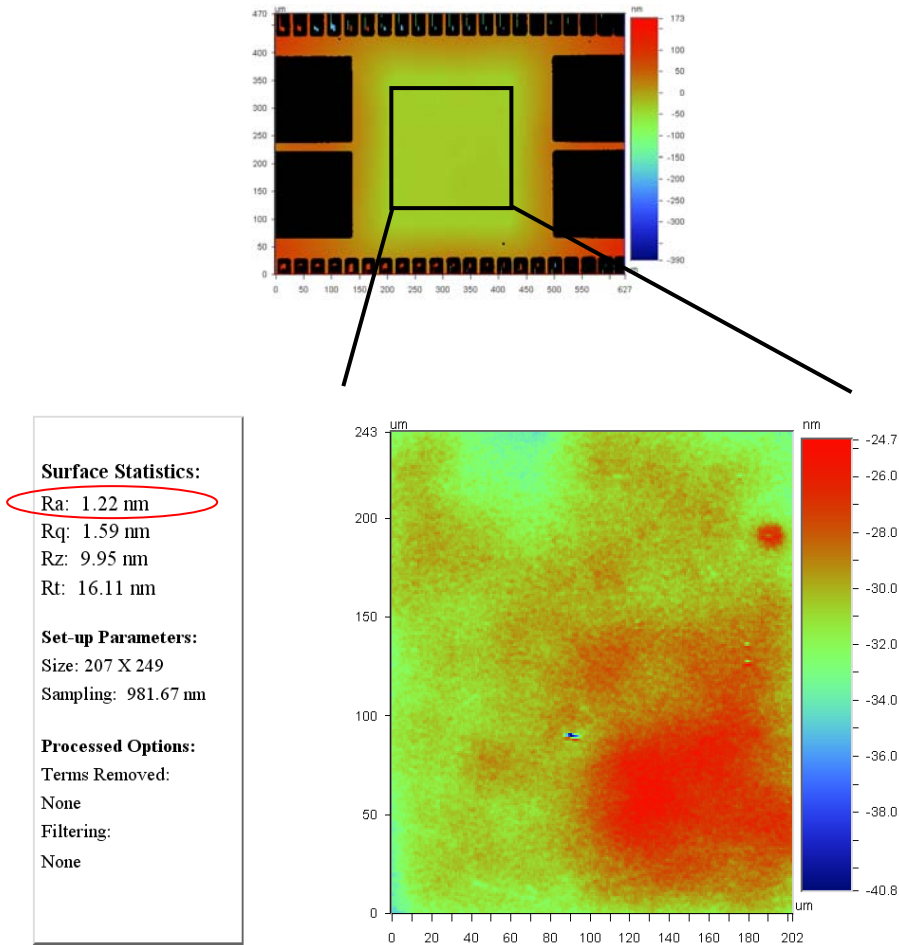


Figure 4-2. Roughness measurement of sample A.

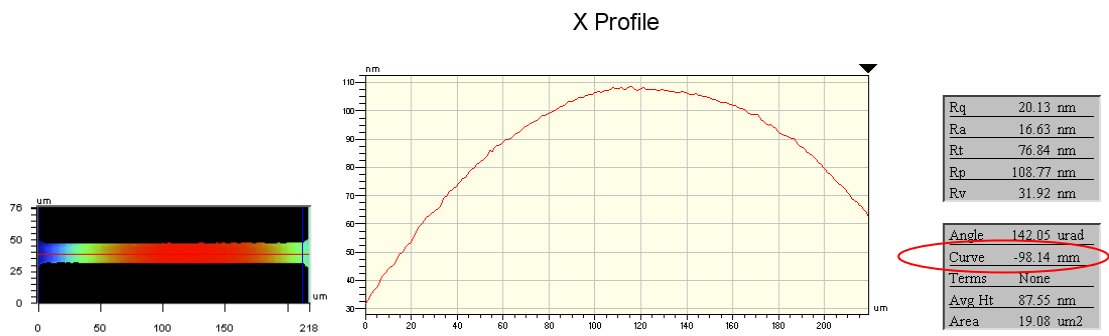


Figure 4-3. Surface profile of the torsional spring of sample A.

Sample B

Sample B was released for two hours and the nitride was not etched entirely as the optical micrograph shows in Figure 4-4. Figure 4-5 shows the surface profile of the mirror plate. The nitride etching residues can be found on the surface. It increases the roughness of the surface from 4.85 nm mentioned in Chapter 3 to 60.22 nm. The surface profile of the spring is shown in Figure 4-6. The average roughness of the spring is 273.76 nm. The rough surface dominates the surface property and bending phenomenon can not be observed.

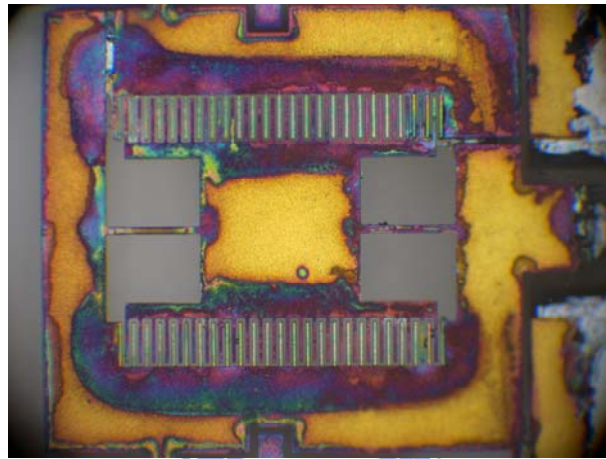
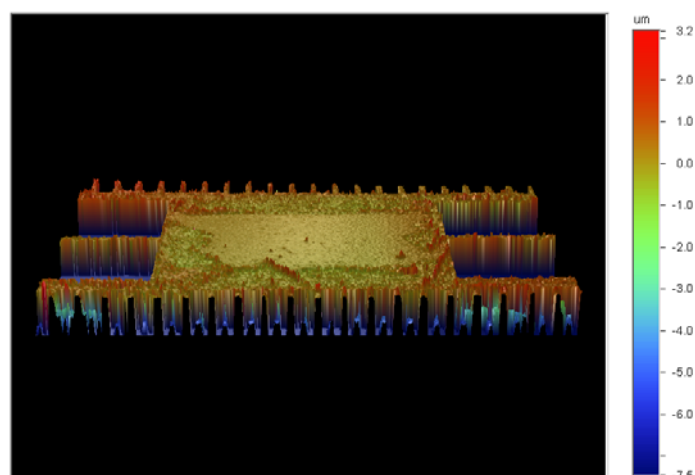
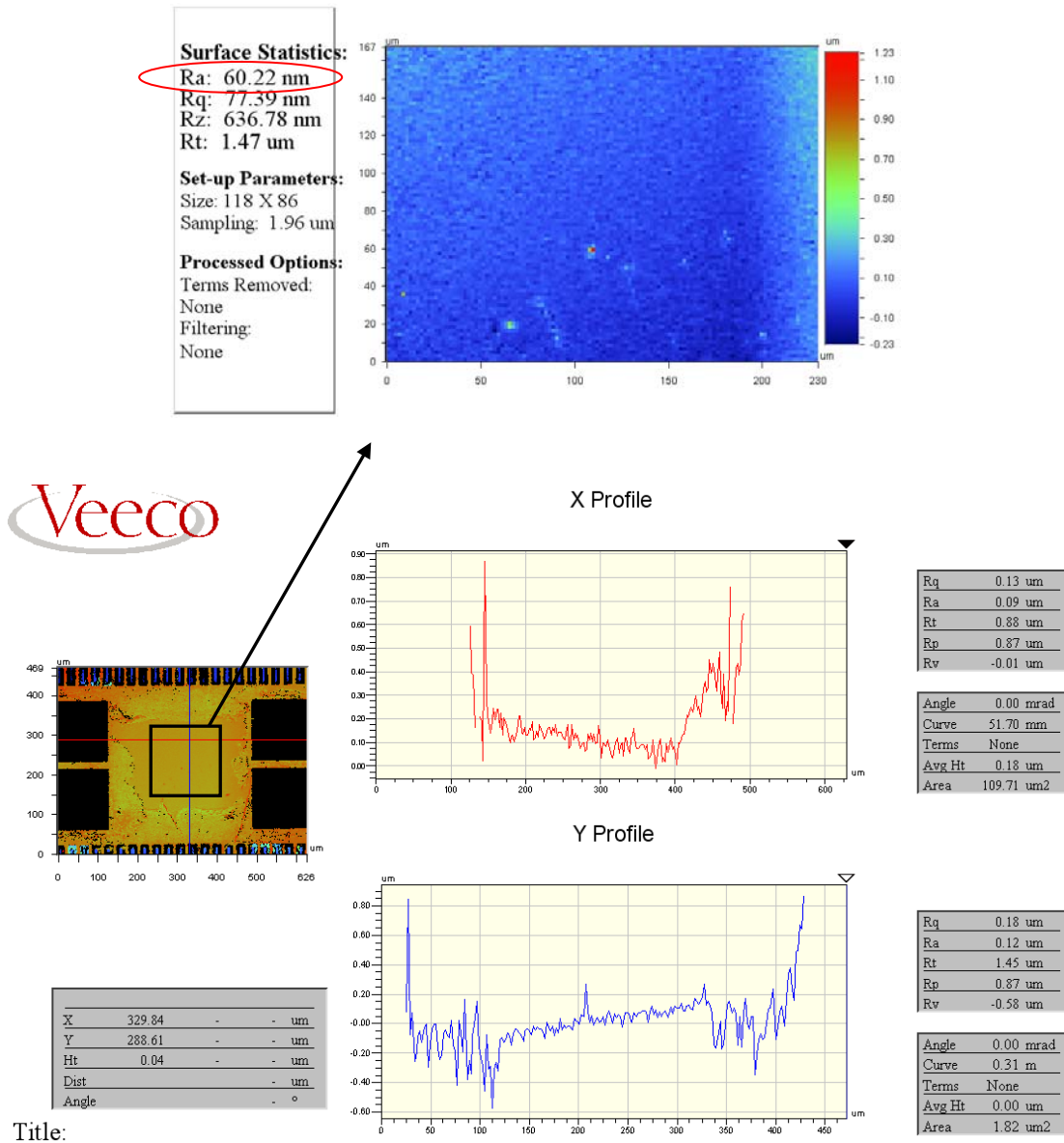


Figure 4-4. Optical micrograph of the micro scanning mirror after 2 hour releasing.



(a)

Figure 4-5. Surface profile of the mirror plate of sample B, (a) 3-D profile and (b) 2-D analysis.



(b)

Figure 4-5. Surface profile of the mirror plate of sample B, (a) 3-D profile and (b) 2-D profile (continued).

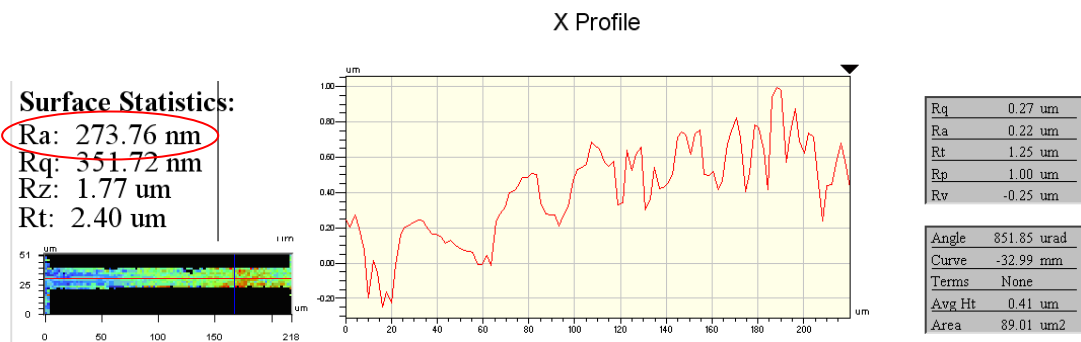


Figure 4-6. Surface profile of the torsional spring of sample B.

Sample C

Sample C was released for 2 hours and a 5000 Å gold layer was coated on the mirror as well as the nitride residues. The optical micrograph is shown in Figure 4-7. Figure 4-8 and Figure 4-9 show the surface profile of the mirror and the spring of sample C. The roughness of the mirror is 39.62 nm. The roughness of the spring is 189.03 nm. The rough surface dominates the surface property and the bending phenomenon can not be observed obviously. Table 4-1 shows the comparison of the three samples.

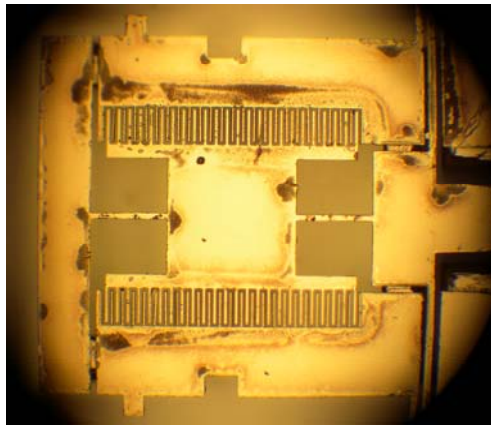
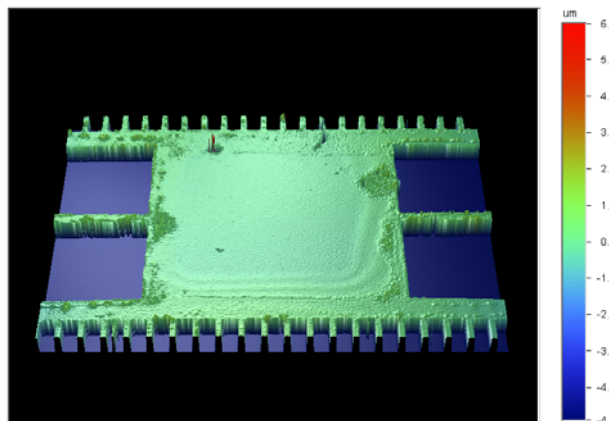


Figure 4-7. Optical micrograph of the micro scanning mirror with gold coating.



(a)

Figure 4-8. Surface profile of the mirror plate of sample C, (a) 3-D profile, (b) 2-D profile.

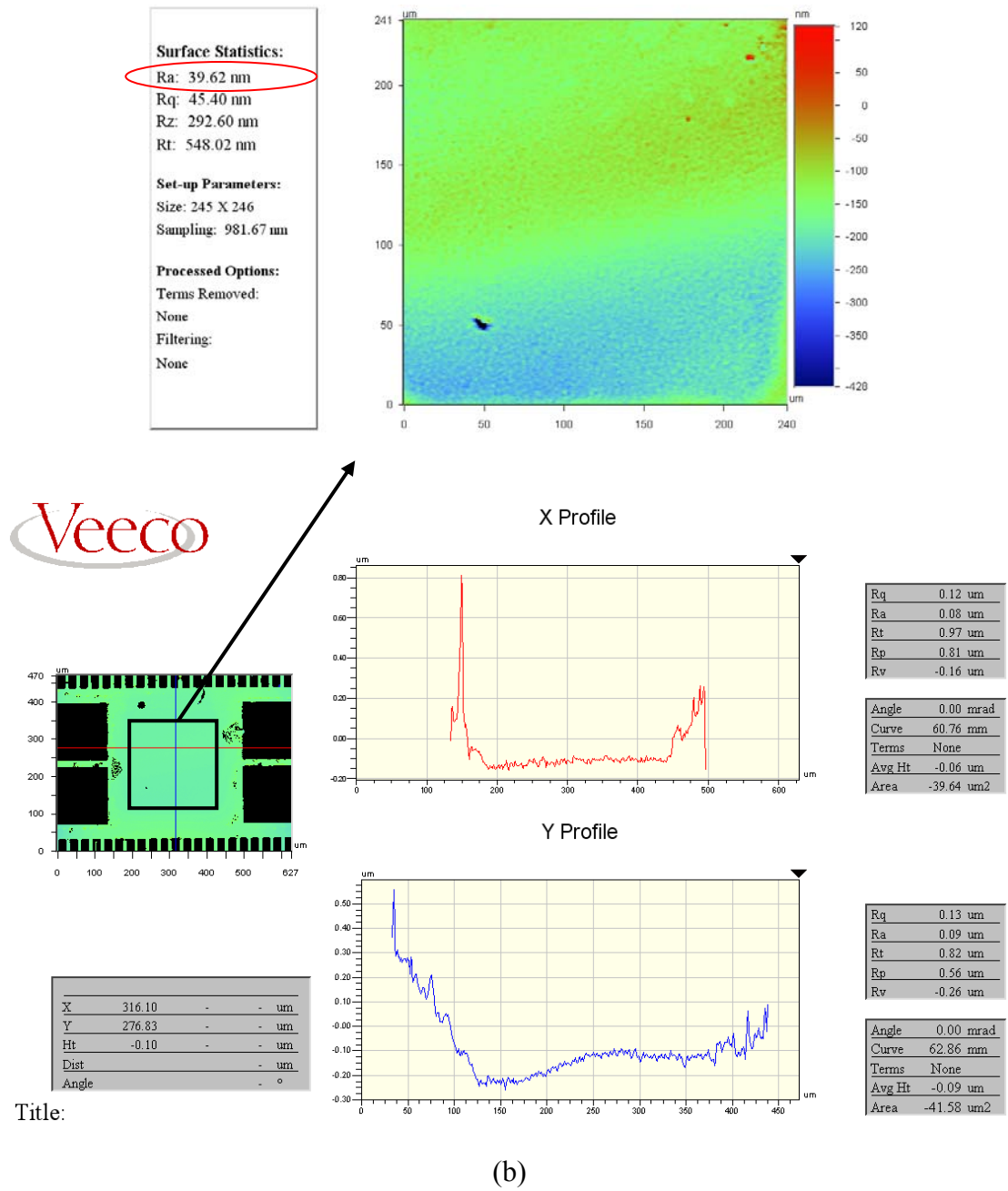


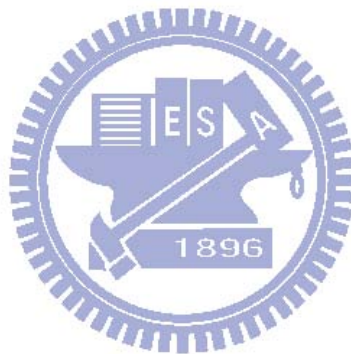
Figure 4-8. Surface profile of the mirror plate of sample C, (a) 3-D profile, (b) 2-D profile (continued).



Figure 4-9. Surface profile of the torsional spring of sample C.

Table 4-1. Comparison of three samples.

	Sample A	Sample B	Sample C
Release time	6 hours	2hours	2 hours (gold coating)
Radius of curvature in x-axis	-6.62 m	-	-
Radius of curvature in y-axis	-2.49 m	-	-
Radius of curvature of the spring	-98.14 mm	-	-
Surface roughness	1.22 nm	60.22 nm	39.62 nm
Spring roughness	-	273.76 nm	189.03 nm



4-2 Static scanning measurement

Figure 4-10 shows the experiment setup to measure the static torsional angle versus applied DC voltage. A Keithley 2400 SourceMeter was connected to the sample to provide DC voltage. A WYKO NT1100 optical profiler was used to measure the deformation of the micro scanning mirror. Figure 4-11 (a) shows the 2D profile of an unactuated beam type micro scanning mirror. Figure 4-11 (b) shows the 2D profile of the 110V actuated beam type mirror. Figure 4-11 (c) shows the difference between the 110V actuated surface profile in Figure 4-1 (b) and the unactuated surface profile in Figure 4-11 (a). The slope of the mirror is the scanning angle. Figure 4-12 compares the measured and simulated static scanning angle. The measured scanning angle is larger than the simulation due to the shrinkage of the photoresist during hard bake that reduced the width of the torsional springs. Figure 4-13 shows the surface profile of the spring. The width is $16.7\ \mu\text{m}$ compared to the designed $20\ \mu\text{m}$. By substituting the value into Equation 2-5, the reduction of the torsional spring width causes about 20 % decrease in the torsional spring constant and thus 20 % increase in the static scanning angle. Figure 4-14 plots the torsional angle of the beam type and meander type micro scanning mirrors. By the equation of the torsion constant of the meander type spring [41], the reduction of the spring width of the meander type causes about 16 % decrease in the static scanning angle. Besides, the shrinkage of the photoresist also causes about 15 % increase in the finger gap. It leads to about 13 % decrease in the electrical torque according to Equation 2-4. The ratio of the torsional spring constants between the beam type and the meander type mirrors is about 2.2 to 2.85. This value is compared with the simulation result of 6.25. After modifying the shrinkage of the photoresist, the measured scanning angle is still larger than the simulation. The frame in simulation was setting as fixed but the measurement was performed before assembly. The simulation also has to be double

checked.

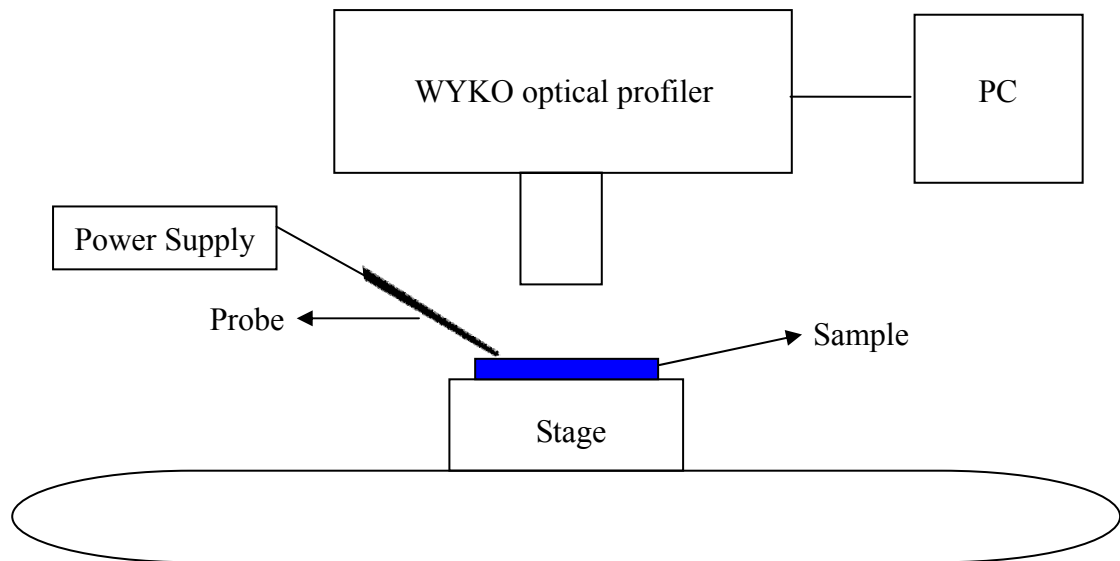
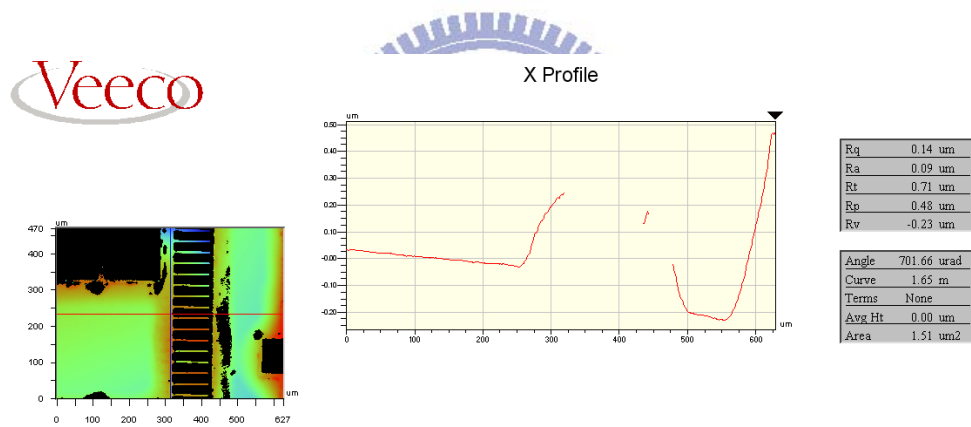
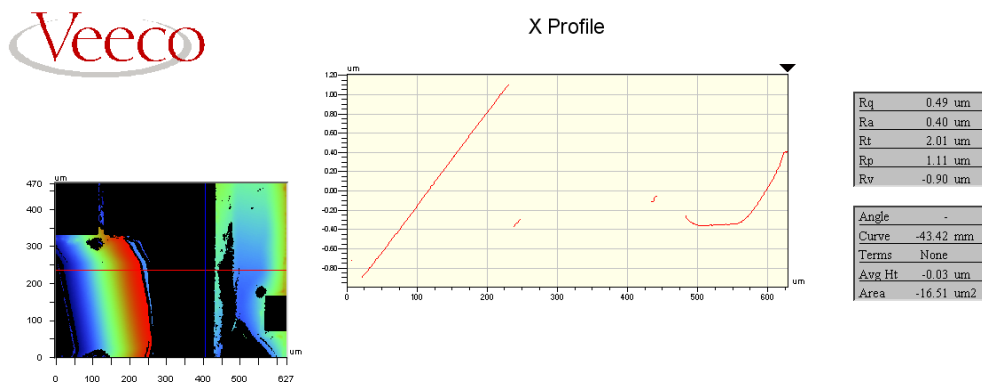


Figure 4-10. Setup of the static scanning measurement.

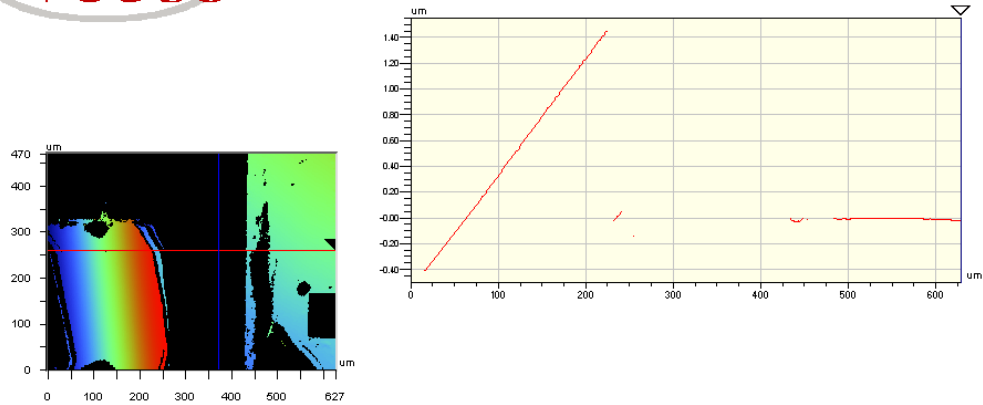


(a)



(b)

Figure 4-11. Static scanning measurements by WYKO optical profiler, (a) unactuated, (b) 110V actuating.



(c)

Figure 4-11. Static scanning measurements by WYKO optical profiler, (a) unactuated, (b) 110V actuation and (c) difference between unactuated and 110V actuation profiles (continued).

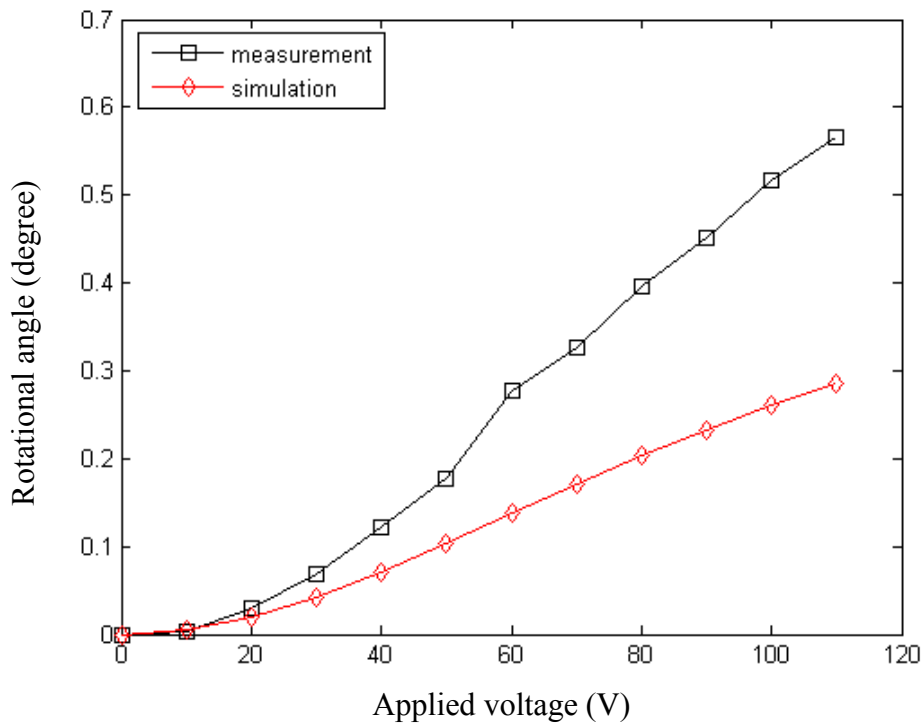


Figure 4-12. Measured and simulated static scanning angle versus applied voltage.

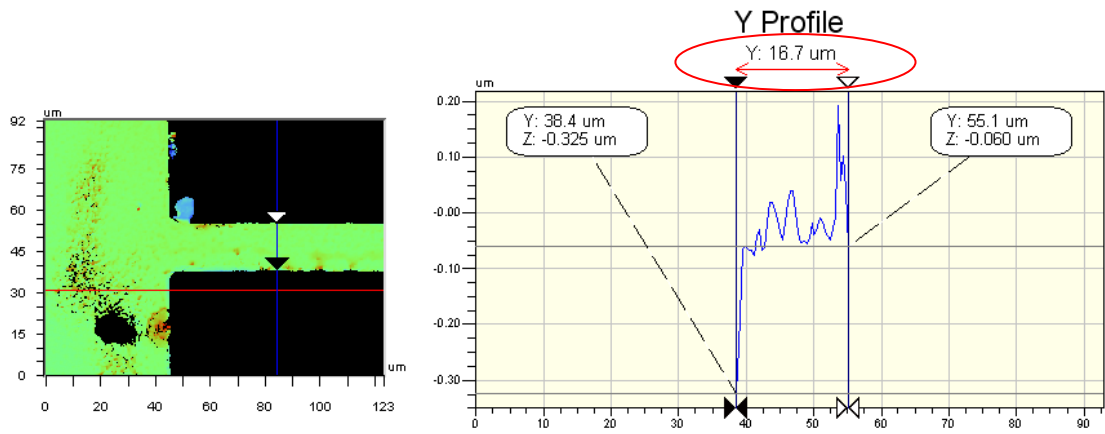


Figure 4-13. Surface profile of the spring.

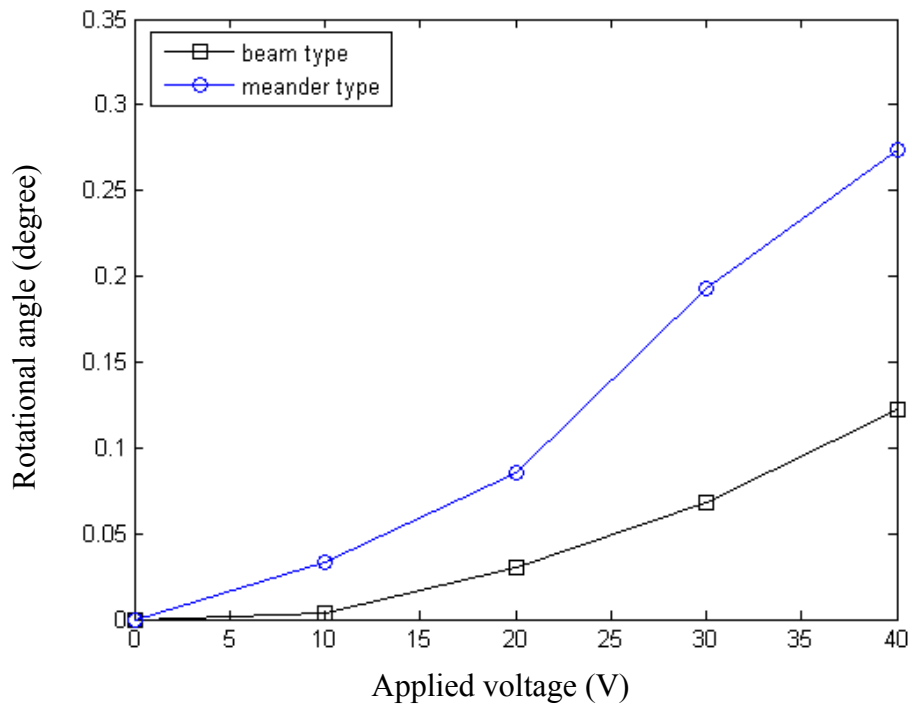


Figure 4-14. Static scanning angle of the beam type and the meander type scanning mirror.

4-3 Dynamic scanning measurement

Figure 4-15 shows the experiment setup to measure the resonant frequency and the mode shape of the micro scanning mirror. A Polytec scanning Doppler vibrometer (MSV300) measured the frequency variance of the reflected laser to construct the motion of the sample. The power supply and the laser were controlled by the vibrometer. A DC ($V_{DC}=5\text{ V}$) and an AC ($V_{AC}=\pm 5\text{ V}$) chirping signal with frequency from 0 Hz to 5 kHz with a 3.125 Hz frequency spacing was applied to the driving electrode.

For the mirror with meander type springs, the measured frequency response is shown in Figure 4-16. The quality factor is about 80 obtained from the frequency response data. The comparison between the measured and the simulated resonant frequency is shown in Table 4-2. The resonant modes are shown in Figure 4-17. The measured frequencies are lower than the simulated values due to reduced spring constant as shown in the previous section. By substituting the value into Equation 2-7, the 15 % reduction of the spring width causes about 9 % decrease in the resonant frequency. Though the gold coating ($0.5\ \mu\text{m}$) is much thinner than the mass block, it slightly contributes to the mass of the mirror since its density is 8 times higher than silicon. The increased mass causes about 1 % in frequency decrease from Equations 2-7 and 2-8. The springs also become weaker than the original design due to overetching in DRIE process. Besides, the mirror as well as the frame were released and without assembly. Therefore the frame was also vibrated at the frequency.

The mass block was used to prevent the bending of the mirror. However, the centrifugal force caused by the vibrating mass block would induce a displacement perpendicular to the mirror plate. The deformed torsional spring also led to an offset of the torsional constant. A thick device layer of the SOI wafer can be chosen to prevent bending without the mass block in the future.

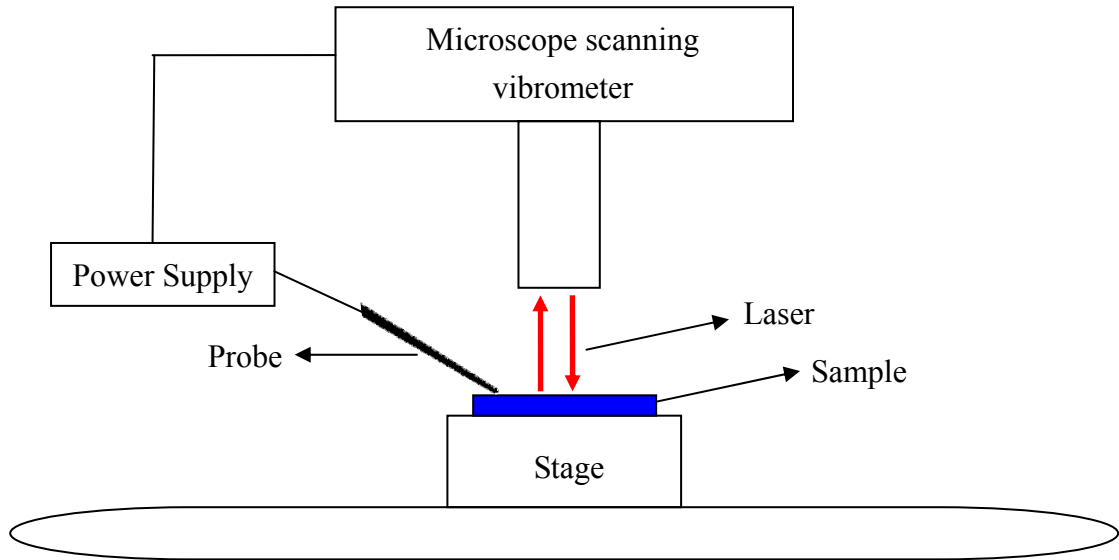


Figure 4-15. Setup of the dynamic scanning measurement.

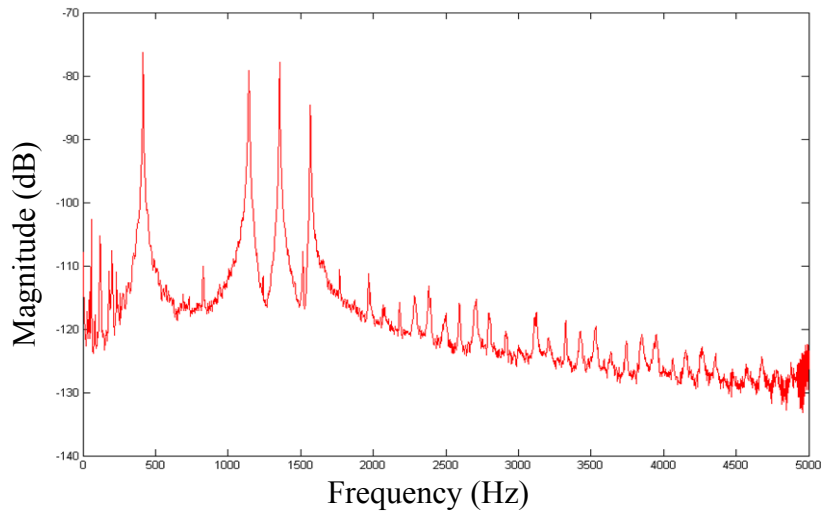


Figure 4-16. Frequency response of a meander type scanning mirror.

Table 4-2. Comparison between the simulation and measurement results of a meander type scanning mirror.

Mode	Simulation	Measurement	Description
Mode 1	0.496 kHz	0.4125 kHz	Rotation around spring
Mode 2	1.483kHz	1.1438 kHz	Piston motion
Mode 3	1.728 kHz	1.3563 kHz	Rotation around the axis
Mode 4	10.978 kHz	1.5656 kHz	perpendicular to the spring.

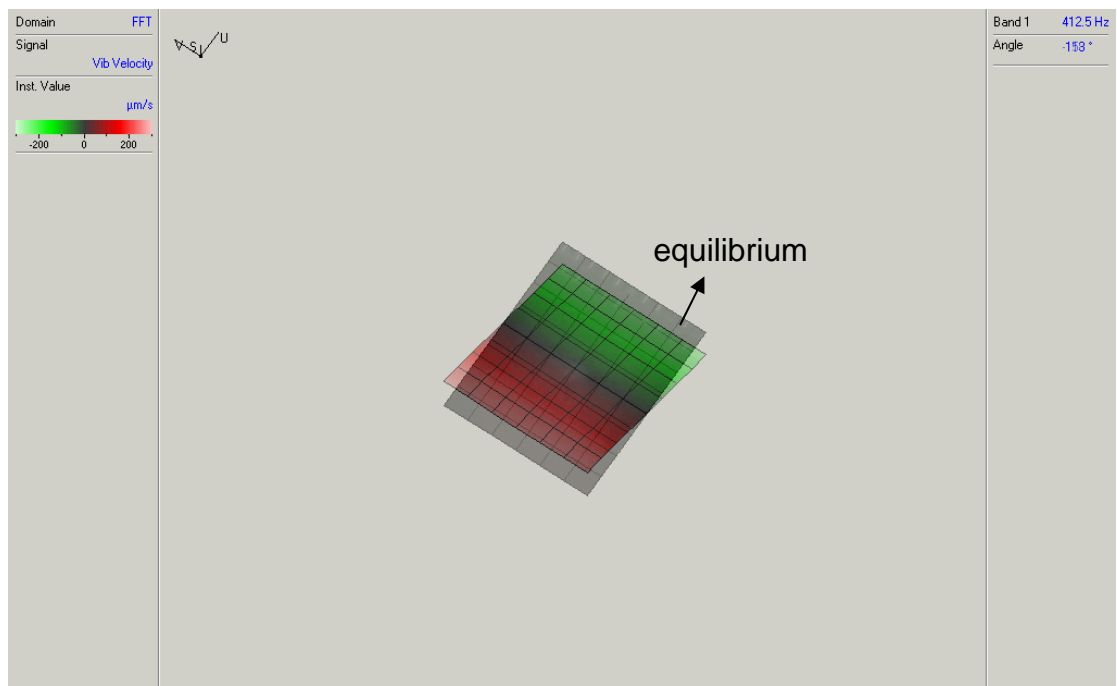
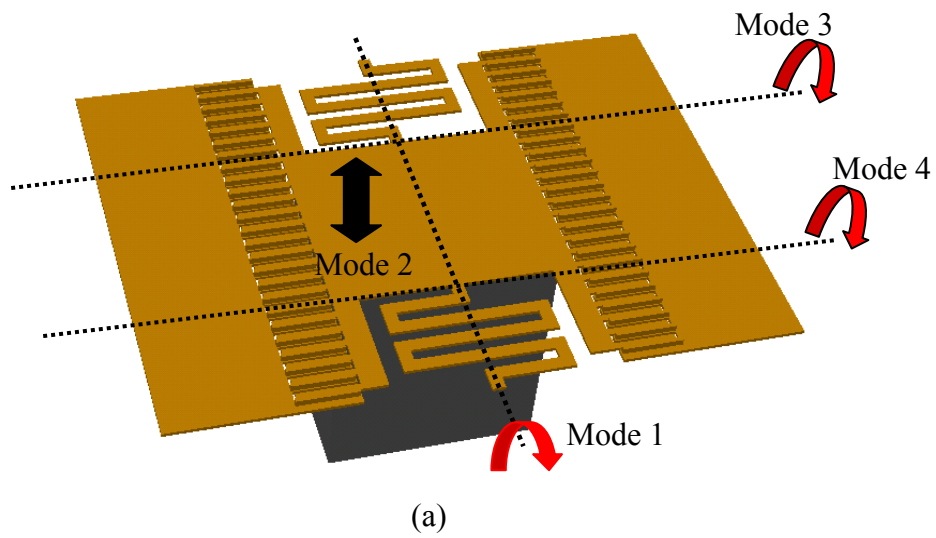
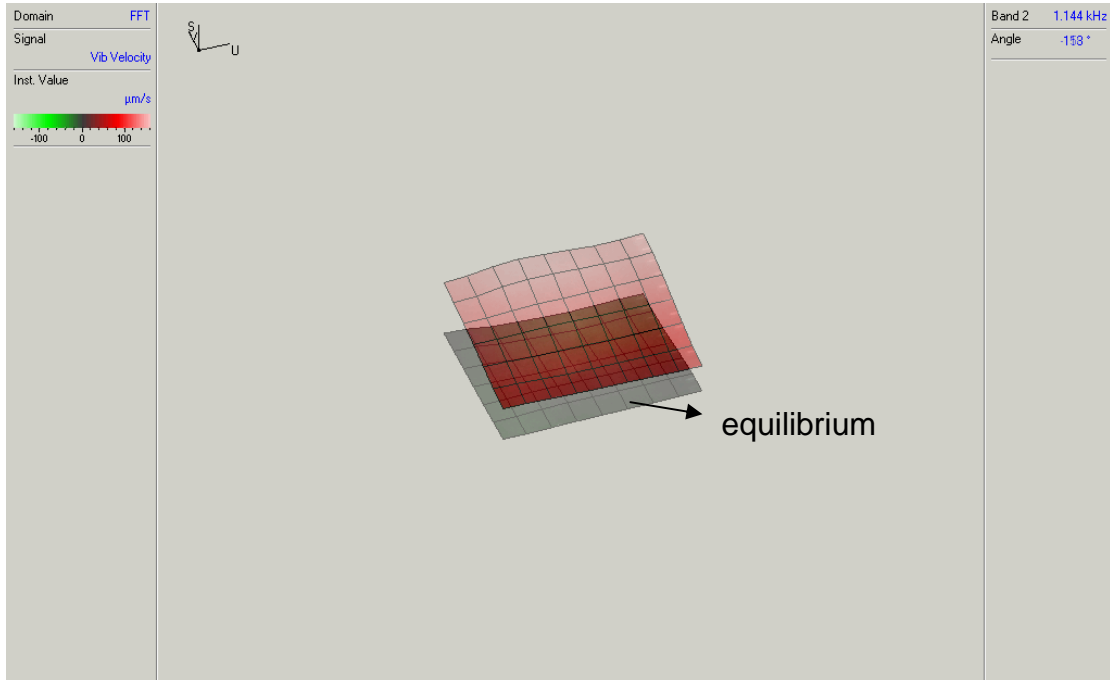
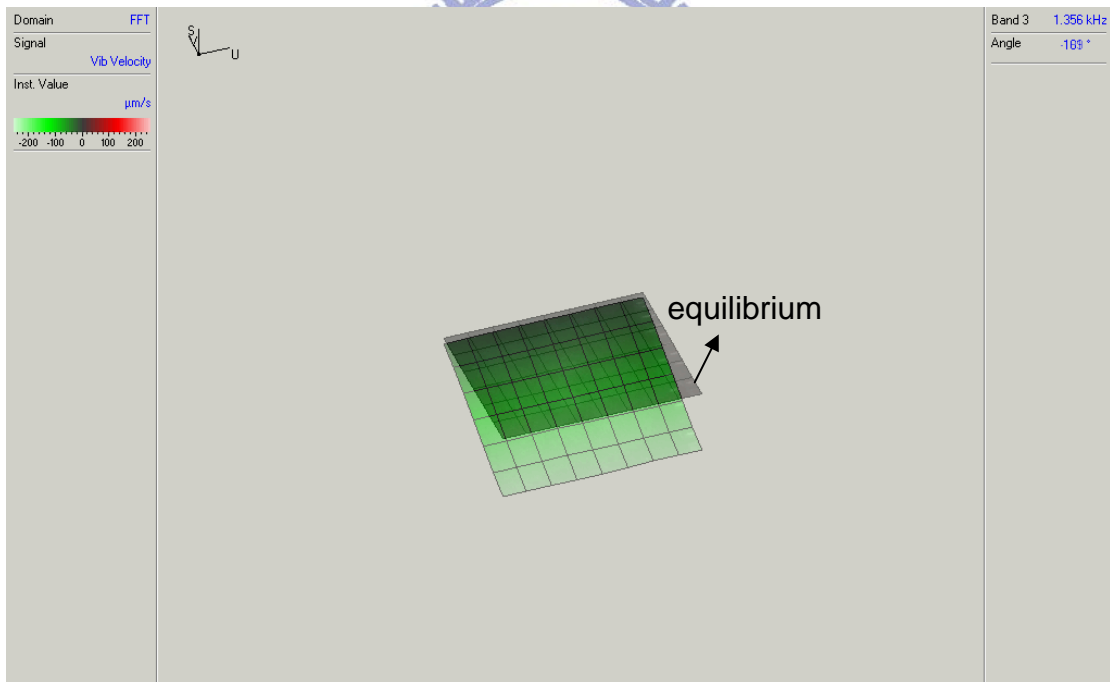


Figure 4-17. Illustration of the resonant modes, (a) schematic of four modes ,(b) mode 1, (c) mode 2, (d) mode 3 and (e) mode 4.

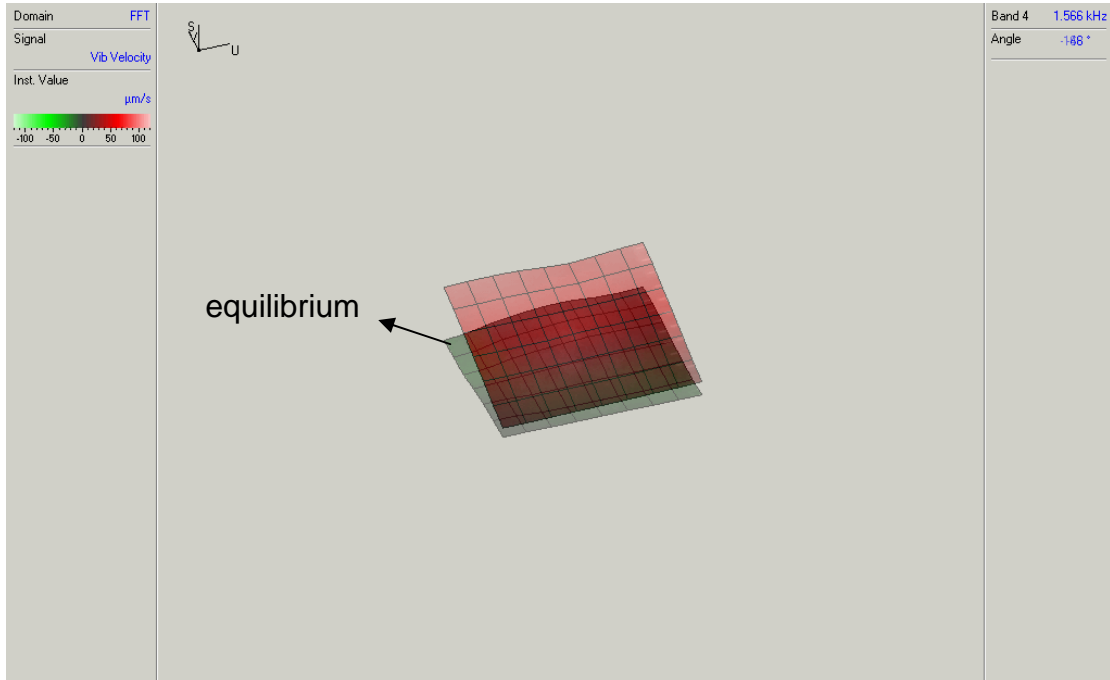


(c)



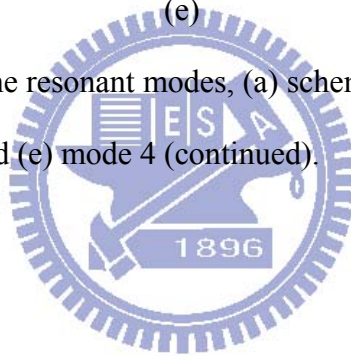
(d)

Figure 4-17. Illustration of the resonant modes, (a) schematic of four modes, (b) mode 1, (c) mode 2, (d) mode 3 and (e) mode 4 (continued).



(e)

Figure 4-17. Illustration of the resonant modes, (a) schematic of four modes, (b) mode 1, (c) mode 2, (d) mode 3 and (e) mode 4 (continued).



4-3-1 Optical scanning measurement

A simple optical scanning experiment was conducted to measure the scanning angle of the meander type scanning mirror at the first resonant frequency. The setup is shown in Figure 4-18. A DC ($V_{DC}=5\text{ V}$) and an AC ($V_{AC}=\pm 5\text{ V}$) sinusoidal signal at the resonant frequency was applied to the electrode. The laser was reflected by the mirror and projected to the screen. The distance between the mirror and the screen is 2 m. The images on the screen are shown in Figure 4-19. When the input frequency is 412.5 Hz, the scan length of the image is 1.7 cm, corresponding to a 0.487° full optical scan angle ($\pm 2\theta_s$). When the input frequency is 413.6 Hz, the scan length of the image is 2.8 cm, corresponding to a 0.802° full optical scan angle ($\pm 2\theta_s$). The 1.1Hz difference in resonant frequency between the dynamic and optical measurements is due to the finer frequency resolution in the latter measurement. Compared to the 0.033° single-sided DC scanning angle depicted in Figure 4-14, the half dynamic scan angle 0.201° (θ_s) has a gain of 6.1 while operating at the resonant frequency.

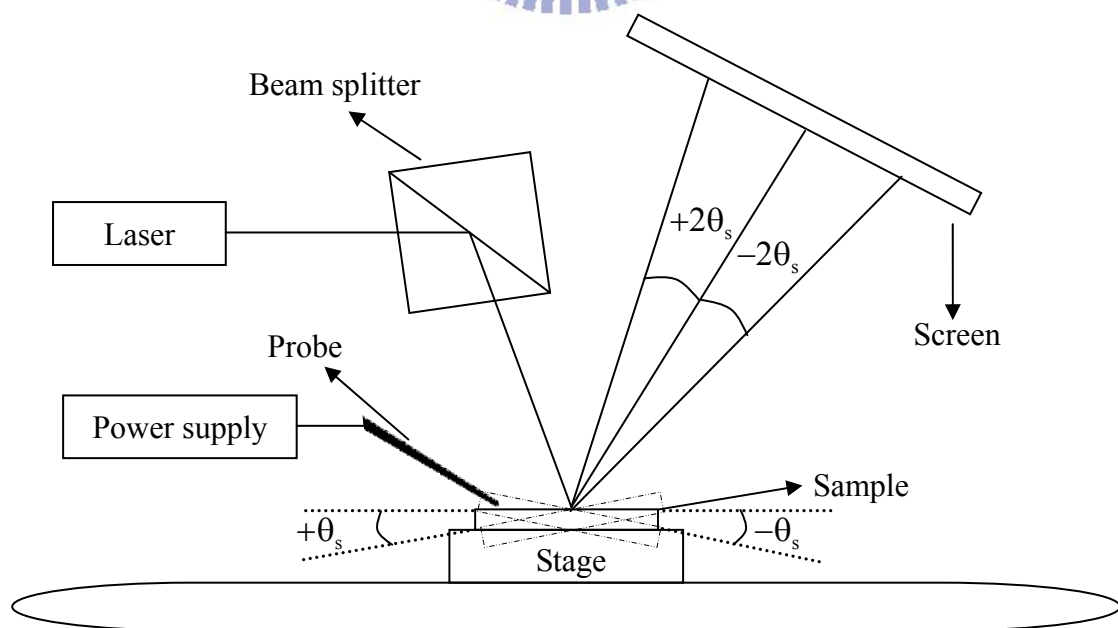


Figure 4-18. Setup of the optical measurement.

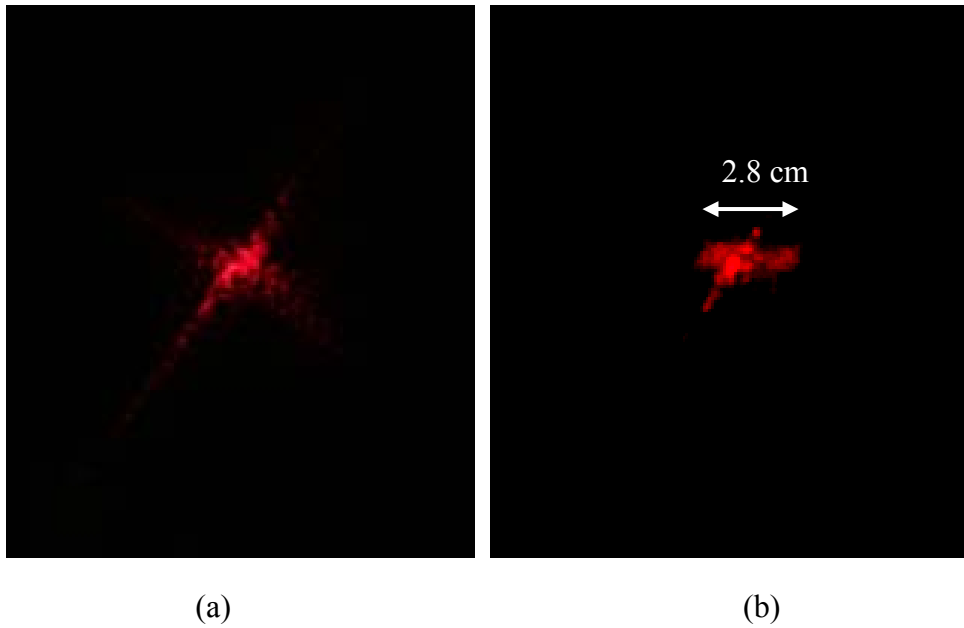


Figure 4-19. Images of the reflected laser on the screen: (a) without actuating and (b) with actuating.

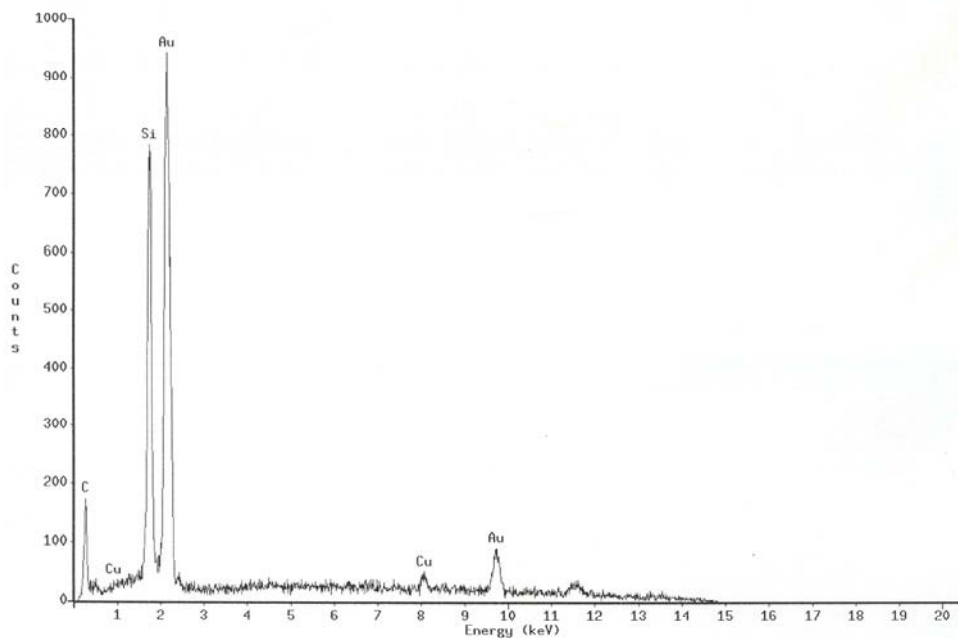
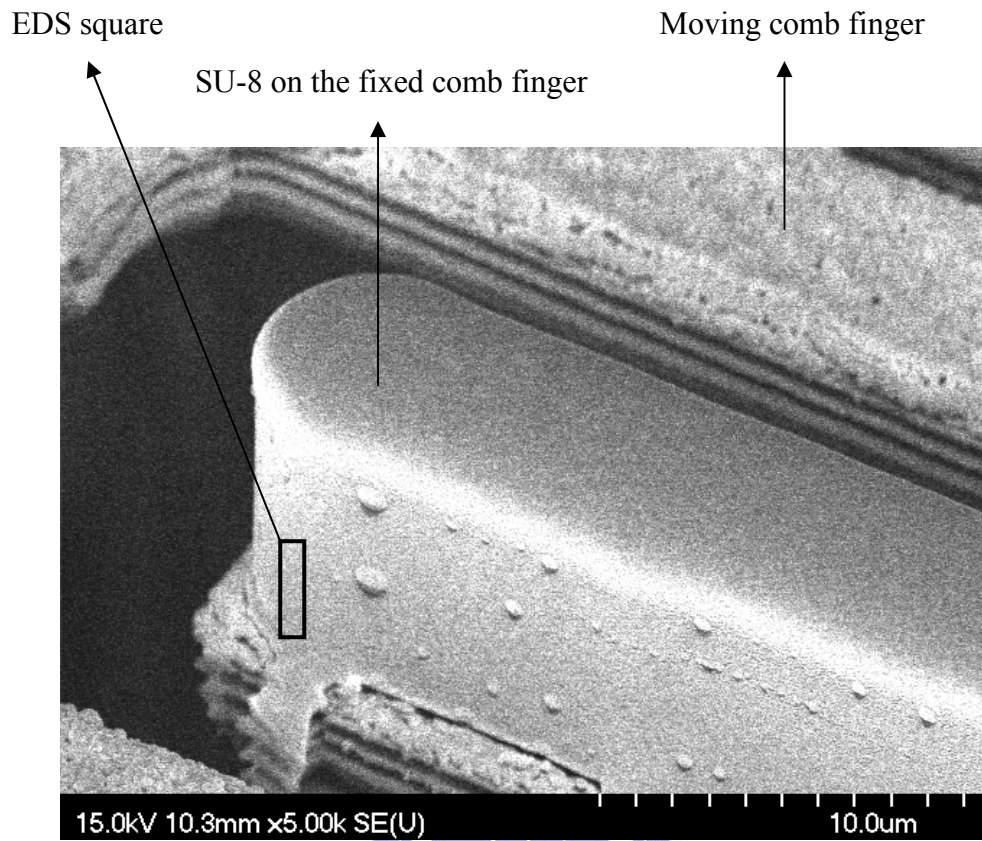
Table 4-3. Optical scanning measurement.

Frequency	Length of the image	Full optical scan angle ($4\theta_s$)
412.5 Hz	1.7 cm	0.487°
413.6 Hz	2.8 cm	0.802°

4-4 Gold deposition measurement

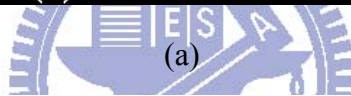
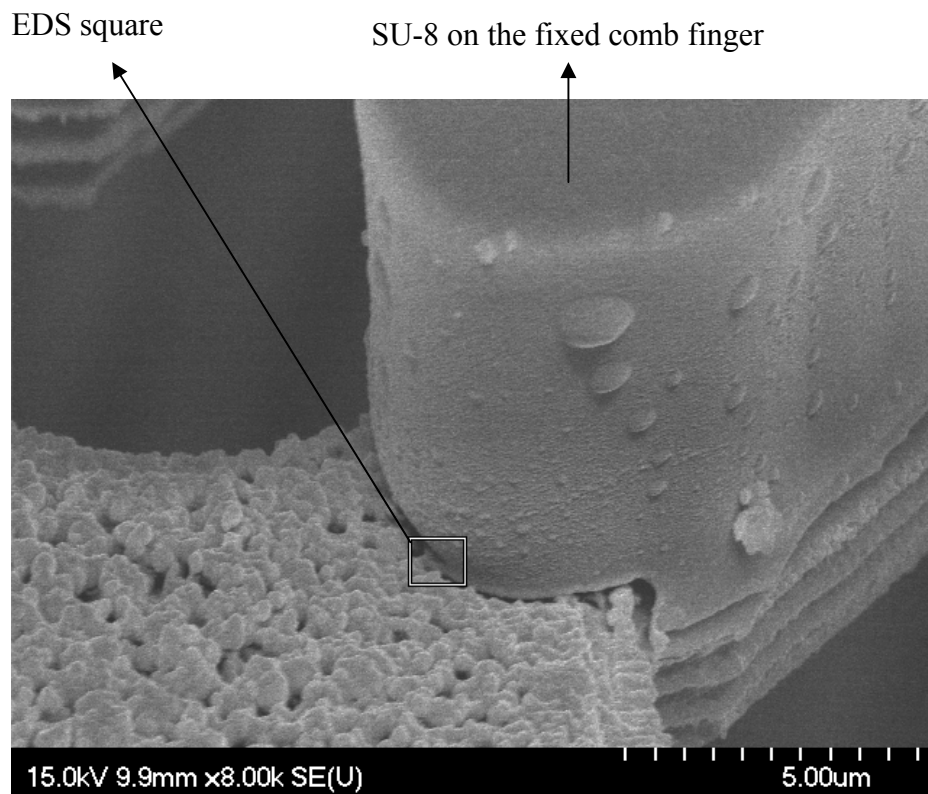
SU-8 is used as the fixed electrode, so gold is deposited for electrical conduction. Therefore, good step coverage of gold deposition is a critical factor. E-gun evaporation was used to deposit the gold. The rotary wafer carrier was used to improve the step coverage. To test the sidewall coverage of gold, EDS (Energy Dispersive Spectrometer) measurement was performed. Figure 4-20 (a) shows the SEM micrograph of SU-8. Figure 4-20 (b) shows the EDS result at the position shown in Figure 4-20 (a). Besides, the joint between SU-8 and substrate must be covered by gold to ensure electrical connection. Figure 4-21 (a) shows the SEM micrograph of the joint and Figure 4-21 (b) shows the EDS result at the position shown in Figure 4-21 (a). From Figure 4-20 and Figure 4-21, it can be seen that gold was deposited on the sidewall of SU-8 and the joint between SU-8 and substrate. The EDS results confirm the coating material is gold.

The electrical isolation was realized by the undercut of the oxide layer as depicted in Chapter 3. But some devices are shorted due to the connection of the gold. Figure 4-22 (a) shows the SEM micrograph of the shorted electrical isolation. The EDS result indicates that the connection is gold as shown in Figure 4-22 (b). The thickness of the deposited gold should be decreased to avoid the shortage phenomenon.

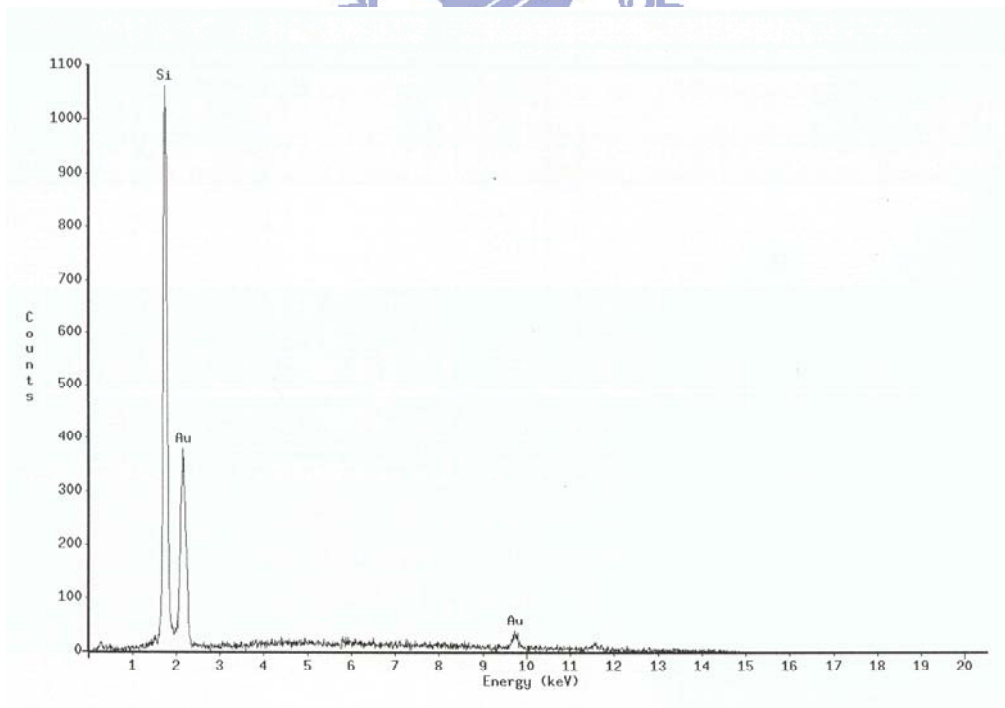


(b)

Figure 4-20. Measurement of sidewall of SU-8, (a) SEM micrograph and (b) EDS result.

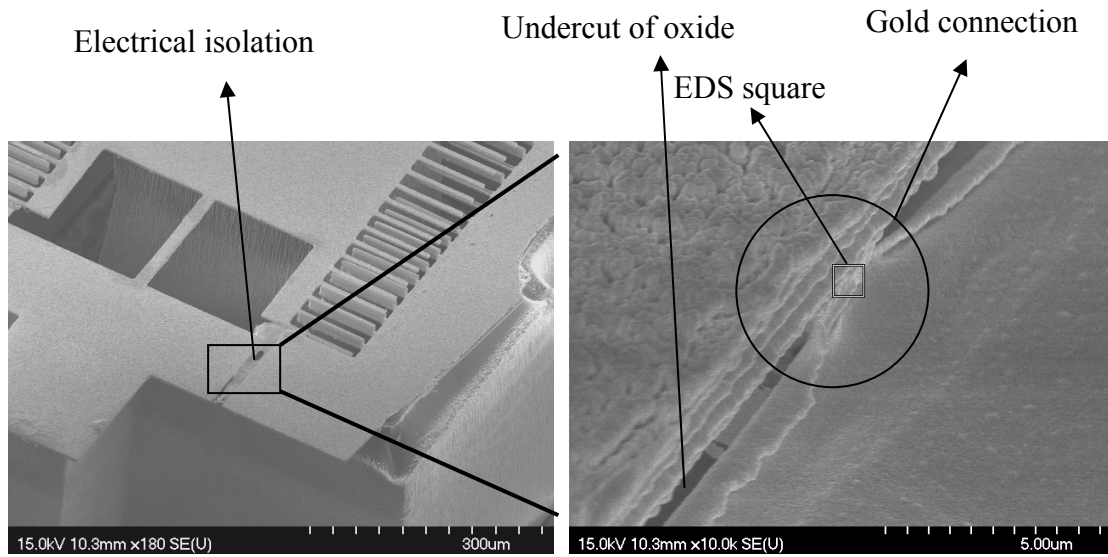


(a)

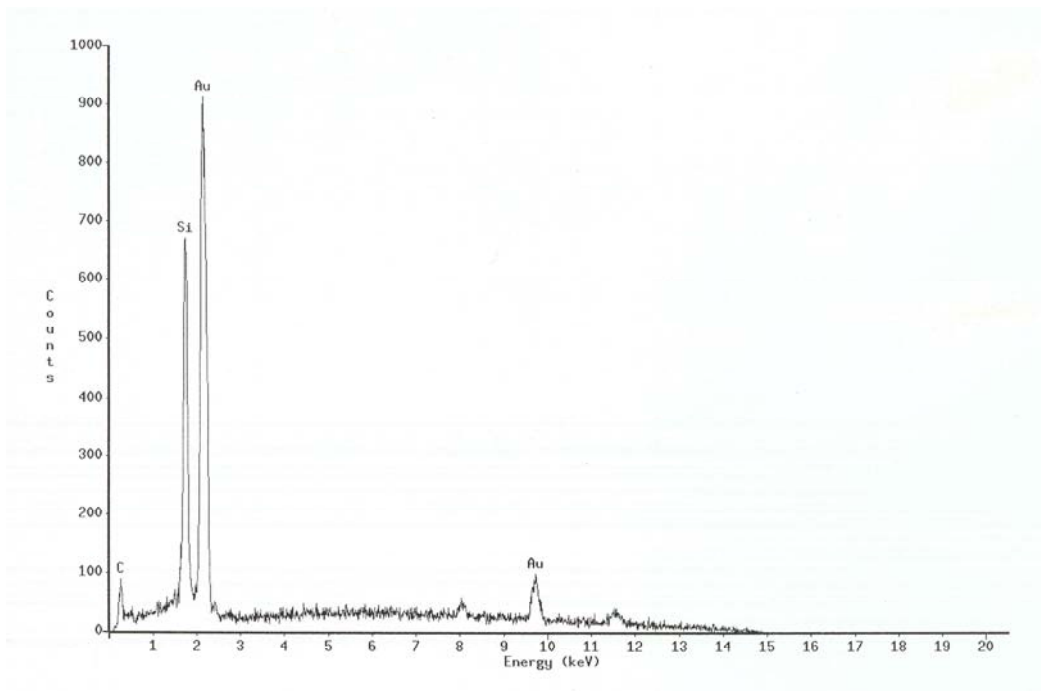


(b)

Figure 4-21. Measurement of the joint between SU-8 and the substrate, (a) SEM micrograph and (b) EDS result.



(a)

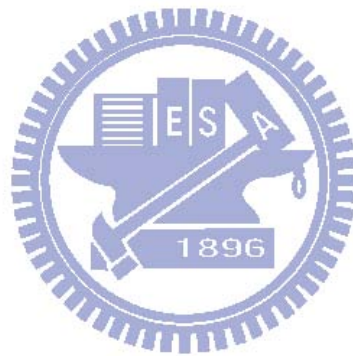


(b)

Figure 4-22. Shortage of the electrical isolation, (a) SEM micrograph and (b) EDS result.

4-5 Summary

The scanning characteristics as well as surface profiles of the proposed micro scanning mirror before assembly were measured. The rough surfaces caused by the nitride residues were measured. The maximum static scanning angle of the beam type mirror was 0.57° with 110 V applied voltage. The maximum dynamic scanning angle of the meander type mirror was 0.80° with ± 5 V sinusoidal and 5 V DC applied voltage at 413.6 Hz. The gold causes the shorted electrical isolation and the step coverage of gold deposition was verified by the EDS results.



Chapter 5

Conclusions and Future Work

A flip-up micro scanning mirror with vertical comb drive was demonstrated in this thesis. The characteristics of the micro scanning mirror before assembly were measured. The maximum static scanning angle of the beam type mirror was 0.57° with 110 V applied voltage. The maximum dynamic scanning angle of the meander type mirror was 0.80° with ± 5 V sinusoidal and 5 V DC applied voltage at 413.6 Hz. Nitride etching in HF vapor was the main problem in this work. This caused the SU-8 vertical fingers to peel off if the release time was long enough to release the mirror. Therefore the flip-up micro mirror could not be actuated.

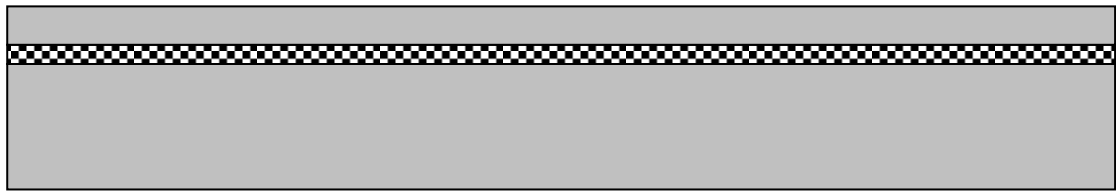
5-1 Future work



Design and fabrication problems encountered in this thesis need to be considered more carefully in the future. To ensure the flip-up micro mirror to work, the SU-8 needs to be patterned on silicon. Besides, the precision of the aligner limits the finger gap. Small finger gaps can produce good scanning performance. Furthermore, the misalignment of the comb fingers would affect the maximum scan angle [42]. For example, 10 % error of the finger gap spacing reduces the maximum scan angle to 80 % of the value without misalignment [17]. In order to solve all the problems, a new fabrication process with four masks is proposed. The vertical comb fingers fabricated by the new fabrication process are self-aligned to minimize the finger gap and eliminate the finger misalignment. The detailed fabrication flow is shown in Figure 5-1.

The SOI wafer is first cleaned by the standard RCA clean process. Then a

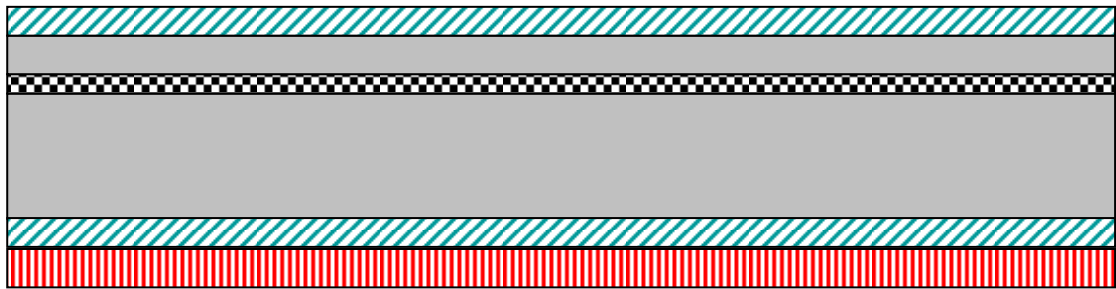
LPCVD nitride and a PECVD oxide are deposited on the both side and back side of the SOI wafer, respectively. Mask 1 defines the SOI device layer pattern except the fingers as shown in Figure 5-1 (c). Mask 2 defines the through-wafer holes under the push pads and the mechanical connection of the micro scanning mirror. Then a PECVD oxide is deposited on the front side and Mask 3 is the coarse definition of the moving comb fingers as shown in Figure 5-1 (f). Mask 4 defines the SU-8 pattern of both fixed and moving comb fingers as shown in Figure 5-1 (g). The comb fingers are defined in a single mask so the minimum gap of the fingers is limited by the mask and photolithography resolution. Compared to the original finger gap of 7 μm , 3 μm finger gap can be achieved in the new process. Then the front side oxide is etched by RIE as Figure 5-1 (f). Back side ICP and front side ICP are followed as shown in Figure 5-1 (i) and (l). The SU-8 on the moving comb fingers is stacked on the oxide and can be removed in the release step as shown in Figure 5-1 (k). Finally gold is deposited for electrical connection.

In the current design, the mirror was locked by the friction between the interlock and the sidewall of the mechanical connection substrate due to the misalignment of the double side aligner. Therefore the dimensions of the back mechanical connection must be carefully designed.



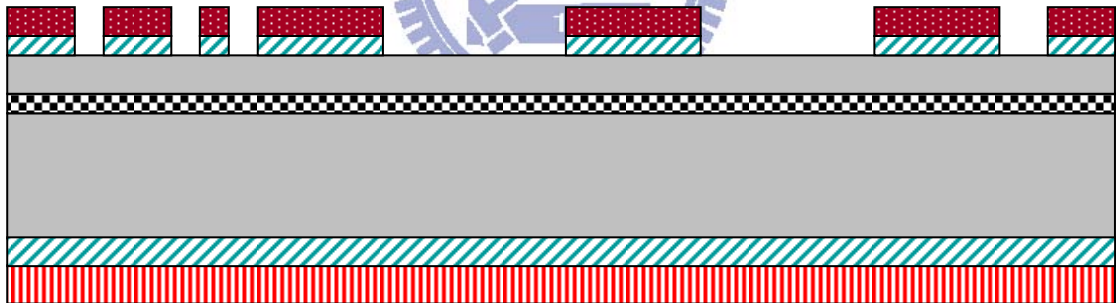
 Buried oxide  Silicon






(a) RCA cleaned SOI wafer



 Buried oxide  LPCVD nitride  PECVD oxide  Silicon

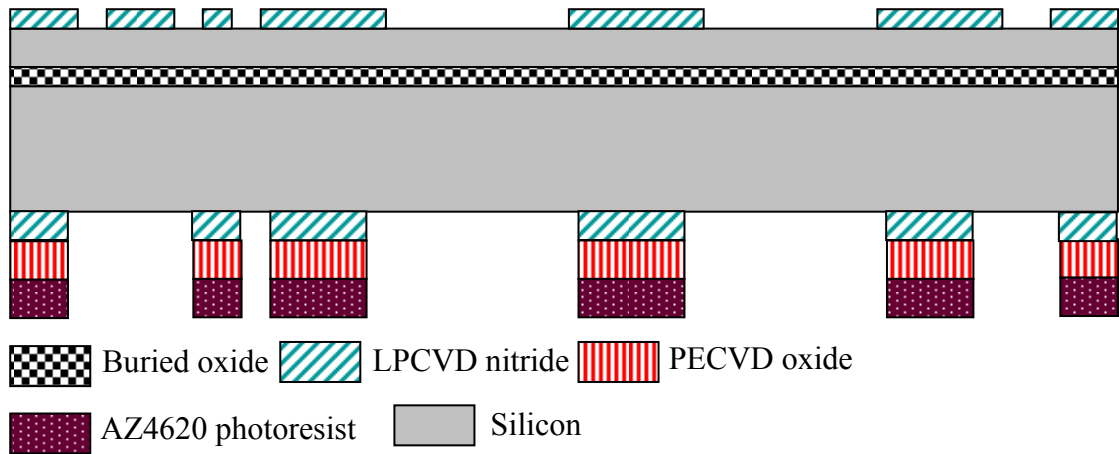
(b) Front side nitride and back side oxide deposition.



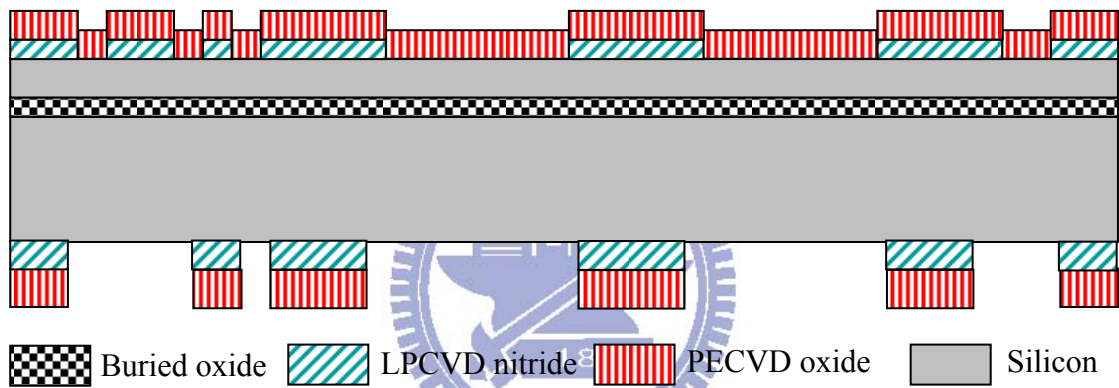
 Buried oxide  LPCVD nitride  PECVD oxide
 FH 6400 photoresist  Silicon

(c) Front side nitride patterning (Mask 1).

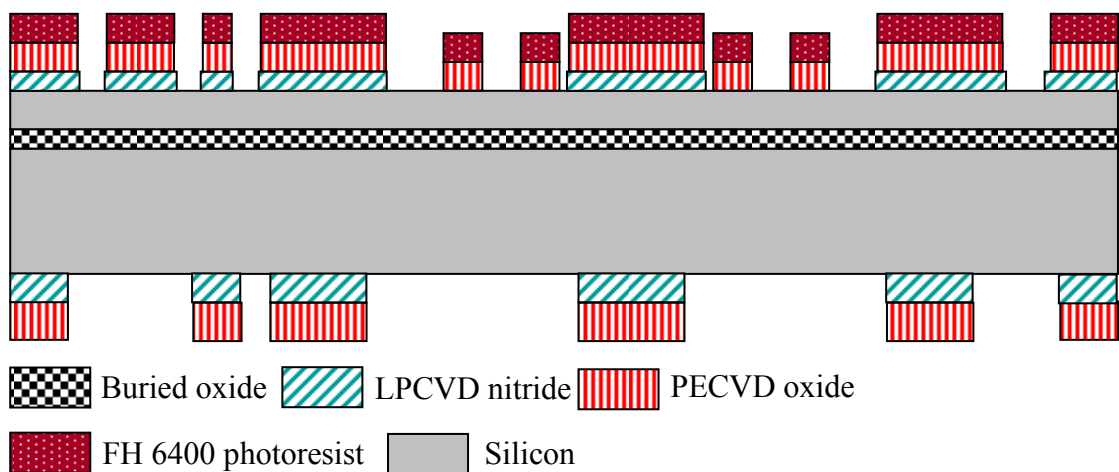
Figure 5-1. New fabrication flow.



(d) Back side oxide patterning (Mask 2).

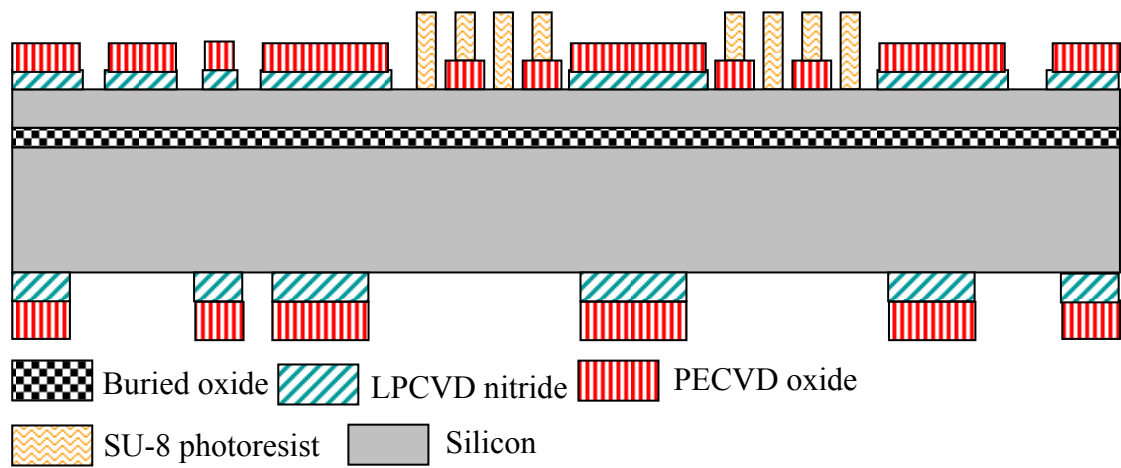


(e) Front side PECVD oxide deposition.

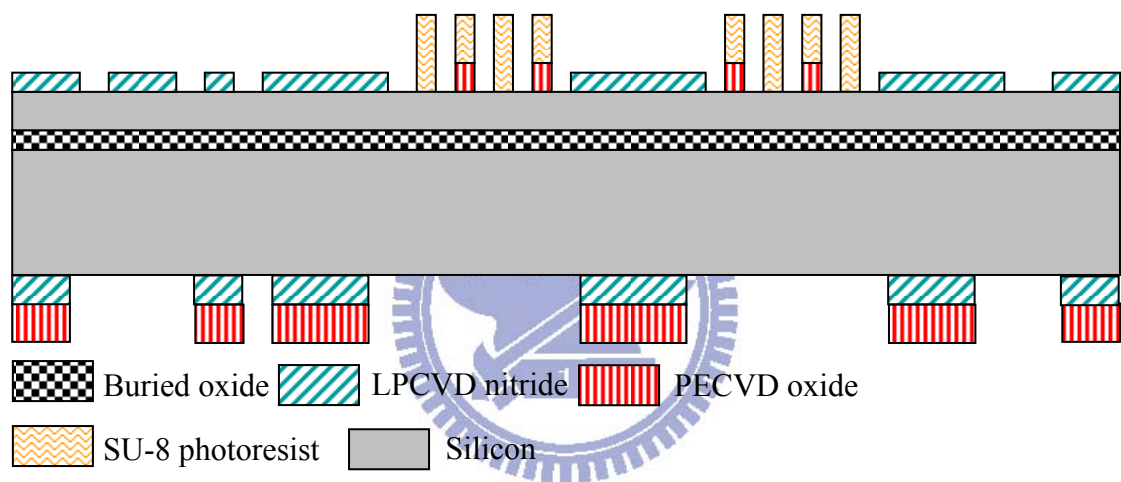


(f) Front side oxide patterning (Mask 3).

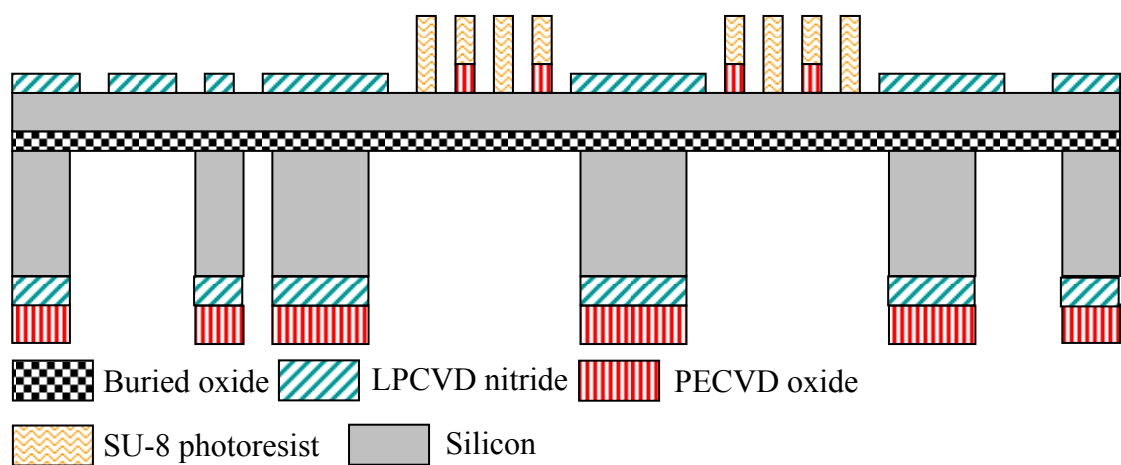
Figure 5-1. New fabrication flow (continued).



(g) SU-8 photoresist patterning.

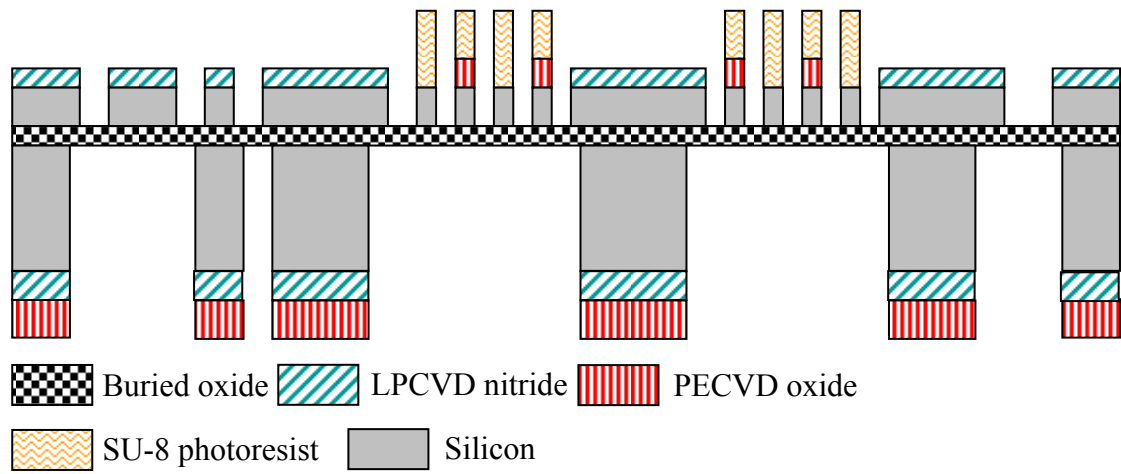


(h) Front side oxide etching.

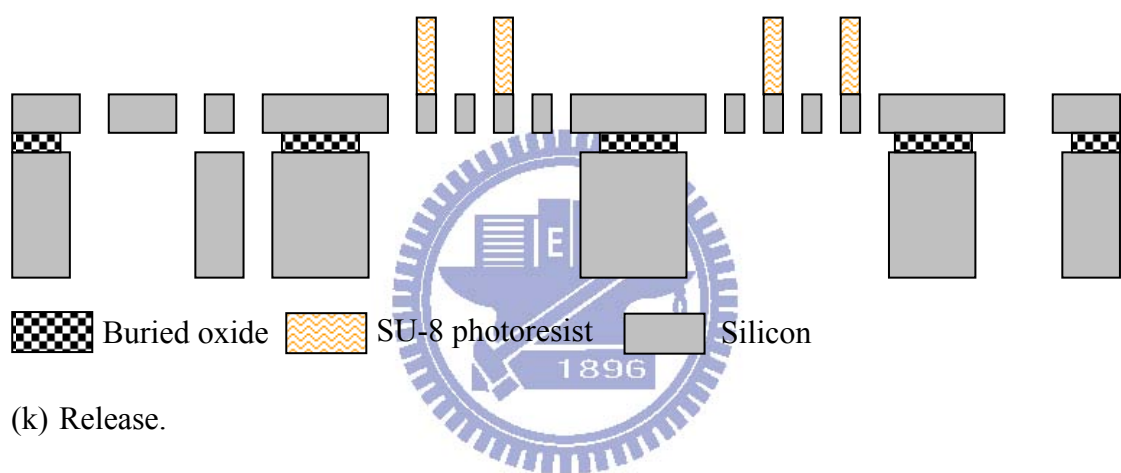


(i) Back side ICP.

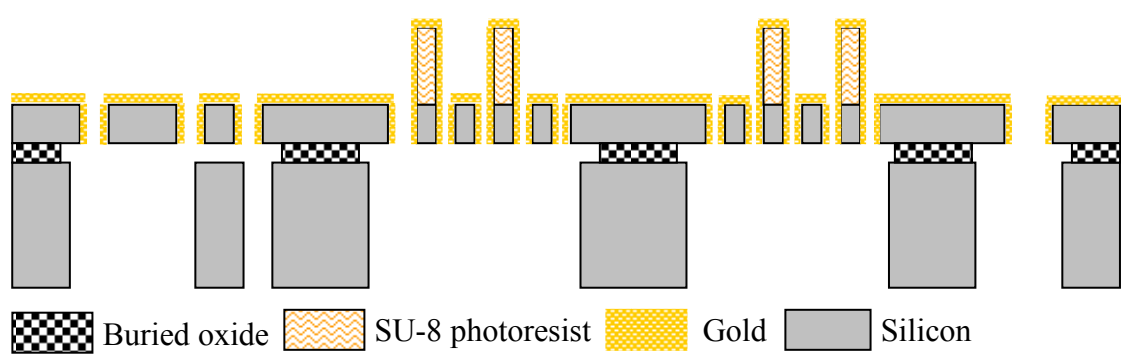
Figure 5-1. New fabrication flow (continued).



(j) Front side ICP.



(k) Release.



(l) Gold deposition.

Figure 5-1. New fabrication flow (continued).

Reference

- [1] S. S. Lee, L. S. Huang, C. J. Kim, and M. C. Wu, "Free-space fiber-optic switches based on MEMS vertical torsion mirrors," *Journal of Lightwave Technology*, vol. 17, no. 1, pp. 7-13, 1999.
- [2] M. H. Kiang, O. Solgaard, K. Y. Lau, and R. S. Muller, "Electrostatic combdrive-actuated micromirrors for laser-beam scanning and positioning," *Journal of Microelectromechanical System*, vol. 7, no. 1, pp. 27-37, 1998.
- [3] Texas Instruments
<http://www.dlp.com/technology/how-dlp-works/default.aspx>
- [4] L. Y. Lin, J. L. Shen, S. S. Lee, and M. C. Wu, "Realization of novel monolithic free-space optical disk pickup heads by surface micromachining," *Optics Letters*, vol. 21, no. 2, pp. 155-157, 1996.
- [5] C. A. Lin, "A MEMS-based optical pickup unit assembled by simple push operation on SOI wafers," *Master thesis*, Department of electrical and control engineering, National Chiao Tung University, Taiwan, 2010.
- [6] J. E. Ford, V. A. Akayuk, D. J. Bishop, and J. A. Walker, "Wavelength add-drop switching using tilting micromirrors," *Journal of Lightwave Technology*, vol. 17, no. 5, pp. 904-911, 1999.
- [7] S. Schweizer, S. Calmes, M. Laudon, and Ph. Renaud, "Thermally actuated optical microscanner with large angle and low consumption," *Sensors and Actuators A: Physical*, vol. 76, issues 1-3, pp. 470-477, 1999.
- [8] J. Singh, J. H. S. Teo, Y. Xu, C. S. Premachandran, N. Chen, R. Kotlanka, M. Olivo, and C. J. R. Sheppard, "A two axes scanning SOI MEMS micromirror for endoscopic bioimaging," *Journal of Micromechanics and Microengineering*, vol. 18, no.2, 2008.
- [9] R. A. Miller and Y. C. Tai, "Micromachined electromagnetic scanning mirrors," *Optical Engineering*, vol.36, no. 5, pp. 1399-1407, 1997.
- [10] I. J. Cho and E. Yoon, "A low-voltage three-axis electromagnetically actuated

- micromirror for fine alignment among optical devices,” *Journal of Micromechanics and Microengineering*, vol.19, no. 8, 2009.
- [11] T. L. Tang, C. P. Hsu, W. C. Chen, and W. Fang, “Design and implementation of a torque-enhancement 2-axis magnetostatic SOI optical scanner,” *Journal of Micromechanics and Microengineering*, vol. 20, no. 2, 2010.
- [12] R. A. Conant, J. T. Nee, K. Y. Lau, and R. S. Muller, “A flat high-frequency scanning micromirror,” *Proc. Tech. Dig. Solid-State Sensor and Actuator Workshop*, Hilton Head, SC, June 4-8, 2000, pp. 6-9.
- [13] D. Lee, U. Krishnamoorthy, K. Yu, and O. Solgaard, “Single-crystalline silicon micromirrors actuated by self-aligned vertical electrostatic combdrives with piston-motion and rotation capability,” *Sensors and Actuators A: Physical*, vol. 114, issues 2-3, pp. 423-428, 2004.
- [14] H. Ra, W. Piyawattanametha, Y. Taguchi, D. Lee, M. J. Mandella, and O. Solgaard, “Two-dimensional MEMS scanner for dual-axes confocal microscopy,” *Journal of Microelectromechanical System*, vol. 16, no. 4, pp. 969-976, 2007.
- [15] J. H. Lee, Y. C. Ko, H. M. Jeong, B. S. Choi, J. M. Kim, and D. Y. Jeon, “SOI-based fabrication processes of the scanning mirror having vertical comb fingers,” *Sensors and Actuators A: Physical*, vol. 102, issues 1-2, pp. 11-18, 2002.
- [16] Y. C. Ko, J. W. Cho, Y. K. Mun, H. G. Jeong, W. K. Choi, J. W. Kim, Y. H. Park, J. B. Yoo, and J. H. Lee, “Eye-type scanning mirror with dual vertical combs for laser display,” *Sensors and Actuators A: Physical*, vol. 126, issues 1, pp. 218-226, 2006.
- [17] D. Hah, C. A. Choi, C. K. Kim, and C. H. Jun, “A self-aligned vertical comb-drive actuator on an SOI wafer for a 2D scanning micromirror,” *Journal of Micromechanics and Microengineering*, vol.14, no. 8, pp. 1148-1156, 2004.
- [18] M. Kim, J. H. Park, J. A. Jeon, B. W. Yoo, I H Park, and Y. K. Kim, “High fill-factor micromirror array using a self-aligned vertical comb drive actuator with two rotational axes,” *Journal of Micromechanics and Microengineering*,

vol.19, no. 3, 2009.

- [19] P. R. Patterson, D. Hah, H. Nguyen, H. Toshiyoshi, R. M. Chao, and M. C. Wu, "A scanning micromirror with angular comb drive actuation," *The Fifteenth IEEE International Conference on MEMS 2002*, Las Vegas, Nevada, Jan. 20-24, pp. 544-547, 2002.
- [20] K. H. Jeong and L. P. Lee, "A novel microfabrication of a self-aligned vertical comb drive on a single SOI wafer for optical MEMS applications," *Journal of Micromechanics and Microengineering*, vol.15, no. 2, pp. 277-281, 2005.
- [21] D. Hah, S. T. Y. Huang, J. C. Tsai, H. Toshiyoshi, and M. C. Wu, "Low-voltage, large-scan angle MEMS analog micromirror arrays with hidden vertical comb-drive actuators," *Journal of Microelectromechanical System*, vol. 13, no. 2, pp. 279-289, 2004.
- [22] C. Tsou, W. T. Lin, C. C. Fan, and Bruce C. S. Chou, "A novel self-aligned vertical electrostatic combdrives actuator for scanning micromirrors," *Journal of Micromechanics and Microengineering*, vol.15, no. 4, pp. 855-860, 2005.
- [23] T. Akiyama and K. Shono, "Controlled stepwise motion in polysilicon microstructures," *Journal of Microelectromechanical System*, vol. 2, no. 3, pp. 106-110, 1993.
- [24] J. R. Reid, V. M. Bright, and J. T. Butler, "Automated assembly of flip-up micromirrors," *Sensors and Actuators A: Physical*, vol. 66, no. 1, pp. 292-298, 1998.
- [25] W. J. Robert, "Electrostatic self-assembly of raised surface micromachined structures for optics," Master Thesis, Department of Engineering Science, Simon Fraser University, Canada, 2000.
- [26] V. Kaajakari and A. Lal, "Electrostatic batch assembly of surface MEMS using ultrasonic triboelectricity," in *The 14th IEEE International Conference on Micro Electro Mechanical Systems*, pp. 10-13, 2001.
- [27] Y. W. Yi and C. Liu, "Magnetic actuation of hinged microstructures," *Journal*

of Microelectromechanical System, vol. 8, no. 1, pp. 10-17, 1999.

- [28] A. P. Hui and W. J. Li, "Non-contact batch micro-assembly by centrifugal force," *The Fifteenth IEEE International Conference of Microelectromechanical Systems*, pp. 184-187, 2002.
- [29] R. W. Johnstone, D. Sameoto, and M. Parameswaran, "Non-uniform residual stresses for parallel assembly of out-of-plane surface-micromachined structures," *Journal of Micromechanics and Microengineering*, vol.16, no. 11, N17-22, 2006.
- [30] R. R. A. Syms, C. Gormley and S. Blackstone, "Improving yield, accuracy and complexity in surface tension self-assembled MOEMS," *Sensors and Actuators A: Physical*, vol. 88, no. 3, pp. 273-283, 2001.
- [31] S. H. Tsang, D. Sameoto, I. G. Foulds, R. W. Johnstone, and M. Parameswaran, "Automated assembly of hingeless 90° out-of-plane microstructures," *Journal of Micromechanics and Microengineering*, vol. 17, no. 7, pp. 1314-1325, 2007.
- [32] K. Tsui, A. A. Geisberger, M. Ellis and G. H. Skidmore, "Micromachined end-effector and techniques for directed MEMS assembly," *Journal of Micromechanics and Microengineering*, vol. 14, no. 4, pp. 542-9, 2004.
- [33] Microchem.
http://www.microchem.com/products/su_eight.htm
- [34] R. Raymond and J. Raymond, "Torsion," in *Roark's formulas for stress and strain*, the 6th edition: McGraw Hill, 1989.
- [35] J. J. Wortman and R. A. Evans, "Young's Modulus, Shear Modulus, and Poisson's Ratio in Silicon and Germanium," *Journal of Applied Physics*, vol. 36, no. 1, pp. 153-156, 1965.
- [36] K. E. Petersen, "Silicon as a mechanical material," *Proceedings of the IEEE*, vol. 70, no. 5, pp. 420-457, 1982.
- [37] M. Sasaki, S. Yuki, and K. Hane, "Performance of tense thin-film torsion bar

for large rotation and low-voltage driving of micromirror,” *IEEE Journal of Selected Topics in Quantum Electronics*, vol. 13, no. 2, pp. 290-296, 2007.

- [38] Y. Fukuta, H. Fujita, and H. Toshiyoshi, “Vapor hydrofluoric acid sacrificial release technique for micro electro mechanical system using labware,” *Japanese Journal of Applied Physics*, vol. 42, pp. 3690-3694, 2003.
- [39] C. K. Chung, “Geometrical pattern effect on silicon deep etching by inductively coupled plasma system,” *Journal of Micromechanics and Microengineering*, vol. 14, no. 4, pp. 656-662, 2004.
- [40] B. Du Bois, G. Vereecke, A. Witvrouw, P. De Moor, C. Van Hoof, A. De Caussemaeker, and A. Verbist, “HF etching of Si-oxide and Si-nitride for surface micromachining,” *Proc. of the Sensor Technology Conf. 2001*, pp. 131-136, 2001.
- [41] G. Barillaro, A. Molfese, A. Nannini and F. Pieri, “Analysis, simulation and relative performance of two kinds of serpentine springs,” *Journal of Micromechanics and Microengineering*, vol. 15, no. 4, pp. 736-746, 2005.
- [42] U. Krishnamoorthy, D. Lee and O. Solgaard, “Self-aligned vertical electrostatic combdrives for micromirror actuation,” *Journal of Microelectromechanical System*, vol. 12, no. 1, pp. 458-464, 2003.